First-Principles Investigation of Crystal Structures and Stabilities of Precipitates in GP zone-strengthened Mg alloys

---

A

Dissertation

Presented to

the faculty of the School of Engineering and Applied Science

University of Virginia

---

in partial fulfillment

of the requirements for the degree

Doctor of Philosophy

by

Du Cheng

May 2023

APPROVAL SHEET

This
Dissertation
is submitted in partial fulfillment of the requirements
for the degree of
Doctor of Philosophy

Author: Du Cheng

This Dissertation has been read and approved by the examing committee:

Advisor: Bi-Cheng Zhou

Advisor:

Committee Member: Sean Agnew

Committee Member: James Howe

Committee Member: Chris Paolucci

Committee Member: Derek Warner

Committee Member:

Committee Member:

Accepted for the School of Engineering and Applied Science:

Jennifer L. West, School of Engineering and Applied Science

May 2023

Abstract

Mg alloys are the lightest of all structural metals, yet they remain underutilized in applications where weight is critical to performance and efficiency, e.g., automotive, rail and aerospace, due to insufficient strength and ductility. It has been known that Guinier-Preston zones (GP zones, nanometer-sized solute-rich clusters formed coherently on parent lattice in the early stage of precipitations) are excellent means to both high specific strength, ductility, and energy absorption capacity. GP zones have been observed in Mg-rare earth alloys as well as Mg-Zn and Mg-Ca-X (X = Zn, Al) alloys, which are free of rare-earth elements and, thus are low cost for mass production. However, the crystal structures and stabilities of the precipitates, especially GP zones, are not clear in Mg-Zn and Mg-Ca-X (X = Zn, Al) alloys.

Here we leverage a statistical mechanical method called cluster expansion (CE) parameterized by density functional theory (DFT) calculations to search for low energy structures at the ground state and identify potential GP zones in the Mg-Zn and Mg-Zn-Ca systems. In Mg-Zn binary alloys, the GP zones are predicted to appear on the basal plane as well as the first-order $\{10\bar{1}0\}$ and second-order $\{\}$ prismatic planes of the Mg matrix. The Zig-Zag plates on $\{10\bar{1}0\}$ planes are consistent with the observed ones in experiments. Monte Carlo simulation is adopted to determine the stabilities of GP zones at elevated temperatures. The stabilities of peak-aged β_1' and β_2' precipitates are also analyzed in addition to GP zones.

In Mg-Zn-Ca ternary alloys, multiple metastable GP zones with various compositions are predicted, which show striking similarities and are all structurally related to monolayer Mg2X with each X atom (e.g., Ca) 6-fold coordinated by Mg atoms on the HCP basal plane. An increased number of Mg atoms in monolayer Mg2X are replaced by Zn atoms to form ordered GP zones at an increased Zn/X ratio due to strong attractive interactions between Zn and X solutes, which ultimately leads to lower formation energies of the GP zones. In addition to monolayer GP zones, the atomic structures of precipitates formed after GP zones during aging are also proposed based on experimental information, i.e., compositions in 3D-atom probe tomography (3D-APT), morphologies in high angle annular dark field-scanning transmission electron microscopy (HAADF-STEM), and symmetry in diffraction patterns. To validate the proposed structures, stabilities are verified in DFT, and simulated TEM images and diffraction patterns are compared with experimental observations.

Further, to incorporate effects of large size-mismatch of elements in the above systems, the mixed-space cluster expansion (MSCE) method, which includes the long-ranged coherency strain energy in addition to shorted-ranged chemical interactions in CE, will be generalized to multi-component systems with arbitrary symmetries and applied to the current HCP systems. With MSCE and Monte Carlo, the interplay between strain and chemical interactions is analyzed for coherent precipitates formed in early-stage aging, especially for monolayer GP zones observed in current systems that challenges the capability of traditional calculation methods, e.g., continuum elasticity plus empirical interfacial energies and phase field model. The current work not only searches for potential precipitates in Mg-Zn and Mg-Zn-Ca alloys, the output of MSCE can also guide large-scale simulations of the mechanical behavior of precipitates during deformation.

Keyword:

First-principles, Precipitates, Cluster Expansion, Thermodynamic Stabilities, Simulated TEM.

Acknowledgements

Reflecting on this journey, I realize that the gratitude I have is beyond words. I’m grateful for all the support and guidance I received that has led me here. First, I would like to thank my advisor, Prof. Bi-Cheng Zhou, who trusted me and gave me the opportunity to join the MSE department at UVa. His patience gave me enough time to do my project at my pace and plenty of space to explore science freely. His gentle manner to the mistakes I made allowed me to correct them and continue my work with confidence. His clear way to describe scientific and engineering problems helped me to reflect on my expression in English as a second language. It was a joy to work with him.

I would also like to thank my committee members, Prof. Sean Agnew, Prof. James Howe, Prof. Derek Warner and Prof. Chris Paolucci. Most of my committee members are professors in the Mg project. I’m so grateful to join this collaborative DMREF project, which include experts in both experiments and simulations. Each DMREF meeting is an opportunity for me to learn from different aspects on materials, e.g., the mechanical properties in macro scale and atom movements in micro scale. I would like to thank Prof. Agnew for the big picture of the project, Prof. Warner and Basel for the shared atomic structures of precipitates and discussions on machine learning potentials, and Prof. Paolucci for the time on my thesis. Especially, I would like thank Prof. Howe and Dr. Eric Hoglund for the help on the simulations of TEM images and explanations of the diffraction patterns. It is their help that enabled me overcome the difficulties in my work and complete my papers.

I would also like to thank my collaborators from NIMS, Japan: Dr. Taisuke Sasaki and Dr. Zehao Li. I want to thank Dr. Zehao Li for sharing with me his beautiful TEM images of the precipitates in the Mg-Zn-Ca alloy, which inspired me to explore the structures of precipitates. I appreciate each discussion with Zehao on problems we encountered in the study, and I really respect the cautious attitude of Zehao and Dr. Sasaki on science.

Lastly, I would like to thank my family. It is my parents’ unconditional love and support that gives me strength to walk through ups and downs. I would also like to thank my husband, Dr. Kang Wang. The challenging life in another country became interesting with a partner. Many issues in both my daily life and my academic research were tackled with the loving support of my husband. For my daughter, I’m sorry that the Covid pandemic separates us on the two sides of the planet. I hope to be reunited with my family soon.

Table of Contents

List of Symbols

APT	Atom probe tomography
RE	Rare Earth
HAADF-STEM	High-angle annular dark field-scanning transmission electron microscopy
TEM	Transmission electron microscopy
CE	Cluster expansion
MSCE	Mixed-space cluster expansion
MC	Monte Carlo
NBED	Nanobeam electron diffraction
SAED	Selected-area electron diffraction
SQS	Special quasi-random structures
EDP	Electron diffraction patterns
HCP	Hexagonal closed packed
DFT	Density functional theory
OR	Orientation relationship
GP	Guinier-Preston
LOOCV	Leave one out cross-validation
$\hat{H}$	Hamiltonian
Ψ	Wave function
E	Ground state energy
KS	Kohn-Sham
LDA	Local Density Approximation
GGA	Generalized Gradient Approximation
PBE	Perdew-Burke-Ernzerhof
VASP	Vienna ab initio simulation package
σ_i	Spin variable
$S_{l,p}(\sigma)$	Spin variable with additional subscript for multi-sublattice
k_B	Boltzmann constant
i	Species
ECI	Effect cluster interactions

ATAT	Alloy Theoretic Automated Toolkit
CSE	Coherency strain energy
ΔE^{epi}	Epitaxial strain energy
ΔE_f	Formation energy
ΔE_f^{solute}	Formation energies per solute atom
$E_2(\sigma)$	Pair energy contributions
$J_{m,n}$	Effective interaction energy of pairs of site m and n
$\boldsymbol{R}_l$	Origin of the l-th primitive cell
$V_{m,n}(\boldsymbol{k})$	Fourier transform of r-space pair interaction energy
$V_{m,n}^{SR}(\boldsymbol{k})$	Short-range pair interactions in k space
$V_{m,n}^{LR}(\boldsymbol{k})$	Long-range pair interactions in k space
$V^{CS}(\boldsymbol{k})$	Long-ranged CSE interaction parameter
$\tilde{V}(\boldsymbol{k})$	$v \times v$ matrix of the $V_{m,n}(\boldsymbol{k})$
$\hat{S}_{\boldsymbol{k}}(\sigma)$	Structural factor
$S_{-\boldsymbol{k},p}^{*}$	Complex conjugate of structure factor
$\mathbf{G}$	Plane normal
$\mathbf{V}_1$	The vector on the epitaxial plane
$\mathbf{V}_2$	The vector on the epitaxial plane
$\mathbf{L}^0$	3×3 matrix for the lattice vectors of the end members at equilibrium
$\mathbf{S}$	3×3 matrix with dimensionless stretch of the lattice along $\mathbf{G}$
$\mathbf{Q}$	3×3 matrix using normalized vectors
w_σ	Weight of a configuration σ

List of Figures

List of Tables

Chapter 1 Introduction

1.1 GP zone-strengthened Mg alloys

Next-generation high-performance structural materials are desired for lightweight design and advanced energy applications. Mg alloys are the lightest of all structural metals, yet they remain underutilized in many applications where weight is critical to performance and efficiency, e.g., automotive, rail and aerospace. There are many reasons for this, including high processing cost, limited strength, and ductility. Additionally, although room temperature formability of some Mg alloys has been dramatically improved by the addition of rare earth (RE) elements [1], [2], the RE elements are viewed as high cost and strategic liabilities caused by their exclusive production in China, which increase the cost of raw materials for Mg-RE alloys. Therefore, we need a strategy that can not only greatly increase the strength, but also increase the ductility and formability of Mg alloys with low cost.

Recently an alloy design strategy has been reported: strengthen alloys with high-density nanoprecipitation with minimal lattice misfit [3]. Traditionally, many alloys can obtain their outstanding strength from semi-coherent precipitates, which create heterogeneous distribution of large coherency strain around them and interact with dislocations. However, the strains also promote crack initiation under load and diminish the ductility of materials. Under the new strategy, it is shown that highly dispersed, fully coherent precipitates (the crystal lattice of the precipitates is almost the same as that of the surrounding matrix), showing very low lattice misfit with the matrix and high anti-phase boundary energy, strengthen steel alloys without sacrificing ductility [3]. The very low lattice mismatch between the precipitates and the matrix promotes the formation of extremely high density of precipitates with small size due to the low the nucleation energy barrier. As expected, the small elastic lattice misfit strain does not contribute significantly to the strengthening, but the high antiphase boundary energies due to the chemical ordering of the precipitates leads to the high cutting stress for dislocations. Therefore, the strategy of the hardening

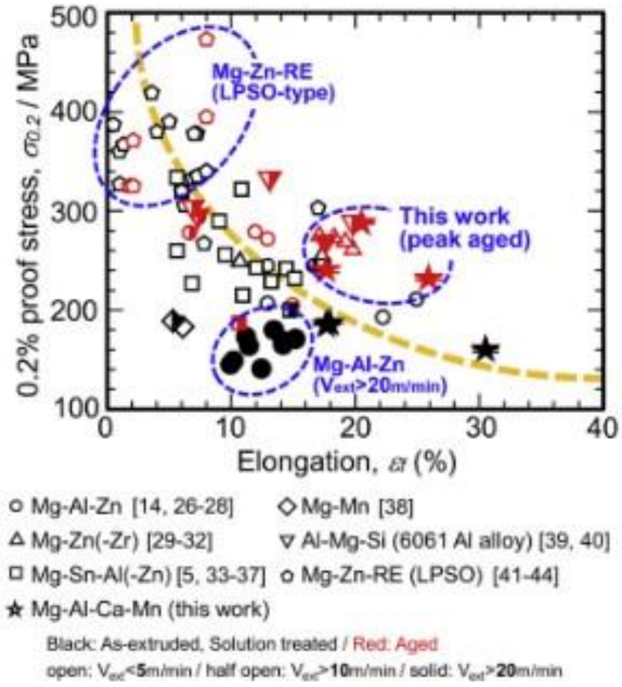

Fig. 1.1 Plot of Mg alloy strength vs. ductility showing that GP-zone strengthened alloys (labeled “This work”) have the best combination, especially for applications demanding some formability. Reproduced from [6].

by high density coherent precipitates are applied in Mg alloys and is expect to show the similar improvement in ductility.

GP zones, as the very early-stage precipitates, usually keep high coherency with its matrix. In Mg alloys, the recent experimental studies [4]–[7] shows that the strength of alloys can be significantly enhanced, while a high elongation of 15-25% can also be retained at the same time (**Fig. 1.1**). The analysis shows that there are high number densities of GP zones formed during early-stage aging (10^{24} m^{-3}) in those alloys, which means the high number density GP zones have potential to improve both strength and ductility of Mg alloys. Further, these Mg alloys with GP zones also overcome another Achille's heel of traditional Mg alloys, low productivity rates during deformation processing steps such as extrusion or rolling. They can be extruded at rates comparable to common 6000-series Al alloys, with much lower density. This lower density is the key factor which would increase the resistance to plastic bending (with a figure of merit = $\sqrt{(yield\ strength)}/density$). This class of alloys boasts 75% improvement over Al alloys

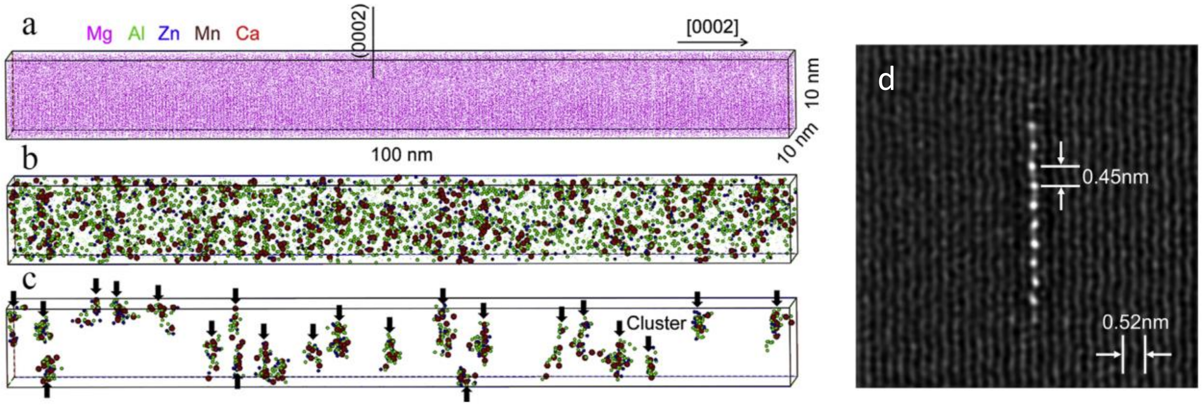

Fig. 1.2 (a)~(c): 3D-APT elemental mappings of (a) Mg and (b) solute atoms obtained from the bake-hardened Mg-Al-Zn-Mn-Ca alloy. (c) Detected Al, Zn and Ca clusters in the selected region. Reproduced from [4]. (d): Fourier-filtered high resolution HAADF images of the peak-aged Mg–0.3Ca–0.6Zn alloy taken from the $[10\bar{1}0]$ direction, showing the ordered monolayer GP zone. Reproduced from [10].

presently employed by the auto industry and far exceeds those of current automotive steels. Therefore, these GP zones-strengthened Mg alloys can have good ductility with enhanced strain rate sensitivity, which means they can resist high strain rate deformation under extreme conditions like collisions in engineering applications.

In RE-free systems, GP zones has been reported in Mg alloyed with elements of Zn[8], Al[9], Ca[10], and Sn [11], which are all amongst the earth's most abundant elements. Bian et al. [4] used 3D-APT to reveal the co-clustering of Al, Zn, and Ca atoms in Mg after a short time aging as shown in **Fig. 1.2(a)~(c)**. Using high-angle annular dark field-scanning transmission electron microscopy (HAADF-STEM), Oh-ishi et al. [10] characterized the finely dispersed monolayer GP zones with in-plane ordered structure in Mg-0.3Ca-0.6Zn alloy. In the HAADF-STEM image shown in **Fig. 1.2(d)**, ordered monolayer GP zones appear as bright dots along the basal plane. Therefore, the highly coherent precipitates of GP zones with chemical ordering inside the precipitates can be formed in Mg alloys with no addition of RE elements. *According to the above experimental observations and analysis, it is proposed that ordered Guinier-Preston zones are excellent means to both high specific strength, ductility, and energy absorption capacity in Mg alloys without expensive alloying elements*.

1.2 Research Objective

The GP zone-strengthened Mg alloys have great potential in realizing desired properties of high specific strength, ductility, and energy absorption capacity. However, the fundamental gap in understanding is our inability to predict the appropriate alloy chemistry and obstacle (e.g., GP zone) microstructure in order to controllably maintain these properties, e.g., strength, ductility and formability. The general framework of thermally activated slip of dislocations [12] provides a basis for developing the governing physics. According to the Orowan equation [13], the shape, size and orientation of obstacles, like GP zones, have strong effects on their interaction with dislocation motion. It is also suggested that, for Mg alloys with GP zones, the strain field around GP zones, even though not large, are possible to affect the interaction between GP zones and dislocations. As known, the GP zones have a specific shape (e.g., spherical, rod- or plate-like) in the matrix which is regulated by a delicate interplay between interfacial chemical energy and coherency strain energy, as an example in Al-Cu alloys shown in **Fig. 1.3**. It is hypothesized that the shape and orientation of GP zones in Mg alloys can be effectively modified by tuning their interfacial energies and coherency strain energies through microalloying. However, even with the state-of-art experimental equipment, the exact identification of the atomic scale structures of precipitates formed during aging, e.g., GP zones, is still difficult, and the explanation still remains unclear for how interfacial and strain affect the observed shapes and orientations of precipitates. Therefore, modeling and calculations are proposed here to solve these issues.

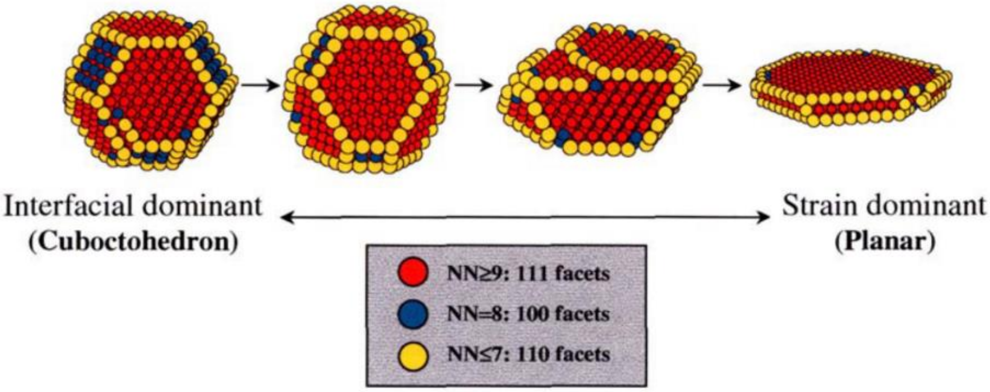

Fig. 1.3 Calculated precipitate shapes with both strain and interfacial energy contributions in Al-Cu system using MSCE/Monte Carlo method. The calculated precipitate shape gradually evolves from cuboctohedron to planar as the coherency strain energy becomes more dominant. Reproduced from [25].

Prediction of the atomic-scale structures and shape of GP zones (such as the monolayer discs described in the introduction) is challenging. The use of continuum elasticity plus empirical interfacial energies [14] or the phase field method based on diffuse interface treatment [15], [16] have been used to study larger precipitate shapes and orientations. However, these methods are not suitable for the present case because the *atomic-scale treatments* of both short-range chemical interactions and long-range coherency strain interactions are required when the definition of an interface is unclear. Recently the critical role of coherency strain in the formation of GP zones in Mg-Nd alloy was reported [17] using direct DFT calculations, which is limited by the DFT cell size (hundreds of atoms).

Here we propose to use the cluster expansion (CE) and further mixed-space cluster expansion (MSCE) technique pioneered by Zunger et al. [18], parameterized by first-principles calculations based on DFT, to study GP zones. CE is a mature statistical mechanics-based method used to calculate the configurational thermodynamics of alloys with an Ising-like Hamiltonian with short-range chemical interactions [19], [20], while the MSCE technique includes the long-range coherency strain energy contributions using a concentration-wave formalism in reciprocal space [18], [21]. The mixing of short-range chemical interaction in the real space with the long-range elastic interaction in the reciprocal space is what makes the proposed MSCE method novel. With this method, it is capable to calculate GP zone sizes, shapes, orientation relationships, metastable phase diagrams, ground state structures, and thermodynamic functions. These results can be corroborated by molecular dynamics simulation in larger time and special scale and passed as an input for crystal plasticity simulations, which will in-turn be experimentally validated by macroscopic property measurements.

Specifically, the proposed modeling aims to study the configurational thermodynamics of hexagonal closed packed (hcp) RE-free Mg-Zn binary and Mg-Zn-Ca ternary systems. We first use CE to search for ground states in the vast configuration space and identify potential coherent early-stage precipitates in Mg-Zn and Mg-Zn-X (X = Nd, Ca) systems, with the emphasis on the atomic structures and thermodynamic properties (configurational and vibrational) of GP zones as a function of chemical composition and temperature. We further propose to extend MSCE to model multicomponent (up to ternary) hcp systems, because, so far, MSCE was only applied to binary alloys [22]–[25] and some semiconductor alloys [21] all with cubic symmetry. Based on the energetics from MSCE, the shape of GP zones can be subsequently predicted using Monte Carlo and simulated-annealing techniques [21], [25] (see **Fig. 1.3**). These works will also shed light on the mechanistic understanding of early-stage precipitation sequence in these technologically important systems. The research will consist of the following four components:

1) Search the ground states of the Mg-Zn alloys on hcp lattice using CE and find the potential coherent precipitates (GP zones) at early stage of aging. Calculate the metastable solvi (metastable phase boundaries) of GP zones and analyzing the effect of lattice-mismatch strain on the formation of cohere GP zones;

2) Search the ground states of monolayer GP zones on the basal plane of the Mg matrix in Mg-Zn-Ca system using CE. Calculate fundamental properties of properties of the predict GP zones: formation enthalpy, lattice parameters, displacement fields around GP zones.

3) Explore the structures of all precipitates in ternary Mg-Zn-Ca system based on the experimental observations, i.e., HAADF-STEM, 3D-APT and diffraction patterns. Focus on the early-stage coherent precipitates, which closely related with monolayer GP zones. Analyze the energy change during the precipitation process.

4) Extend the model of MSCE to ternary hexagonal lattice by incorporating long-range strain effects into traditional CE. Doing CE for the ternary Mg-Zn-Ca system and analyze the effect of large lattice mismatch on the convergence of CE predict the low energy phases in this system and compare with experiments.

1.3 Thesis Organization

The contents of this thesis are organized as follows. Chapter 2 is the methodology section. It includes a detailed methodology for configurational thermodynamics modeling using cluster expansion based on first-principles calculations. Chapter 3 presents the prediction of GP zone structures in binary Mg-Zn system, which is the basis for many widely used commercial Mg alloys. The coherency strain of GP zones is analyzed. In this chapter, the structures and stabilities of other precipitates, i.e., $\beta 1'$ and β_2', are also analyzed in addition to GP zones. Chapter 4 presents the prediction of the structures of GP zones in Mg-Zn-Ca and Mg-Zn-Nd ternary alloys. The predicted structures show similarity with the previous experimentally reported ones but the difference is reported based on the energetic trends. Chapter 5 focused on the precipitates formed during aging process of Mg-0.6Zn-0.3Ca ternary alloy aged at 200 C. The structures of precipitates in peak-aged stage, i.e., GP zones, and those formed following GP zones are explored. The DFT energies are used to analyze the stabilities of precipitates, and simulated TEM and Diffraction patterns are used to confirm the predicted structures. Chapter 6 presents the extension of MSCE method from cubic lattice to systems with arbitrary lattice. The effect of coherency strain on the morphology of precipitates in Mg-Zn system is shown, and the predictability of MSCE is tested on this system compared with traditional CE. Chapter 7 presents the extension of MSCE method to multicomponent systems. The mathematical details of the development process are the focus. Finally, Chapter 8 concludes this thesis by presenting a summary of all the work and recommendation for the future work.

Reference

[1] K. Hantzsche, J. Bohlen, J. Wendt, K. U. Kainer, S. B. Yi, and D. Letzig, “Effect of rare earth additions on microstructure and texture development of magnesium alloy sheets,” Scr. Mater. 63 (2010) 725–730.

[2] J. Bohlen, M. R. Nürnberg, J. W. Senn, D. Letzig, and S. R. Agnew, “The texture and anisotropy of magnesium-zinc-rare earth alloy sheets,” Acta Mater.55 (2007) 2101–2112.

[3] S. Jiang, H. Wang, Y. Wu, X. Liu, H. Chen, M. Yao, B. Gault, D. Ponge, D. Raabe, A. Hirata, M. Chen, Y. Wang, Z. Lu. "Ultrastrong steel via minimal lattice misfit and high-density nanoprecipitation." Nature 544 (2017): 460-464.

[4] M. Z. Bian et al., “Bake-hardenable Mg–Al–Zn–Mn–Ca sheet alloy processed by twin-roll casting,” Acta Mater. 158 (2018) 278–288.

[5] M. Cihova et al., “Rational design of a lean magnesium-based alloy with high age-hardening response,” Acta Mater.158 (2018) 214–229.

[6] T. Nakata et al., “Strong and ductile age-hardening Mg-Al-Ca-Mn alloy that can be extruded as fast as aluminum alloys,” Acta Mater.130 (2017) 261–270.

[7] J. F. Nie, N. C. Wilson, Y. M. Zhu, and Z. Xu, “Solute clusters and GP zones in binary Mg-RE alloys,” Acta Mater. 106 (2016) 260–271.

[7] J. J. Bhattacharyya, T. Nakata, S. Kamado, and S. R. Agnew, “Origins of high strength and ductility combination in a Guinier-Preston zone containing Mg-Al-Ca-Mn alloy,” Scr. Mater. 163 (2019) 121–124.

[8] J. F. Nie, “Precipitation and hardening in magnesium alloys,” Metall. Mater. Trans. A. Phys. Metall. Mater. Sci. 43 (2012) 3891–3939.

[9] J. Jayaraj, C. L. Mendis, T. Ohkubo, K. Oh-Ishi, and K. Hono, “Enhanced precipitation hardening of Mg-Ca alloy by Al addition,” Scr. Mater. 63 (2010) 831–834.

[10] K. Oh-ishi, R. Watanabe, C. L. Mendis, and K. Hono, “Age-hardening response of Mg-0.3 at.%Ca alloys with different Zn contents,” Mater. Sci. Eng. A. 526 (2009) 177–184.

[11] C. Q. Liu, H. W. Chen, H. Liu, X. J. Zhao, and J. F. Nie, “Metastable precipitate phases in Mg–9.8 wt%Sn alloy,” Acta Mater. 144 (2018) 590–600.

[12] U. F. Kocks, A. S. Argon, and M. F. Ashby, Thermodynamics and kinetics of slip, 19 (1975).

[13] J. F. Nie, “Effects of precipitate shape and orientation on dispersion strengthening in magnesium alloys,” Scr. Mater. 48 (2003) 1009–1015.

[14] J. K. Lee, D. M. Barnett, and H. I. Aaronson, “The elastic strain energy of coherent ellipsoidal precipitates in anisotropic crystalline solids,” Metall. Trans. A. 8 (1977) 963–970.

[15] H. Liu, Y. Gao, J. Z. Liu, Y. M. Zhu, Y. Wang, and J. F. Nie, “A simulation study of the shape of β′ precipitates in Mg-Y and Mg-Gd alloys,” Acta Mater. 61 (2013) 453–466.

[16] Y. Z. Ji, A. Issa, T. W. Heo, J. E. Saal, C. Wolverton, and L. Q. Chen, “Predicting β′ precipitate morphology and evolution in Mg-RE alloys using a combination of first-principles calculations and phase-field modeling,” Acta Mater. 76 (2014) 259–271.

[17] A. R. Natarajan, E. L. S. Solomon, B. Puchala, E. A. Marquis, and A. Van Der Ven, “On the early stages of precipitation in dilute Mg-Nd alloys,” Acta Mater.108 (2016) 367–379.

[18] D. B. Laks, L. G. Ferreira, S. Froyen, and A. Zunger, “Efficient cluster expansion for substitutional systems,” Phys. Rev. B. 46 (1992) 12587–12605.

[19] D. de Fontaine, “Configurational Thermodynamics of Solid Solutions,” Solid State Phys. - Adv. Res. Appl. 34 (1979) 73–274.

[20] D. De Fontaine, “Cluster approach to order-disorder transformations in alloys,” Solid State Phys. 47 (1994) 33–176.

[21] Z. W. Lu, D. B. Laks, S. H. Wei, and A. Zunger, “First-principles simulated-annealing study of phase transitions and short-range order in transition-metal and semiconductor alloys,” Phys. Rev. B. 50 (1994) 6642–6661.

[22] S. Müller, C. Wolverton, L. W. Wang, and A. Zunger, “Predicting the size- and temperature-dependent shapes of precipitates in Al-Zn alloys,” Acta Mater. 48 (2000) 4007–4020.

[23] S. Müller, C. Wolverton, L. W. Wang, and A. Zunger, “Prediction of alloy precipitate shapes from first principles,” Euro. phys. Lett. 55 (2001) 33–39.

[24] C. Wolverton, L. W. Wang, and A. Zunger, “Coherent phase stability in Al-Zn and Al-Cu fcc alloys: the role of the instability of fcc Zn,” Phys. Rev. B. - Condens. Matter Mater. Phys. 60 (1999) 16448–16462.

[25] C. Wolverton, “First-principles theory of 250,000-atom coherent alloy microstructure,” Model. Simul. Mater. Sci. Eng. 8 (2000)323–333.

Chapter 2 Computational Methodology

2.1 First-principles Calculations based on the Density Functional theory

Density functional theory (DFT) calculations are often known as “ab-initio” calculations. It calculates energies “from first principles”, sicne the inputs are the basic physical information of the atoms, e.g., atomic coordinates and atomic numbers, and it does not rely on any experimental or empirical data. The total energy of the targeted system is then determined by using quantum mechanical electronic theory. Instead of solving complex multi-body Schrödinger equations in quantum mechanics, DFT uses the electron density to describe the intricate many-body effects within a single particle formalism and enables the application in real system possible. As evidenced by some recent reports, the number of DFT applications is growing rapidly by the year and some of the latest, and most significant studies include the following: the understanding and design of catalytic processes in enzymes and zeolites, electron transport, solar energy harvesting and conversion, drug design in medicine. Here we focus on the thermodynamic properties of alloys calculated by DFT, i.e., enthalpy and entropy of formation, use them to study thermodynamic stabilities of phases formed during the thermomechanical processing, and finally control the microstructures of alloys to reach desired macro properties.

2.1.1 Density Functional Theory

The Schrödinger equation that describes the quantum nature of matter is:

$$\hat{H}\Psi = E\Psi \tag{2.1}$$

where the Hamiltonian, $\hat{H}$, for a Coulombic system described by the interacting positively charged nuclei and negatively charged electrons, is given by:

$$\hat{H} = -\sum_i \frac{\hbar^2}{2m}\nabla_i^2 - Ze^2 \sum_i \frac{1}{|r_i - r_A|} + e^2 \sum_{i>j} \frac{1}{|r_i - r_j|} \tag{2.2}$$

with a specified set of nuclei with charges Z and positions r_A and number of electrons $i = N$. The task is to simply minimize the energy over all possible anti-symmetric wave functions, $\Psi(x_1, x_2, \ldots, x_i, \ldots\ x_N)$, where x_i contains the spatial coordinate r_i and spin coordinate σ_i. This enables us to find the minimizing Ψ and hence the ground state energy, E. Here the nuclei-nuclei interaction energy in the above is neglected, which would have to be added in order to yield the total energy of the system. However, the Born-Oppenheimer approximation allows us to decouple the nuclear and electronic degrees of motion; the nuclei are of order ~ 10^3 – 10^5 times massive than the electrons, and therefore can be treated as stationary on the electronic timescale. As a result of this, it is possible to neglect the nuclear kinetic energy contribution to the system energy. Although this equation is exact within the non-relativistic regime, it is not possible, except for trivially simple case, to solve it. There are two reasons for this: one mole of a solid contains N ~ 1028 electrons; since the many-electron wave function contains 3N degrees of freedom, this is simply intractable; further, the electron - electron Coulomb interaction results in the electronic motions being correlated.

In DFT, the problem is reformulated in a philosophically and computationally different manner [1]. The foundation of DFT is the Hohenberg-Kohn theorem [2], which states that the external potential is a functional of the ground-state density. In other words, the density (an observable in 3D space) is used to describe the complicated physics behind the interactions between electrons and, therefore, determines everything about the system. In Kohn-Sham (KS) theory [3], this is formulated as a simple expression for the ground state energy:

$$E(\rho(\boldsymbol{r})) = T_s\big(\rho(\boldsymbol{r})\big) + V_{ne}\big(\rho(\boldsymbol{r})\big) + J_{ee}\big(\rho(\boldsymbol{r})\big) + E_{xc}(\rho(\boldsymbol{r})) \tag{2.3}$$

where the forms of some of the functionals are explicitly known. The electron density of the KS reference system is given by:

$$\rho(r) = \sum_i |\phi_i(r)|^2 \tag{2.4}$$

The kinetic energy for the KS non-interacting reference system is:

$$T_s(\rho(\boldsymbol{r})) = \sum_i \left\langle \phi_i \middle| -\frac{\hbar^2}{2m} \nabla_i^2 \middle| \phi_i \right\rangle \tag{2.5}$$

in terms of $\{\phi_i\}$, the set of one electron KS orbitals. The other two known energy components are the nucleus electron potential energy, expressed in terms of the external potential due to the nuclei,

$$V_{ne}\big(\rho(\boldsymbol{r})\big) = \int \rho(\boldsymbol{r}) V(\boldsymbol{r})\, d\boldsymbol{r} \tag{2.6}$$

and the classical electron-electron repulsion energy,

$$J_{ee}(\rho(\boldsymbol{r})) = \frac{1}{2} \iint \frac{\rho(\boldsymbol{r})\rho(\boldsymbol{r}')}{|\boldsymbol{r}-\boldsymbol{r}'|} d\boldsymbol{r} d\boldsymbol{r}' \tag{2.7}$$

The key remaining term, the exchange-correlation functional $E_{xc}(\rho(\boldsymbol{r}))$, includes not only the exchange and correlation energy of interacting electrons, but also the difference between T and Ts. Although no explicit form is available, it can be expressed in the constrained search formulation for density functionals [4],

$$E_{xc}\big(\rho(\boldsymbol{r})\big) = \min_{\Psi\to\rho}\langle\Psi|T + V_{ee}|\Psi\rangle - T_s\rho(\boldsymbol{r}) - J_{ee}(\rho(\boldsymbol{r})). \tag{2.8}$$

Many density functional approximations have been developed for real case applications. One of the very early and most widely used approximation is the Local Density Approximation (LDA), which assumes that the exchange-correlation energy is only a functional of the local density of electrons. The functional for correlation was not derived from first principles, instead Monte Carlo simulations of the uniform gas [5] were used to parametrize interpolations between the known forms in the high- and low-density limits. There exist widely used LDA correlation functionals developed by Voskoet [6] and Perdew [7]. The uniform electron gas, although a beautiful model system that has played a key role in the development of functionals, has an incredibly different density to those found in atomic or molecular systems. Therefore, another widely used approximation is the Generalized Gradient Approximation (GGA), which attempts to incorporate the effects of inhomogeneity by including the gradient of the electron density. Unlike LDA, GGA has no unique functional form, and indeed many variations are possible, each corresponding to a different enhancement factor. Currently, there are two main functionals that are well-established, LYP [8] and PBE [9]. Further to improve the exchange-correlation functionals, the next obvious step was to include higher-order derivatives of the density. The term meta-GGA was coined by Perdew and Schmidt when they proposed the famous Jacob’s ladder of approximations [10] to the exact exchange-correlation functional. This is a ladder of functionals improves the accuracy of DFT within 1 kcal/mol for energetics. This concept in functional development has stimulated and inspired many ideas. Another clear advance in the development of exchange-correlation functionals is the inclusion of some Hartree-Fock exchange into the functional. The original idea proposed a linear model to mix some Hartree-Fock exchange with local density functional approximation and correlation type functionals. This gave rise to functionals like BHLYP [11]. Efforts to improve the accuracy of exchange-correlation functionals are still going on, and many new functionals are not detailed in current chapter.

2.1.2 DFT settings in VASP

In current thesis, First-principles calculations based on density functional theory [2,3] were employed to optimize the ground-state structures and calculate the energies. The ion-electron interaction was described by the projector augmented plane-wave method [12] and the exchange-correlation functional was described by an improved general gradient approximation of Perdew-Burke-Ernzerhof [13], as implemented in the Vienna ab initio simulation package (VASP, version 5.4) [14,15]. An energy cutoff of 400 eV was adopted for the plane-wave expansion of the electronic wave functions. The Methfessel-Paxton technique was adopted with smearing parameter of 0.2 eV for integration over k points [16]. The Brillouin zone was sampled by Gamma-centered grids with the k points per reciprocal atom over 8000 [17]. For all the configurations under consideration, all degrees of freedom for the cell, i.e., volume, shape, and internal atomic positions, are allowed to relax for structural optimization. To improve the accuracy of energy calculations, static calculations with the tetrahedron method incorporating Blöchl correction [18] were adopted after structural relaxations.

2.2 Cluster Expansion

DFT calculations provide formation energies at 0 K. To obtain thermodynamic information at finite temperature, sampling of all excited states in thermodynamic equilibrium is required, but directly calculation based on quantum mechanics is computationally prohibitive. Therefore, in solid-state alloys, this issue is solved by the coarse-graining concept and cluster expansion formulism. The idea is to build a simple Hamiltonian that can be used to sample excited configurational, vibrational, and electronic states at finite temperature. This Hamiltonian is expected to be more accurate than empirical potentials, since they focused specific atomic configurations and take the form of a complete and systematically improvable expansion [19].

In statical mechanics, all thermodynamic properties of a system can be obtained from its partition function Z. In crystalline alloys, the partition function including all possible states can be factored as,

$$Z = \sum_{\sigma \in L} \sum_{v \in \sigma} \sum_{e \in v} \exp\{-\beta E(L, \sigma, v, e)\} \tag{2.9}$$

where $\beta = (k_B T)^{-1}$ and σ denotes a configuration on a given lattice L. v denotes a displacement of atoms from their ideal sites of the lattice. e denotes the electronic state when the ions are constrained to be in a state of σ and v. E is the energy of the state (L, σ, v, e).

Each summation defines an increasingly coarser level of hierarchy in the set of microscopic states. The free energy of the system on lattice L and temperature T can be written as,

$$F(L, T) = -k_B T \ln(\sum_{\sigma \in L} \exp\{-\beta F(L, \sigma, T)\}) \tag{2.10}$$

The coarse graining of the partition function enables an exact mapping of a real alloy onto a simple lattice model described a temperature-dependent Hamiltonian $F(L, T)$, as shown in **Fig. 2.1**. In this way, the system's energy is a constrained free energy as a function of only the lattice L and configurations σ.

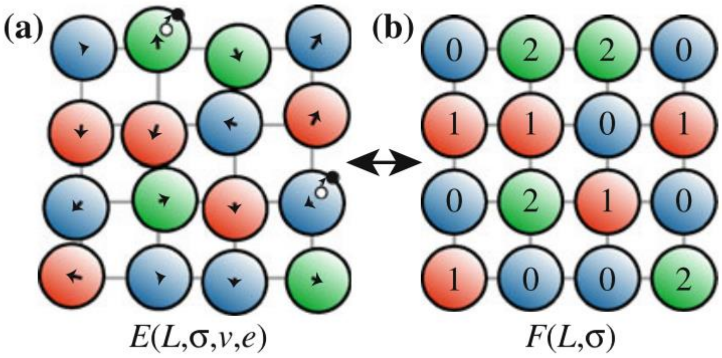

Fig. 2.1 The process of coarse graining from a real alloy (a) exhibiting configurational disorder(colors), vibrational excitations (arrows), and electronic excitations (open and filled black circles) to a lattice model (b) in which only the configurational degrees of freedom. The figure is from [19].

Although the coarse graining reduces the configurationally disordered system to a more tractable calculations for a lattice model, but it still needs to calculate of energies for each possible configuration, which is computationally intractable. This issue is solved by a convenient strategy cluster expansion. Cluster expansion reproduces the lattice property value by expand that property as a linear combination of the basis functions known as correlation functions. [20] These basis functions form an orthogonal basis for the space of functions of descriptors according to a suitably defined inner product. [21] A simple set of correlation functions are products of spin variables of all sites within a cluster on a given lattice. The expansion coefficient represents the interaction between sites within a cluster. Therefore, the cluster expansion is an analytical method which can efficiently accelerate the calculation of property values with a high accuracy due to a large number of basis functions.

Here the cluster expansion Hamiltonians is used to describe the configurational thermodynamics of Mg-Zn and Mg-Zn-X alloys on the hcp lattice. For an alloy with the number of allowed species on site i of M_i, the spin variables, σ_i , to each crystal site i takes a value from 0 to $M_i - 1$. Then, the formation energy of a given atomic configuration on the fixed parent lattice can be cast into the general form [22]:

$$E_f(\vec{\sigma}) = \sum_\alpha m_\alpha J_\alpha \prod_i \gamma_{\alpha_i,M_i}(\sigma_i) \tag{2.11}$$

where α is a cluster and described by a vector of elements α_i, which take value from 0 to $M_i - 1$, with 0 indicating that site i does not belong to cluster α, while other values reflect various functional form dependence of the energy on cluster α. m_α are multiplicities indication the number of clusters equivalent to α by symmetry, J_α are expansion coefficient, or effect cluster interactions (ECIs), $\gamma_{\alpha_i,M_i}(\sigma_i)$ are used the form of default setting in ATAT:

$$\gamma_{\alpha_i,M_i}(\sigma_i) = \begin{cases} 1, \ \alpha_i = 0 \\ -\cos\left(2\pi\lceil\alpha_i\rceil \frac{\sigma_i}{M_i}\right), \alpha_i > 0 \ and \ odd \\ -\sin\left(2\pi\lceil\alpha_i\rceil \frac{\sigma_i}{M_i}\right), \alpha_i > 0 \ and \ even \end{cases} \tag{2.12}$$

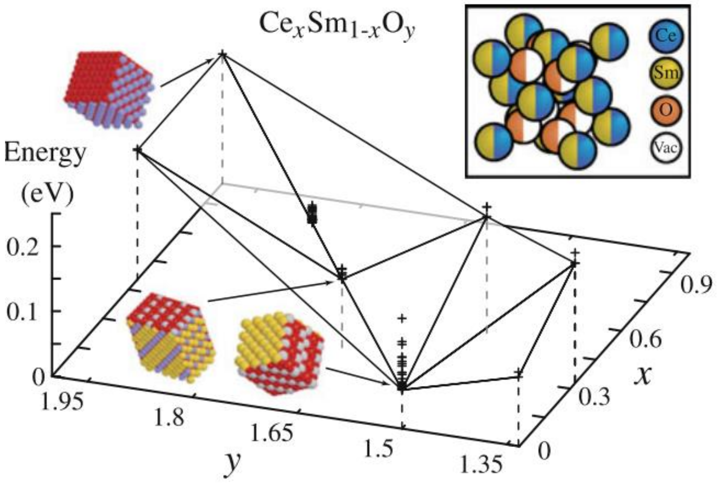

Fig. 2.2 Example of application of the cluster expansion formalism to the study of (a) ground-state structures via a convex hull construction. The figure is adapted from [19].

In binary systems, the single site functional forms for the two species indexed by 0 and 1, respectively, are $\gamma_{1,2}(0) = -1$ and $\gamma_{1,2}(1)$=1. This result is consistent with the commonly used spin variables in binary cases.

The unknow parameters in the cluster expansion, the ECI J, can be determined by fitting them to the energies calculated by DFT for s small number of configurations. Once the ECI is determined, the free energy for all configuration can be easily predicted. Therefore, there is no need to calculate energies for all possible configurations from the expensive DFT. This is also particularly useful to determine the ground states of an alloy system (the lowest energy structure, or mixture of structures, at each composition) because many candidate structures can be quickly screened for a low energy without resorting to ab initio calculations. An example application of cluster expansion in a ternary system is given in **Fig. 2.2**.

2.3 Coherency strain energy

In some alloy systems, convergence of the cluster expansion to a useful accuracy may necessitate the inclusion of long-ranged interatomic interactions, due to, e.g., electrostatic, elastic, or by electronic structure (Fermi-surface) effects. The constituent strain formalism has been proposed as an effective approach to modeling long- ranged elastically mediated interactions. Such elastic effects are known to be particularly important in describing the thermodynamics of mixtures of species with very large differences in atomic “size”.

For a binary system with composition x, the coherency strain energy (CSE) $\Delta E_{CS}\left(\vec{k}, x\right)$ on the plane of normal $\vec{k}$ can be calculated as the composition averaged strain energies of the two elements in epitaxial configuration [23]. For non-cubic parent lattice with two independent lattice parameters (e.g., HCP), the strain energies (i.e., $\Delta E^{epi}_{\mathrm{Mg/Zn}}(\vec{k}, a_1, a_2)$) are obtained from biaxially deformed elements from their own lattice parameters on the epitaxial plane $\vec{k}$ (i.e., $a_1^{\mathrm{Mg}}, a_2^{\mathrm{Mg}}, a_1^{\mathrm{Zn}}$ and a_2^{Zn}) to the common in-plane lattice parameters (i.e., a_1 and a_2) and relaxed in the $\vec{k}$ direction [24–26]:

$$\Delta E^{HCP}_{CS}(\vec{k}, x) = \min_{a_1, a_2}[(1-x)\Delta E^{epi}_{\mathrm{Mg}}(\vec{k}, a_1, a_2) + x\Delta E^{epi}_{\mathrm{Zn}}(\vec{k}, a_1, a_2)] \tag{2.13}$$

Noted that, for the basal plane, only one independent in-plane lattice parameter, i.e., a, is needed for optimization, while for the other planes, two independent in-plane lattice parameters are needed. Based on the symmetry of HCP lattice, 3 symmetrically distinct crystallographic planes are chosen to analyze the anisotropy of CSE, including basal plane ($\{0001\}$), and two prismatic planes ($\{10\bar{1}0\}$ and $\{11\bar{2}0\}$).

Here two approaches are adopted to obtain the epitaxial strain energy $\Delta E^{epi}(\vec{k}, a_1, a_2)$ in Eq.(2), namely DFT and linear elasticity theory (or harmonic elasticity theory [23,25]). The DFT calculations can capture the anharmonic elastic response of the biaxial deformation [25–27], while the linear elasticity theory only consider the linear elastic response (or harmonic effects) of solid under small lattice distortions within elastic response limit[28,29]. If the lattice mismatch is sufficiently small, $\Delta E^{epi}(\vec{k}, a_1, a_2)$ from DFT and the linear elastics would coincide with each other. Therefore, linear elastic result is a reference to reflect the anharmonic effect from DFT result. In linear elasticity theory, $\Delta E^{epi}(\vec{k}, a_1, a_2)$for the constituent Mg or Zn follows [25],

$$\Delta E^{epi}_{\mathrm{Mg/Zn}}(\varepsilon_2', \varepsilon_3') = \frac{V_0}{2}\begin{bmatrix} C_{22}'{\varepsilon_2'}^2 + C_{12}'\varepsilon_2'\left(\dfrac{C_{12}'\varepsilon_2' + C_{13}'\varepsilon_3'}{-C_{11}'}\right) + 2C_{32}'\varepsilon_2'\varepsilon_3' \\ +C_{13}'\varepsilon_3'\left(\dfrac{C_{12}'\varepsilon_2' + C_{13}'\varepsilon_3'}{-C_{11}'}\right) + C_{33}'\varepsilon_3' \end{bmatrix} \tag{2.14}$$

where ε_2' and ε_3' are the two independently optimized strains on the epitaxial plane, and C_{ij}' is the elastic stiffness tensor in Voigt notation with respect to the in-plane coordinate system, with C_{11}' being the out-of-plane stiffness [25]. The elastic stiffness tensor is calculated from DFT with normal and shear strain of 1%, and transformed to the in-plane coordinate system [30]. Note that all primed variables are functions of plane normal $\vec{k}$, which accounts for the anisotropy of elasticity.

2.4 Mixed-space cluster expansion

For most configurations, atoms move away from the ideal lattice sites with lowering energies. However, allowing these relaxations will slow down the convergence of CE. This will later be proven to be accelerated by considering the singularity of the macroscopic elastic strain at the zone-center Γ in reciprocal space. With the long-range strain effect incorporated in reciprocal space and short-range chemical interaction described in conventional real space CE, the method is called mixed-space cluster expansion (MSCE). It was originally developed in the research group led by Zunger [23] and subsequently applied by co-workers: Müller [31], [32], Ozolins [33], Wolverton [34], [35], and J.Z. Liu [36], [37]. The expression of the formation enthalpy of any configuration σ in MSCE is:

$$\Delta H_{MSCE}(\sigma) = E_{pair}(\sigma) + E_{multibody}(\sigma) + E_{CS}(\sigma)$$

$$= \sum_{\boldsymbol{k}} J_{pair}(\boldsymbol{k})|S(\boldsymbol{k},\sigma)|^2 + \sum_f D_f J_f \prod_f(\sigma) + \frac{1}{4x(1-x)} \sum_{\boldsymbol{k}} \Delta E_{CS}^{eq}(\hat{k},x)|S(\boldsymbol{k},\sigma)|^2 \qquad (2.15)$$

where $J_{pair}(\boldsymbol{k})$ and J_f are the Ising-like interaction energies, f is a symmetry-distinct figure comprised of several lattice sites (pairs, triplets, etc.) and thus is the same as α defined previously, D_f indicates the number of symmetrically equivalent clusters of f, $\prod_f(\sigma)$ are correlation functions[38] (spin products in the binary cases). The first term $E_{pair}(\sigma)$ includes all pair figures, where $J_{pair}(\boldsymbol{k})$ and $S(\boldsymbol{k},\sigma)$ are lattice Fourier transforms of real-space pair interactions and spin-occupation variables. These pair interactions are conveniently summed using the reciprocal-space concentration-wave formalism. The second term includes only non-pair figures. The real-space summation of the second term is over f. These first two terms include all the information about different chemical interactions characterized by effective cluster interactions $J_{pair}(\boldsymbol{k})$ and J_f. However, the strain energy (due to the lattice mismatch) necessary to maintain coherency at an interface between regions of pure A and B cannot be expressed by these finite-ranged J values. Consequently, the third term involves $\Delta E_{CS}^{eq}(\hat{k},x)$, the constituent strain energy, defined as the energy change when the bulk solids A and B are deformed from their equilibrium lattice constants a_A and a_B to a common lattice constant $a_\perp$ perpendicular to $\hat{k}$:

$$\Delta E_{CS}^{eq}(\hat{k},x) = \min_{a_\perp}\left[(1-x)\Delta E_A^{epi}(\hat{k},a_\perp) + x\Delta E_B^{epi}(\hat{k},a_\perp)\right] \tag{2.16}$$

where $\Delta E_A^{epi}(\hat{k},a_\perp)$ is the energy required to deform A biaxially to $a_\perp$. The constituent strain energy corresponds to the $\boldsymbol{k} \rightarrow 0$ limit of $J(\boldsymbol{k})$ and takes on different values depending on the direction in which this limit is taken, which thus corresponds to infinite-range real-space elastic interaction terms.

Reference

[1] A. J. Cohen, P. Mori-Sanchez, W. Yang, Challenges for density functional theory, Chem. Rev., 63 (2012) 289–320.

[2] P. Hohenberg; W Kohn, Inhomogeneous electron gas, Phys. Rev. 136 (1964) 864.

[3] W. Kohn, L. J. Sham, Self-consistent equations including exchange and correlation effects, Phys. Rev. 140 (1965) 1133.

[4] M Levy, Universal variational functionals of electron densities, first-order density matrices, and natural spin-orbitals and solution of the v-representability problem, Proc. Natl. Acad. Sci. 76 (1979) 6062.

[5] D. M. Ceperley, B. J. Alder, Ground state of the electron gas by a stochastic method, Phys. Rev. Lett. 45 (1980) 566.

[6] S. H. Vosko, L. Wilk, M. Nusair, Accurate spin-dependent electron liquid correlation energies for local spin density calculations: a critical analysis, Can. J. Phys. 58 (1980) 1200.

[7] J. P. Perdew; Y. Wang, Accurate and simple analytic representation of the electron-gas correlation energy, Phys. Rev. B 45 (1992) 13244.

[8] C. T. Lee, W. T. Yang, R. G. Parr, Development of the Colle-Salvetti correlation-energy formula into a functional of the electron density, Phys. Rev. B 37 (1988) 785.

[9] J. P. Perdew, K. Burke, M. Ernzerhof, Generalized gradient approximation made simple, Phys. Rev. Lett. 77 (1996) 3865.

[10] J. P. Perdew, K. Schmidt, Jacob’s ladder of density functional approximations for the exchange-correlation energy, AIP Conference Proceedings, American Institute of Physics, 577 (2001) 1-20.

[11] A.D. Becke, A new mixing of Hartree–Fock and local density-functional theories, Chem. Phys, 98 (1993) 1372.

[12] D. Joubert, From ultrasoft pseudopotentials to the projector augmented-wave method, Phys. Rev. B. 59 (1999) 1758–1775.

[13] J. P. Perdew, K. Burke, M. Ernzerhof, Generalized gradient approximation made simple, Phys. Rev. Lett. 77 (1996) 3865–3868.

[14] G. Kresse, Efficient iterative schemes for ab initio total-energy calculations using a plane-wave basis set, Phys. Rev. B. 54 (1996) 11169–11186.

[15] G. Kresse, J. Furthmüller, Efficiency of ab-initio total energy calculations for metals and semiconductors using a plane-wave basis set, Comput. Mater. Sci. 6 (1996) 15–50.

[16] M. Methfessel, A.T. Paxton, High-precision sampling for Brillouin-zone integration in metals, Phys. Rev. B. 40 (1989) 3616–3621.

[17] A. Van de Walle, M. Asta, G. Ceder, The alloy theoretic automated toolkit: A user guide, CALPHAD. 26 (2002) 539–553.

[18] P.E. Blöchl, O. Jepsen, O.K. Andersen, Improved tetrahedron method for Brillouin-zone integrations, Phys. Rev. B. 49 (1994) 16223–16233.

[19] A. van de Walle, Methods for first-principles alloy thermodynamics, Jom 65 (2013) 1523-1532.

[20] T. Mueller and G. Ceder, Bayesian approach to cluster expansions, Phys. Rev. B 80 (2009) 1–13.

[21] A. Van der Ven, G. Ceder, M. Asta, and P. D. Tepesch, First-principles theory of ionic diffusion with nondilute carriers, Phys. Rev. B 64 (2001) 1–17.

[22] A. van de Walle, Multicomponent multisublattice alloys, non-configurational entropy and other additions to the Alloy Theoretic Automated Toolkit, Calphad 33 (2009) 266–278.

[23] D. B. Laks, L.G. Ferreira, S. Froyen, A. Zunger, Efficie cluster expansion for substitutional systems, Phys. Rev. B. 46 (1992) 12587.

[24] C. N. Varney, G.L.W. Hart, C. Wolverton, A Coherency Strain Model for Hexagonal-Close-Packed Alloys, TMS Lett. 1 (2005) 35–36.

[25] A. Issa, J.E. Saal, C. Wolverton, Physical factors controlling the observed high-strength precipitate morphology in Mg-rare earth alloys, Acta Mater. 65 (2014) 240–250.

[26] K. Wang, D. Cheng, B. Zhou, Generalization of the mixed space cluster expansion method for arbitrary lattices, submitted to npj Computational Materials, (2022).

[27] V. Ozoliņš, C. Wolverton, A. Zunger, Effects of anharmonic strain on the phase stability of epitaxial films and superlattices: Applications to noble metals, Phys. Rev. B. 57 (1998) 4816–4828.

[28] S. Shang, Y. Wang, Z.K. Liu, First-principles elastic constants of α- And θ- Al2O3, Appl. Phys. Lett. 90 (2007) 1–4.

[29] M. De Jong, W. Chen, T. Angsten, A. Jain, R. Notestine, A. Gamst, M. Sluiter, C.K. Ande, S. Van Der Zwaag, J.J. Plata, C. Toher, S. Curtarolo, G. Ceder, K.A. Persson, M. Asta, Charting the complete elastic properties of inorganic crystalline compounds, Sci. Data. 2 (2015) 1–13.

[30] Robert E Newham, Properties of Materials Anisotropy, Symmetry, Structure, Oxford University Press, 2005.

[31] S. Müller, C. Wolverton, L. W. Wang, and A. Zunger, Predicting the size- and temperature-dependent shapes of precipitates in Al-Zn alloys, Acta Mater. 48 (2000) 4007–4020.

[32] S. Müller, C. Wolverton, L. W. Wang, and A. Zunger, Prediction of alloy precipitate shapes from first principles, Euro. phys. Lett., 55 (2001) 33–39.

[33] V. Ozoliņš, C. Wolverton, and A. Zunger, Cu-Au, Ag-Au, Cu-Ag, and Ni-Au intermetallics: First-principles study of temperature-composition phase diagrams and structures, Phys. Rev. B 57 (1998) 6427–6443.

[34] C. Wolverton, L. W. Wang, and A. Zunger, Coherent phase stability in Al-Zn and Al-Cu fcc alloys: the role of the instability of fcc Zn, Phys. Rev. B 60 (1999) 16448–16462.

[35] C. Wolverton, First-principles theory of 250,000-atom coherent alloy microstructure, Model. Simul. Mater. Sci. Eng., 8 (2000) 323–333.

[36] J. Z. Liu and A. Zunger, Thermodynamic states and phase diagrams for bulk-incoherent, bulk-coherent, and epitaxially-coherent semiconductor alloys: Application to cubic (Ga,In)N, Phys. Rev. B, 77 (2008) 1–12.

[37] J. Z. Liu, G. Trimarchi, and A. Zunger, Strain-minimizing tetrahedral networks of semiconductor alloys, Phys. Rev. Lett., 99 (2007) 1–4.

[38] L. G. Ferreira, S. H. Wei, and A. Zunger, First-principles calculation of alloy phase diagrams: The renormalized-interaction approach, Phys. Rev. B, 40 (1989) 3197–3231.

Chapter 3 is from the published paper: D. Cheng, K. Wang, B.C. Zhou. “Crystal structure and stability of phase in MgZn: a comprehensive first-principles study.” Acta Mater. (2022): 118443. Author contributions: D. Cheng performed the DFT, CSE and CE calculations, analyzed results and drafted the manuscript. K. Wang performed CE and Monte Carlo simulations and wrote the code for numerical analysis and figure output. B.C Zhou conceived and supervised the project. All authors contributed to discussions on the results and revision of the manuscript.

Chapter 3 stabilities of phases in Mg-Zn alloy

3.1 Introduction

Mg alloys, as the lightest structural metallic materials, have been studied extensively for their wide potential applications in aerospace and automotive industries, where weight is a crucial factor to reduce the energy cost and CO2 emission [1–3]. Among Mg-based alloys, Mg-Zn alloys received tremendous attention due to its precipitation strengthening capability [3], biocompatibility [4,5] and low cost [6]. The maximum solubility of Zn in Mg matrix is 2.4 at.% at 613 K (340 °C) [3], which decreases rapidly with lowering temperature and leads to supersaturated solid solution (S.S.S.S.) [7]. Aging treatment of S.S.S.S. leads to formation of various precipitates that impede the movement of dislocations and improves the strength of the alloy. Biochemically, Mg and Zn species can be absorbed by human body and bivalent ions of Mg and Zn are essential for human metabolism [8,9]. If the absorption rate is properly tuned, Mg-Zn alloys could become a promising candidate for various implants (e.g., bone screws, cardiovascular stent) [9,10]. As for availability, elemental Mg and Zn are abundant and inexpensive compared with rare earth (RE) elements commonly used in Mg alloys [1,6]. Mg-Zn system is also a critical subsystem for commercial Mg alloys, e.g., AZ series (Mg-Al-Zn alloys), ZK series (Mg-Zn-Zr alloys) and ZE series (Mg-Zn-RE alloys) [11] due to Zn's ability to form precipitates with a larger atom in Mg matrix.

Over the years, numerous efforts have been made to understand and tune the microstructures of Mg-Zn alloys since the discovery of its age hardening effect [3,5,20–26,12–19]. Although remarkable progress has been made, the structures and stabilities of the phases in Mg-Zn system are still not well understood. Specifically, there are considerable debates on the exact stoichiometry and details of the atomic structure of the metastable phases in the Mg-Zn system, especially the precipitates in the early stages of aging treatment [3]. In the current Chapter, we review the current knowledge on the phases in Mg-Zn system and identify three key open questions on phase structure and stability (Chapter 2.3). Then, comprehensive first-principles calculations based on density functional theory (DFT)[27,28], cluster expansion (CE) [29] and Monte Carlo (MC) [30] are performed to fill the knowledge gap and answer these questions from computational perspectives. The results are discussed (Chapter 3.3), including the overall phase structures and stabilities, potential GP zones, effect of lattice mismatch and formation of incoherent precipitates. Finally, a precipitation sequence is proposed by summarizing the experimental information in the literature and insights from current calculations (Chapter 3.4).

3.2 Literature Review

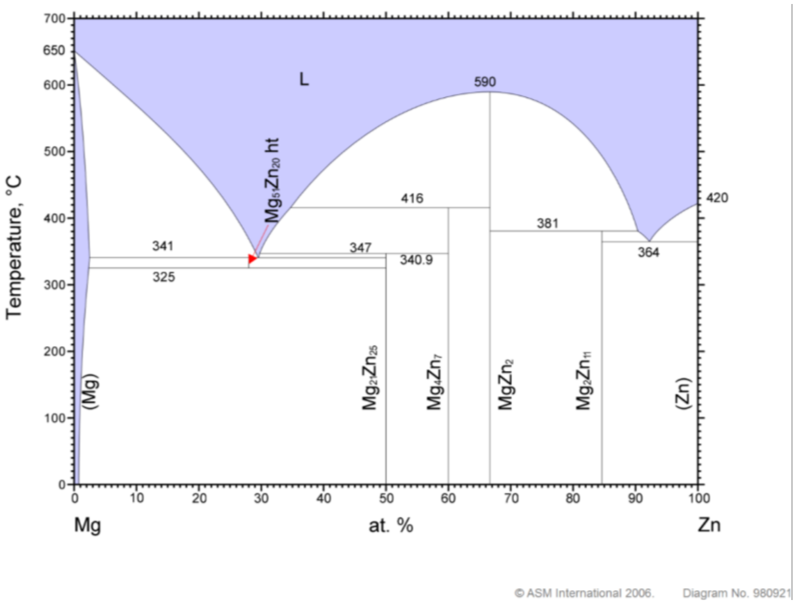

© ASM International 2006. Diagram No. 980921

Fig. 3.1 Phase diagram of Mg-Zn system [7], retrieved from the ASM Alloy Phase Diagram Database.

The crystallography of phases and their microstructures in Mg-Zn alloys during processing often display a rich variety of complexity. In this Section, a critical review on the research status is given on the intermetallic compounds and precipitates in Mg-Zn alloys. The categorization of structures into intermetallic compounds and precipitates is due to the terminologies in different research communities (e.g., crystallography and metallurgy), despite the overlapping of concepts. The intermetallic compounds are reviewed in Sec. 2.1 focusing on the crystallographic aspect, while the review on precipitations focuses on the microstructures in aging process. The phase diagram of Mg-Zn system by Okamoto is shown in **Fig. 3.1** for an overview of the phase relation [7].

3.2.1 Intermetallic compounds

$Mg_{51}Zn_{20}$ (Mg_7Zn_3)

$Mg_{51}Zn_{20}$ (or conventionally known as Mg_7Zn_3) is the compound with the lowest Zn concentration, i.e., ~ 30 at.% Zn, among all the binary intermetallic compounds. It is stable within temperature range of 325 to 341 °C according to the experimental Mg-Zn phase diagram shown in **Fig. 3.1** [7]. The crystal structure of $Mg_{51}Zn_{20}$ (Immm, $a = 14.083$ Å, $b = 14.486$ Å and $c = 14.025$ Å) was first reported by Higashi et al. based on single-crystal X-ray diffraction (XRD) [31]. The structure can be described as an arrangement of icosahedral polyhedra, which is basically the same as those of Mackay icosahedron (MI)-type quasicrystal approximant [31,32]. This atomic structure is later confirmed by transmission electron microscopy (TEM)in binary Mg-Zn alloys by Gao et al. [33] and Nemec et al. [23].

$Mg_{21}Zn_{25}$ (MgZn)

$Mg_{21}Zn_{25}$ (or conventionally known as MgZn) is the compound with Zn concentration slightly larger than 50 at.%. Since a large fraction of $Mg_{21}Zn_{25}$ or MgZn is usually observed in this binary alloy after equilibration, this phase is usually denoted as the equilibrium β phase. The conventionally designated MgZn phase was originally suggested by Hume-Rothery et al.[23], and later different crystal structures was proposed for MgZn, including the hexagonal crystal structure by Tarschisch [34], the orthorhombic structure McKeehan et al. [35], the rhombohedral structure by Khan [36], a base-centered monoclinic structure by Gao et al. based on TEM [33]. A slightly different stoichiometry of $Mg_{12}Zn_{13}$ was also suggested for this phase by Clark et al. using XRD [23,37], but the structural information was not reported.

The stoichiometry of $Mg_{21}Zn_{25}$ is accepted in recent publications [23,35,38]. Its crystal structure ($R\bar{3}c$, $a = b = 25.7758$ Å, $c = 8.7624$ Å, $\alpha = \beta = 90°$ and $\gamma = 120°$) was first proposed by Cerny et al. based on XRD [35] and further confirmed by other TEM and high angle annular dark field scanning transmission electron microscopy (HAADF-STEM) investigations [23,38,39]. This complex crystal structure has C14 Laves-type hexagonal columns isolated by the Mg-rich transition region with an orientation relationship of $[11\bar{2}0]_{\mathrm{C14}} \parallel [1\bar{1}00]_{\mathrm{Mg_{21}Zn_{25}}}$ and $[10\bar{1}0]_{\mathrm{C14}} \parallel [11\bar{2}0]_{\mathrm{Mg_{21}Zn_{25}}}$, respectively [35,40]. Further observation shows that C14 Laves-type columns can overlap with each other due to the local enrichment of Zn, leading to nanometer-sized C14 domains within $Mg_{21}Zn_{25}$ phase [38].

Mg_4Zn_7 (Mg_2Zn_3)

Mg_4Zn_7 (or conventionally known as Mg_2Zn_3) is the compound with Zn concentration of 60~63.6 at.%. This phase is first suggested to have a composition of Mg_2Zn_3 with a triclinic structure by Gallot and Graf [3,41]. But this crystal structure has not been experimentally confirmed. Later, it is proposed that this phase has a stoichiometry of Mg_4Zn_7 with a base-centered monoclinic structure ($\mathrm{B/2m}$, $a = 25.96$ Å, $b = 14.28$ Å, $c = 5.24$ Å, $\gamma = 102.5°$) [42]. Using TEM, Gao and Nie confirmed this structure and reported the orientation relationship of $[001]_{\mathrm{Mg_4Zn_7}}\sim \parallel [0001]_{\alpha}$ and $(630)_{\mathrm{Mg_4Zn_7}}\sim \parallel (01\bar{1}0)_{\alpha}$ with Mg matrix [33].

The Mg_4Zn_7 phase resembles the Frank-Kasper phase (a common type of the topologically close packed phase) and is closely related to 2D icosahedral quasicrystal [43]. Viewed along [010] direction, the Mg_4Zn_7 phase is characterized by the $MgZn_2$ rhombic units and the Mg_6Zn_7 elongated hexagonal units. The $MgZn_2$ rhombic unit is the same with the building unit of C14 and

C15 $MgZn_2$ Laves phases. The Mg_6Zn_7 elongated hexagonal unit can be formed by one rectangle unit and two icosahedral chains outside the rectangle [44]. In other words, the Mg_4Zn_7 phase is a Frank-Kasper type decagonal 2D quasicrystal approximant with a relative small unit cell compared with most approximants [45]. Similar decagonal quasicrystal and approximants built by hexagonal and rhombic units are reported in Mg-Zn-RE system [46–48].

C14 and C15 Laves phase $MgZn_2$

There are two phases that have stoichiometry of $MgZn_2$, i.e., C14 and C15, and there is no controversy about their composition. The C14 $MgZn_2$ is stable up to 590 ℃ in Mg-Zn phase diagram in **Fig. 3.1** [7]. Its crystal structure was first discovered by Friauf in 1927 [49]. Later, Laves and his coworkers performed extensive research on C14 $MgZn_2$, which is thus named Laves phase [50–52]. The C14 $MgZn_2$ has a hexagonal structure ($\mathrm{P6_3/mmc}$, $a = 5.221$ Å, $c = 8.57$ Å) [53]. Viewed along $[2\bar{1}\bar{1}0]$ direction, it is identified as zigzag-stacked $MgZn_2$ rhombic units packed along [0001] direction. Recently, in the exploration of intermediate phases in Mg-Zn alloys, metastable $MgZn_2$ with C15 structure is also found [54,55]. C15 $MgZn_2$ has a face centered cubic structure ($\mathrm{Fd\bar{3}m}$, $a = b = c = 5.234$ Å) [56] built by the same rhombic units in C14 $MgZn_2$ but stacked in an aligned pattern along [001] direction [54,55]. Both C14 and C15 Laves $MgZn_2$ belong to the Frank-Kasper phases, which are structurally related to a large number of quasicrystals and their approximants [45,52]. Icosahedral clusters, i.e., the unit structure of quasicrystal, can be found within C14 and C15 Laves $MgZn_2$ [57,58]

Mg_2Zn_{11}

There is no controversy involving the stoichiometry of Mg_2Zn_{11} phase. The structure of Mg_2Zn_{11} (Pm$\overline{3}$, $a = b = c = 8.54$ Å) is first determined by Samson based on single-crystal XRD study [59]. This structure can be seen as a cubic packing of Pauling triacontahedra linked through Zn octahedral or as an embedding of icosahedra in an FCC matrix, which is structurally related with the simple C14 Laves $MgZn_2$ phase, the quasicrystals and approximants typically in ZnMgAl and Zn(Mg)Sc systems [60].

3.2.2 Precipitates

Precipitation sequence

The precipitation sequence in Mg-Zn alloys depends on the alloy composition and thermal history. Using early TEM, Clark reported that the precipitation sequence in Mg-5wt.%Zn alloy follows S.S.S.S. → MgZn' (rod-like coherent C14 Laves phase $MgZn_2$) → MgZn at the temperature of 149 °C and above [12]. Based on XRD analysis and electron microscopy, Mima et al. suggested that in Mg-4wt. %Zn alloy the precipitation sequence is S.S.S.S. → pre-β' → β' → β (MgZn) for temperature above 110 °C and S.S.S.S → GP zone → pre-β' → β' for temperature ranging from 60 to 110 °C [16]. In the early literatures, MgZn' and β' refers to the rod-like precipitates, corresponding to β_1' in recent publications, while pre-β' refers to the preliminary precipitates that were observed before β'. Based on Laue XRD, Takahashi et al. suggested that the precipitation sequence is S.S.S.S. → GP 1 zones → GP 2 zones → ${\beta_1}'$→ ${\beta_2}'$→ β [17]. Using TEM, Wei et al. reported the transition from rod-like β_1' to disc-like β_2' is the onset of over aging [18]. In recent publications, the commonly accepted precipitation sequence is S.S.S.S. → GP zones →

$\beta_1{}'$→ $\beta_2{}'$→ β [3,21]. The structures of GP zones, $\beta_1{}'$ and $\beta_2{}'$ are discussed in the following sections.

GP zones

The GP zones in Mg-Zn system are usually described as coherent nano-scale precipitates of a few atomic layers on certain crystalline planes of Mg matrix. In 1962, Murakami employed Laue XRD and showed the formation of GP zones that causes age hardening is on the $\{10\bar{1}0\}$ plane at the temperature range of 70-100 ℃ [61]. In 1969, Mima et al. suggested existence of GP zone from the difference in thermal behavior compared with pre-β' in Mg-4 wt.% Zn specimen during aging process, in spite of the lack of direct evidence from electron microscopy [16]. Using Laue XRD, Takahashi et al. discovered patterns for GP 1 and GP 2 zones, where GP 1 is plate-like on $\{11\bar{2}0\}$ plane formed below 60 ℃ and GP 2 oblate spheroid on basal plane that forms below 80 ℃ [17]. Komatsu et al. also suggested the existence of GP zones in Mg-4wt.%Zn alloy due the increase in electrical resistivity at temperatures up to 333 K (60℃) [19]. Direct observation of GP zones is challenging due to its small size and coherency with the matrix. With modern high resolution TEM, Buha observed Zn clusters and GP zones on $\{0001\}_\alpha$ and $\{2\bar{1}\bar{1}0\}_\alpha$ planes in Mg-2.8 at.% Zn alloys heat treated at 70-100 ℃ [21]. However, the experimental evidence is considered insufficient to support the existence of such Zn clusters and GP zones [3]. The increased hardness attributed to GP zones in this work are also unrealistically high compared with those reported by the others [3]. In Mg-2.4 at.% Zn alloys aged at 70 ℃ for 100 h, Bhattacharjee et al. reported the formation of GP zone from 3 dimensional atom probe (3D-APT) result, and suggested early stage GP zones serve as heterogeneous nuclei for the β_1' [62]. Zhou et al. reported observation of GP zones on $\{0001\}_\alpha$ and $\{2\bar{1}\bar{1}0\}_\alpha$ planes in TEM results in Mg-4 wt.% Zn alloys processed by high strain rate rolling, pre-aging at 70°C and aging at 160°C [5], although the detailed atomic structures are not reported. In the Mg-5.78Zn-0.44Zr wt.% alloy processed by integrated extrusion and equal channel angular pressing at 623K (350°C) and then aging at room temperature, GP zones on $\{10\bar{1}0\}_\alpha$ plane were reported in their HAADF STEM images [63]. It is accepted that Zr plays the role of grain refiner and does not change the atomic structures of binary Mg-Zn precipitates [64,65]. So far, many experimental studies suggested the existence of GP zones in Mg-Zn alloys, although direct imaging that can definitively resolve the issue is still lacking.

$\boldsymbol{\beta_1'}$ precipitates

The metastable precipitate that forms after GP zones is named β_1', which usually has a rod-like morphology perpendicular to the basal plane of Mg matrix and appear in the peak-aged samples. There has been controversy for the crystal structure of β_1' precipitates. In early literatures of precipitation in Mg-Zn alloys, β_1' precipitates, also described as MgZn' or β' [12,66], were determined from XRD and selected-area electron diffraction (SAED) to have the same structure with C14 Laves phase $MgZn_2$ with an orientation relationship of $[0001]_{\mathrm{C14}} \parallel [11\bar{2}0]_{\mathrm{Mg}}$ and $(11\bar{2}0)_{\mathrm{C14}} \parallel (0001)_{\mathrm{Mg}}$ with the Mg matrix [18,66]. Another hexagonal structure was also reported for β_1' [3,67], but it has not been confirmed so far.

In the electron microscopy study of precipitates in a Mg-8 wt.% Zn alloy aged at 200 °C, Gao et al. reported that, contrary to the traditional view of C14 Laves phase $MgZn_2$, β_1' rods have a base centered monoclinic structure ($a = 25.96$ Å, $b = 14.28$ Å, $c = 5.24$ Å, $\gamma = 102.5$ deg) that is similar to that of Mg_4Zn_7 with an orientation relationship of $[001]_{\mathrm{Mg_4Zn_7}}\sim \parallel [0001]_\alpha$ and

$(630)_{\mathrm{Mg_4Zn_7}}\sim \parallel (01\bar{1}0)_{\alpha}$ [20]. This result is confirmed by a separate TEM study from Singh et al. [68].

In the TEM study of binary Mg- 3 at.% Zn alloys aged at 150 °C, Rosalie et al. reported, rather than single-phase precipitates, β_1' rods contain a mixture of Mg_4Zn_7 and C14 $MgZn_2$ phases [55]. The orientation relationship between α-Mg matrix, Mg_4Zn_7 and C14 $MgZn_2$ follows $[0001]_{\mathrm{Mg}} \parallel [010]_{\mathrm{Mg_4Zn_7}} \parallel [0001]_{\mathrm{C14}}$ and $(11\bar{2}0)_{\mathrm{Mg}} \parallel (20\bar{1})_{\mathrm{Mg_4Zn_7}} \parallel (0\bar{1}10)_{\mathrm{C14}}$ [55]. Some domains of C15 $MgZn_2$ were also found inside the β_1' rods [54,55]. The two Laves phase structures have the orientation relationship: $[1\bar{1}00]_{\mathrm{C14}} \parallel [110]_{\mathrm{C15}}$ and $(0002)_{\mathrm{C14}} \parallel (1\bar{1}1)_{\mathrm{C15}}$ [54,55].

Based on HAADF-STEM study in Mg-2.2 at.% Zn alloy aged at 200 °C, Bendo et al. also confirmed that [25], in addition to C14 $MgZn_2$ and monoclinic Mg_4Zn_7, β_1' precipitates in binary Mg-Zn alloy show a variety of crystal structures, which can be interpreted as 2 dimensional arrangement of the Mg_6Zn_7 elongated hexagonal units and the $MgZn_2$ rhombic units in Penrose tiling viewed along $[2\bar{1}\bar{1}0]_{\mathrm{C14}}$ (or $[010]_{\mathrm{Mg_4Zn_7}}$) direction. The two structural units can be tiled to form a series of structures: the crystalline phases (i.e., C14 and C15 $MgZn_2$ Laves phase), complex 2D quasicrystals (without translational symmetry on the $(2\bar{1}\bar{1}0)_{\mathrm{C14}}$ plane) and their approximants (i.e., crystalline structures of Mg_4Zn_7 and similar structures). The orientation relationship between α-Mg matrix, domains of C14 $MgZn_2$ follows $[0001]_{\mathrm{Mg}} \parallel [2\bar{1}\bar{1}0]_{\mathrm{C14}}$ and $(11\bar{2}0)_{\mathrm{Mg}} \parallel (0001)_{\mathrm{C14}}$ [25].

Combining TEM with molecular dynamics simulations, Yang et al. explains that the prismatic dislocations in Mg-Zn system break the symmetry of HCP lattice and further introduce fivefold rings, which facilitate the formation of 2D quasi-crystalline precipitates along the dislocations. Although not explicitly mentioned, the morphology and orientation of the rod-like precipitates are consistent with those of β_1' [44].

$\boldsymbol{\beta_2'}$ precipitates

The metastable plate-like precipitates are generally identified as β_2' and form on the basal plane of Mg matrix [3,18,20,21]. Extensive formation of plate-like β_2' coincides with the onset of overaging [18]. The crystal structure of β_2' is confirmed to be C14 $MgZn_2$ with an orientation relationship of $(0001)_{\mathrm{C14}} \parallel (0001)_{\mathrm{Mg}}$ and $[11\bar{2}0]_{\mathrm{C14}} \parallel [10\bar{1}0]_{\mathrm{Mg}}$, as reported in the early literature [18]. A small fraction of the β_2' precipitates are also reported as laths with the long axis along $[0001]_{\mathrm{Mg}}$ and an orientation relationship with Mg matrix same as that of β_1', i.e., $[11\bar{2}0]_{\mathrm{C14}} \parallel [0001]_{\mathrm{Mg}}$ and $(0001)_{\mathrm{C14}} \parallel (11\bar{2}0)_{\mathrm{Mg}}$ [20]. It is suggsted that these β_2' laths can be distinguished from the β_1' rods by the larger aspect ratio of the cross section and the near parallelogram shape with the broad surface parallel to $[10\bar{1}0]_{\mathrm{Mg}}$ [3]. However, there is no quantitative criterion to differentiate the morphology of a rod from that of a lath. In some papers these laths are also denoted as β_1' [25]. Less commonly, other orientation relationships between β_2' laths and Mg matrix are also reported, e.g., $[11\bar{2}0]_{\mathrm{C14}} \parallel [0001]_{\mathrm{Mg}}, (1\bar{1}06)_{\mathrm{C14}} \parallel (\bar{1}010)_{\mathrm{Mg}}$ [18,20].

3.2.3 Current focus

With the advanced characterization techniques, especially HAADF-STEM and 3D-APT, the structures of intermetallic compounds and precipitates in alloys can be thoroughly investigated. However, there are on-going debates on the structures and stabilities of phases in Mg-Zn alloys, especially for the metastable precipitates. The focus of the current work is summarized as the following:

(1) GP zones have been reported in different experimental studies. However, the atomic structures and stabilities of this early-stage precipitates are unclear.

(2) β_1' precipitates include a hierarchy of structures built by the rhombic $MgZn_2$ and the hexagonal Mg_6Zn_7 units (e.g., C14 and C15 Laves phase $MgZn_2$, Mg_4Zn_7, quasicrystals and approximants). However, the relative stabilities of structures within this hierarchy are still unclear.

(3) β_2' precipitates with C14 $MgZn_2$ dominantly have two distinct orientation relationships with respect to α-Mg. The origins behind these two distinct orientation relationships of the same phase are unclear.

In the following sections, comprehensive first-principles calculations based on DFT [27,28], CE [29] and MC [30] are performed to fill the knowledge gaps.

3.3 Results

3.3.1 Phase structures and stability

To assess the phase stability in Mg-Zn binary system, we calculate the 0 K formation energy for the reported compounds with the atomic structures from Inorganic Crystal Structure

Database [71]. The symmetry, lattice parameter, and formation energy of the reported phases collected from previous experiments, the DFT results from Materials Project (MP) [56] and Open Quantum Mechanical Database (OQMD) [72], together with current calculations are shown in Table 1.

The global convex hull constructed on the current calculations are shown as the black line in **Fig. 3.2**. The predicted stable phases include Mg21Zn25, C14 MgZn2 and Mg2Zn11. Careful examination shows that, Mg4Zn7 is 1.2 meV/atom above the convex hull, which is close to the error bar of DFT energy. If such small energy difference is ignored, Mg21Zn25, Mg4Zn7 and C14

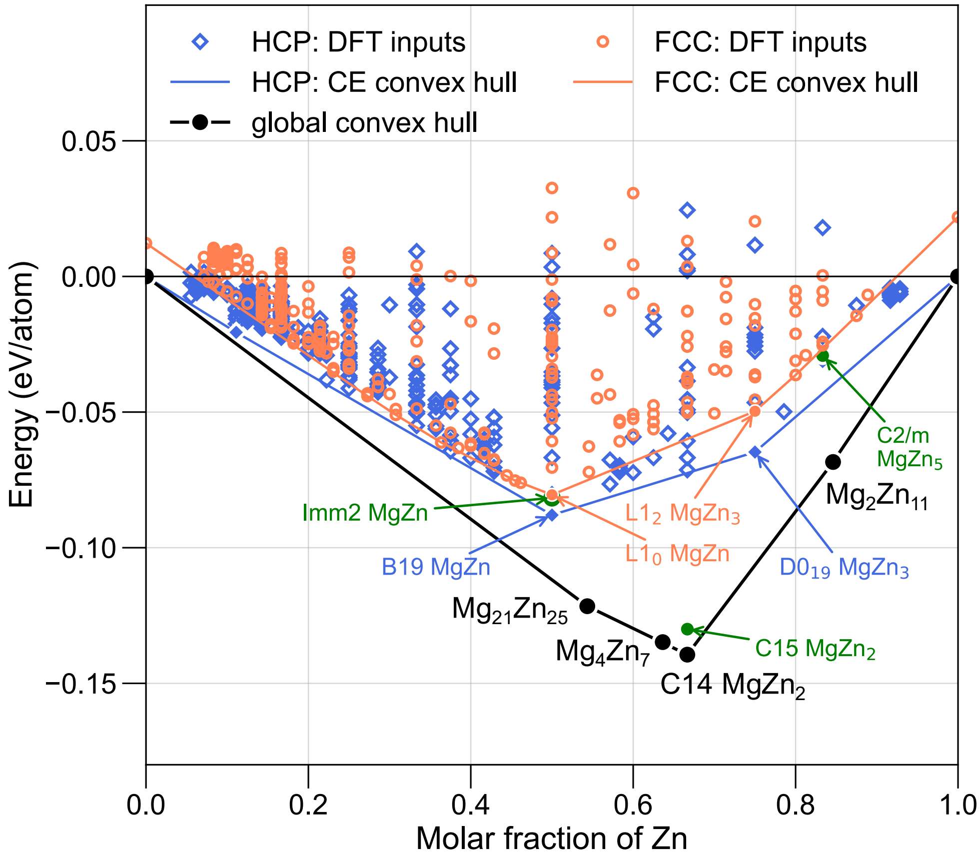

Fig. 3.2 Formation energies of the experimental observed compounds in Mg-Zn alloy and orderings on FCC and HCP lattice searched by CE. Formation energies are calculated relative to the energy of Mg and Zn on HCP lattice at 0 K. Blue diamonds, orange open circles, green filled circles and black filled circles indicate HCP orderings, FCC orderings, metastable incoherent compounds and stable compounds, respectively.

MgZn2 lie on the convex hull and are stable structures in Mg-Zn system. This is in agreement from the phase diagrams evaluated experimentally [7,73,74]. According to the criterion by Ravi et al. [75,76], the precipitation process during aging follows the sequential decrease of the energy per solute atom of the precipitates, which can be determined by the slope of the line connecting the precipitate to pure solvent on formation energy (ΔE_f) vs. composition diagram; see **Fig. 3.2**. From the current calculations, the slopes for C14 MgZn2, Mg4Zn7 and Mg21Zn25 are determined as -

0.2091, -0.2118 and -0.2237 (eV/atom), thus leading to the stability sequence of C14 MgZn2 → Mg4Zn7 → Mg21Zn25. Note that the slopes for C14 MgZn2 and Mg4Zn7 are actually very close to each other (with a difference of ~ 3 meV/atom), with Mg21Zn25 slightly more stable than C14 MgZn2 and Mg4Zn7. Therefore, from a thermodynamic point of view, the current calculations explains the coexistence of C14 MgZn2 and Mg4Zn7 in β_1' rods [25,54,55], which eventually transforms to the equilibrium β phase (i.e. Mg21Zn25).

Table 3.1. The structural information and formation enthalpies of the compounds and precipitates in Mg-Zn alloys. The first-principles data from Materials Project (MP) [56] and Open Quantum Materials Database (OQMD) [72] are listed together with published experimental and first-principles results.

Phase	**Structural information**	**Lattice parameter**					**Formation enthalpy**		
		Method	***a*** **/Å**	***b*** **/Å**	***c*** **/Å**	**Reference**	**Method**	**Values / kJ/mol-atom**	**Reference**
GP zone	Not reported	Calorimetry				[16]			
	Not reported	Electrical resistivity				[19]			
	Not reported	3D-APT				[62]			
	Oblate spheroid on $\{0001\}_{\mathrm{Mg}}$ plane	Laue XRD				[17]			
	Plates on $\{2\bar{1}\bar{1}0\}_{\mathrm{Mg}}$ plane	Laue XRD				[17]			
		TEM				[21]			
						[5]			
	Plates on $\{01\bar{1}0\}_{\mathrm{Mg}}$ plane	Laue XRD				[61]			
		TEM				[63]			
	Plates on $\{0001\}_{\mathrm{Mg}}$ plane	TEM				[21]			
						[5]			
	Orthorhombic, Immm	XRD	14.083	14.486	14.025	[31]	CALPHAD	-4.8, 298K	[77]
		TEM	14.083	14.486	14.025	[33]	DFT	-5.89, 0K	[78]

$Mg_{51}Zn_{20}$ (Mg_7Zn_3)		TEM	14.08	14.49	14.03	[23]	CALPHAD	-5.3, 298K	[73]
$Mg_{21}Zn_{25}$ (MgZn)	Hexagonal, P63/mmc	XRD	10.66		17.16	[34]	Direct calorimetry	-10.5±3.1, 298K	[79]
		DFT	10.734		17.588	[56]	DFT	-7.14, 0K	[56]
	Orthorhombic, Imm2		5.33	17.16	9.23	[80]	Calorimetry-tin solution	-8.9±0.4, 298K	[81]
		DFT	10.626	17.591	9.177	[72]	DFT	-7.72, 0K	[72]
	Rhombohedral	XRD	25.69	-	18.10	[36]	Calorimetry-acid solution	-12.14±3, 298K	[82]
	C1c1 or C1 2/c1	TEM	16.10	25.79	8.80	[33]	CALPHAD	-9.6, 298K	[77]
							Partial drop-solution	−7.9 ± 3.1, 298K	[83]
							CALPHAD	-10.4, 298K	[73]
	Trigonal, $R\bar{3}c$	XRD	25.78	-	8.76	[35]			
		TEM	25.518	-	8.713	[39]	DFT	-12.42, 0K	[78]
		DFT	15.042	15.042	15.042	[56]	DFT	-6.95, 0K	[56]
		DFT	25.4	-	8.6	[72]	DFT	-11.67, 0K	[72]
		DFT	25.78	-	8.76		DFT	-12.06, 0K	[26]

						Current work	DFT	-11.72, 0K	Current work
Mg_4Zn_7 (Mg_2Zn_3)			17.24	14.45	5.20	[41]	Calorimetry-acid solution	-13.96±3, 298K	[82]
	Monoclinic, C2/m	XRD	25.96	14.28	5.24	[42]	CALPHAD	-11.0, 298K	[77]
		TEM	25.96	14.28	5.24	[33]	CALPHAD	-10.9, 298K	[73]
		TEM	26.69	14.11	5.11	[39]	DFT	-13.22, 0K	[26]
		DFT	26.304	14.141	5.287	[56]	DFT	-13.32, 0K	[56]
		DFT	25.8	14.1	5.2	[72]	DFT	-12.93, 0K	[72]
		DFT	26.484	14.185	5.190	Current work	DFT	-13.02, 0K	Current work
C14 $MgZn_2$	Hexagonal, P63/mmc	XRD	5.15		8.48	[49]	Calorimetry-acid solution	-17.6, 291K	[84]
		XRD	5.221		8.567	[85]	Direct calorimetry	-15.1±1.1, 298K	[79]
		DFT	5.251		8.445	[56]	Partial drop-solution	-7.9 ± 3.1, 298K	[83]

		DFT	5.188		8.495	[72]	Calorimetry-tin solution	-10.9 ± 0.4, 298K	[81]
							Calorimetry-acid solution	-13.8 ± 3, 298K	[82]
							CALPHAD	-11.7, 298K	[77]
							DFT	-13.85, 0K	[78]
							DFT	-12.64, 0K	[56]
							DFT	-13.32, 0K	[72]
							DFT	-13.60, 0K	[26]
		DFT	5.221		8.503	Current work	DFT	-13.41, 0K	Current work
C15 $MgZn_2$	Cubic, $Fd\bar{3}m$	TEM				[54]			
		TEM				[55]			
		DFT	5.21	5.21	5.21	[26]	DFT	-12.64, 0K	[26]
		DFT	5.234	5.234	5.234	[56]	DFT	-12.93, 0K	[56]
		DFT	5.219	5.219	5.219	Current work	DFT	-12.58, 0K	Current work
Mg_2Zn_{11}	Cubic,		8.552	8.552	8.552	[59]	Direct calorimetry	-10.0 ± 2.5, 298K	[79]

	$Pm\bar{3}$	TEM	8.415~8.462	8.415~8.462	8.415~8.462	[39]	CALPHAD	-5.8, 298K	[77]
		DFT	8.551	8.551	8.551	[56]	DFT	-6.56, 0K	[56]
		DFT	8.496	8.496	8.496	[72]	DFT	-6.46, 0K	[72]
		DFT	8.519	8.519	8.519	Current work	DFT	-6.56, 0K	Current work
							CALPHAD	-9.9, 298K	[73]
							Calorimetry-acid solution	-8.96 ± 3, 298K	[82]
							DFT	-7.11, 0K	[78]
							DFT	-6.66, 0K	[26]

Most early-stage precipitates usually form coherently with the matrix due to the strong constraint from the parent lattice. Therefore, the metastable convex hulls on HCP Mg matrix in Mg-Zn system are calculated with the low energy structures searched by CE. The FCC metastable convex hull is also calculated, considering the formation of FCC phase in some HCP Mg alloys [70]. The symmetrically distinct orderings on both lattices are enumerated for up to 18 atoms to search for the ground states of coherent orderings. The distortion of the structures during structural relaxation are calculated according to the criterion of ATAT [69,81], and these relax away from the parent lattice (i.e., over 10% lattice distortion) are excluded for the CE fitting. All the energies of those orderings within the relaxation range after DFT calculation are shown in **Fig. 3.2** (orange circles for FCC and blue diamonds for HCP). The corresponding convex hulls are built, with the ground state being B19 MgZn and $\mathrm{D0_{19}}$ MgZn3 for HCP lattice, and $\mathrm{L1_0}$ MgZn and $\mathrm{L1_2}$ MgZn3 for FCC lattice. The FCC convex hull is higher than that of HCP across all concentration range, which means the orderings on HCP lattice are more stable. However, both convex hulls are well above the global convex hull, making the HCP and FCC ordering phases less stable than ground sates on the global convex hull and thus more difficult to be massively observed in experiments.

3.3.2 Atomic structures of GP zones

As listed in Table 1, there have been experimentally reported plate-like GP zones on $\{0001\}_{\mathrm{Mg}}$ planes [5,21], $\{2\bar{1}\bar{1}0\}_{\mathrm{Mg}}$ planes [5,17,21], $\{01\bar{1}0\}_{\mathrm{Mg}}$ planes [61,63] and ones without structural information [62] in Mg-Zn alloys. However, these GP zones were rarely clearly characterized in experiments. Therefore, we leveraged DFT combined with CE to predict their potential atomic structures. Here the coherent orderings showing Zn-rich plates (GP sheets) on the reported planes of the Mg matrix are considered to contain the potential GP zones. In addition, those containing low-energy rods (GP rods) and bulk structures are also considered since they are reported to be structurally related to the GP sheets in other Mg alloys [86]. To search the potential GP zones, all the low-energy coherent structures that are within ~ 10 meV/atom above the HCP convex hull with the overall Zn composition less than 50% are examined. The criterion of ~ 10 meV/atom is chosen considering the error bars involved in the methods of DFT and CE. Previously the GP zones within this energy range were reported to be observed in experiments [86]. Using this criterion, two bulk structures are found, i.e., $D0_{19}$ Mg_3Zn and B19 MgZn with the former being 2.7 meV/atom above and the latter on the HCP convex hull, and their detailed atomic structures are shown in **Fig. 3.3(a) and (b)**, respectively.

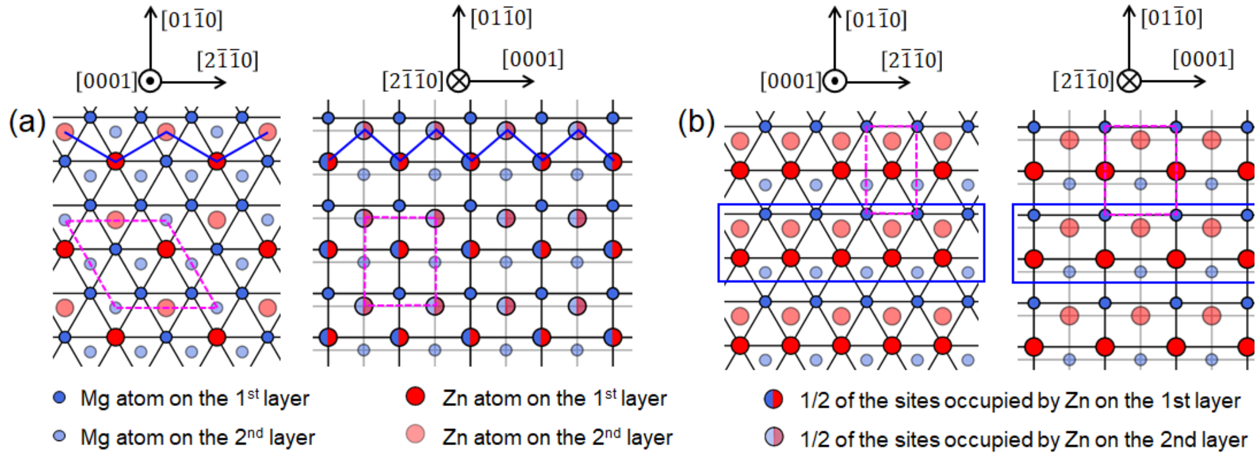

Fig. 3.3 Schematic crystal structures of (a) D019 Mg3Zn (2.7 meV/atom above HCP convex hull) and (b) B19 MgZn (on HCP convex hull). The Mg and Zn atoms are represented by blue and red circles, respectively, with the second layers along the [0001] and $[2\bar{1}\bar{1}0]$ directions partially transparent to distinguish from the first layer. The dashed purple line indicates the primitive cell. The circles partially in red indicates the fraction of Zn occupancy along the viewing direction. The blue lines indicate the "building block" of the ordering structures.

As shown in **Fig. 3.4**, the formation energies of structures containing the same type of GP zone are marked with the same symbol (belong to the same family). The difference of structures in a family comes from different relative positions between neighboring GP zones in the Mg matrix. The atomic structures of different GP zones are plot schematically with Mg matrix hidden for convenience. The GP rods are predicted to consist of single and double Zn atomic rows are along $[2\bar{1}\bar{1}0]_{\mathrm{Mg}}$ direction (cyan and brown boxes) with their formation energies marked by cyan 'Y' and brown '⅄' symbols, respectively. The GP sheets on $\{0001\}_{\mathrm{Mg}}$ plane are predicted to have single or triple Zn-rich layers with the Zn concentration of 50 at.% within the Zn-rich layer (green box in the $[2\bar{1}\bar{1}0]_{\mathrm{Mg}}$ direction), and their formation energies are marked by green hexagons. The GP sheet on the $\{2\bar{1}\bar{1}0\}_{\mathrm{Mg}}$ plane is predicted to be a monolayer structure with 50 at.% Zn within this layer (blue box in the $[0001]_{\mathrm{Mg}}$ direction), and its formation energy is marked by blue square. The GP sheets on the $\{01\bar{1}0\}_{\mathrm{Mg}}$plane are predicted to have zigzagged Zn atoms (purple box) and double-layered Zn atoms (red box) viewed along $[0001]_{\alpha}$ direction, and their formation energies are marked by purple and red squares, respectively.

The relative stabilities of the predict structures can be analyzed by the vertical distances of their formation energies to the HCP convex hull. Those with smaller distances are more thermodynamically stable. As shown in **Fig. 3.4**, the structure containing the GP sheet on the $\{2\bar{1}\bar{1}0\}_{\mathrm{Mg}}$ plane has a distance to the convex hull of 10.2 meV/atom. The most stable structure containing the GP sheet on the $\{0001\}_{\mathrm{Mg}}$ plane (the monolayer one) has a distance of 6.6 meV/atom. For GP sheets on the $\{01\bar{1}0\}_{\mathrm{Mg}}$ plane, there are two different types, i.e., the zigzagged ones in the $D0_{19}$ family and the double-layered ones in the B19 family. The most stable structure in the B19 family resides on the HCP convex hull, while the most stable one in the $D0_{19}$ family

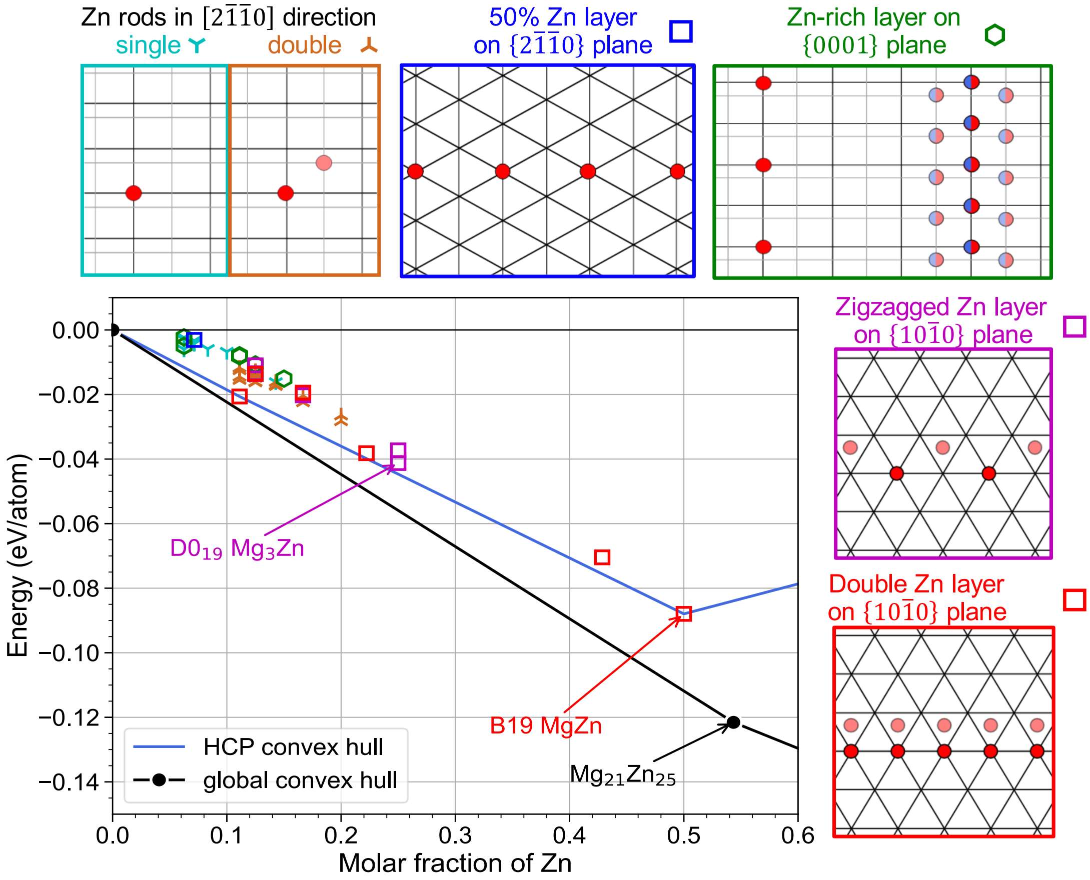

Fig. 3.4 The ground state formation energies of the predicted GP zones and their schematic crystal structures. In the schematics for structures, the sites that are fully and partially occupied by Zn are indicated using red and red/blue circles, respectively.

has a distance of 7.4 meV/atom. Therefore, although it is possible for these structures to be observed in experiments, the one containing the double-layered GP sheet on the $\{01\bar{1}0\}_{\mathrm{Mg}}$ plane is the most thermodynamically favored, followed by the one with the monolayer GP sheet on the $\{0001\}_{\mathrm{Mg}}$ plane, the one with the zigzagged GP sheet on the $\{01\bar{1}0\}_{\mathrm{Mg}}$ plane, and finally the one with the GP sheet on the $\{2\bar{1}\bar{1}0\}_{\mathrm{Mg}}$ plane. Noted, the structures in **Fig. 3.4** are calculated using small DFT cells, where the constraint from the large Mg matrix on GP zones not fully considered.

Further analysis on the effect of this constraint from the Mg matrix on the stabilities of GP zones is detailed in section 4.4.

Further examination shows that GP zones on the $\{01\bar{1}0\}_{\mathrm{Mg}}$ plane are structurally related to the two bulk structures, i.e., D0$_{19}$ Mg$_3$Zn and B19 MgZn. The zigzagged GP sheets on the $\{01\bar{1}0\}_{\mathrm{Mg}}$ plane are the substructures of the D0$_{19}$ Mg$_3$Zn bulk structure, as indicated by blue lines in **Fig. 3.3(a)** of the bulk D0$_{19}$ Mg$_3$Zn and **Fig. 3.5(a)** of a zigzagged Zn GP sheets. Similarly, the double-layered GP sheets on the $\{01\bar{1}0\}_{\mathrm{Mg}}$ plane are substructures of the B19 MgZn bulk structure, as indicated by the blue box in **Fig. 3.3(b)** of the bulk B19 MgZn and **Fig. 3.5(b)** of a double layered Zn GP sheets. Overall, the GP sheets on the $\{01\bar{1}0\}_{\mathrm{Mg}}$ plane can be regarded as the mixtures of pure Mg and the building blocks of the predicted bulk structures, and the ratio of the two mixing "components" can change with the overall Zn concentration in the Mg matrix.

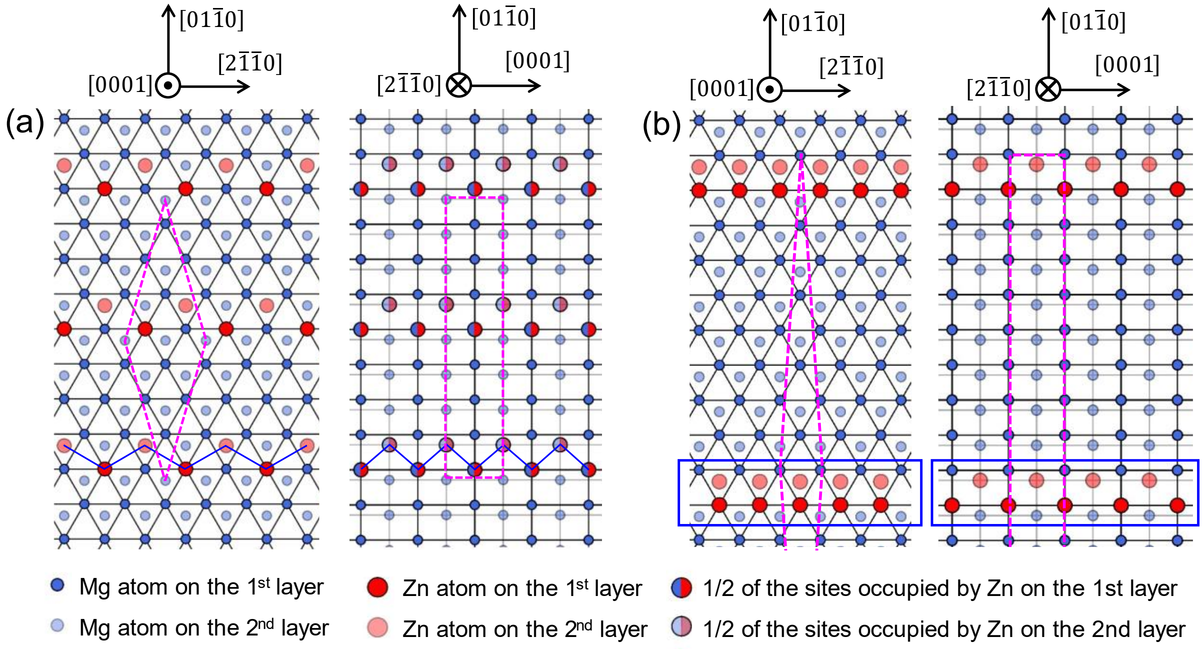

Fig. 3.5 Schematic crystal structures of potential GP sheets on $\{01\bar{1}0\}$ prismatic plane with energy close to convex hull (5meV/atom): (a) GP sheet resembling D019 Mg3Zn; (b) GP sheet resembling B19 MgZn.

3.3.3 Finite temperature stability of GP zones

At finite temperatures, the disordering of site occupation will lead to configurational entropy that affects the stability of GP zones. Here the equilibrium between Mg solid solution and potential GP sheets are examined by the SGCMC simulation and compared with experiments. To demonstrate how the phase boundaries are calculated, the free energies of Mg solid solution and potential GP sheets on $\{01\bar{1}0\}_{\mathrm{Mg}}$ plane with zigzagged Zn (**Fig. 3.5(a)**), as well as the common tangent for phase equilibrium are shown in **Fig. 3.6(a)**. The SGCMC simulation without further constraints yields the free energies for single phase regions, but not the metastable or unstable regions [70]. Therefore, in the current MC of GP zones, the atomic arrangements are constrained to the structural template to sample the configurational states related to the corresponding GP zones above the HCP convex hull, which are in metastable states. For example, the free energy curve of the zigzagged GP zone in $D0_{19}$ family is calculated using Monte Carlo by only allowing the Zn atoms in the GP zone to be switched to Mg, while the switching from Mg to Zn is prohibited. In this way, the Zn atoms in the intermediate structures are either isolated in Mg matrix or form part of the zigzagged pattern on $\{01\bar{1}0\}_{\mathrm{Mg}}$ plane, which is exactly the case for the equilibrium between the zigzagged GP zone and Mg-rich solid solutions.

Using this method, the phase boundaries (i.e., GP zone solvus) between Mg solid solutions and predicted structures containing GP sheets on $\{01\bar{1}0\}_{\mathrm{Mg}}$, $\{2\bar{1}\bar{1}0\}_{\mathrm{Mg}}$ and $\{0001\}_{\mathrm{Mg}}$ planes are calculated and compared with the alloy composition vs. temperatures of experimentally reported GP zones. The GP zone solvus is the boundary between single phase region of the Mg-rich solid solution and dual-phase region of the Mg-rich solid solution and the GP zone, with the upper-left side of the curve being Mg-rich solid solution and the lower-right side being the mixture of Mg-rich solid solution and GP zone. Noted, the listed experimental data points are the alloy composition vs. the temperature at which the GP zones were observed, not the experimentally measured phase boundary. Therefore, as long as the experimental data points for a specific GP zone fall into the lower-right side of the solvus, the calculation agrees with the experiments.

As shown in **Fig. 3.6(b)**, the calculated solvi for GP zones on $\{01\bar{1}0\}_{\mathrm{Mg}}$ and $\{0001\}_{\mathrm{Mg}}$ planes are above the corresponding experimental conditions, while the solvus for GP zones on $\{2\bar{1}\bar{1}0\}_{\mathrm{Mg}}$ plane is below some of the experimental conditions. For GP zones on $\{01\bar{1}0\}_{\mathrm{Mg}}$ plane, the phase boundary calculations show that GP sheets with double-layered Zn (the B19 family) is more stable than the zigzagged GP sheets. However, the double-layered GP sheet is predicted to transit to disordered solid solutions at very high temperatures (e.g., ~ 750 K for Mg-1 at.% Zn alloy), which are unrealistically stable as compared with experiments [17,63]. This indicate that the stability of the double-layered GP sheet is overestimated. The origin to this discrepancy is attributed to the lack of the constraint from Mg matrix to the GP sheets in the small structures in the training set of CE; see Section 4.4 for detailed discussion. In comparison, the calculated solvi for zigzagged GP zone on $\{01\bar{1}0\}_{\mathrm{Mg}}$ plane (blue line in **Fig. 3.6(b)**) and single layer GP zone on $\{0001\}_{\mathrm{Mg}}$ plane (green line in **Fig. 3.6(b)**) are slightly above the corresponding experimental conditions, which indicates agreement between calculations and experiments. For the GP zone on $\{2\bar{1}\bar{1}0\}_{\mathrm{Mg}}$ plane, the calculated solvus (brown line in **Fig. 3.6(b)**) breaks down due to the appearance of other ordering structures in MC simulations. Comparison with the corresponding experimental data indicates that the stability of GP zone on $\{2\bar{1}\bar{1}0\}_{\mathrm{Mg}}$ plane is underestimated.

The discrepancies between the calculated solvi and experiments can be attributed to the inaccuracies and uncertainties involved in calculations and experiments. In the DFT and CE calculations, the typical error bars of energy are approximately 1 and 5 meV/atom, respectively, which is insufficient to exactly reproduce experimental phase boundary. Additionally, the neglected effects (e.g., free energy due to lattice vibrations) in DFT can also contribute to the error in the estimation of the GP zone solvus. Experimentally, the detailed atomic structures of GP zones are not reported and the difference between the predicted atomic structures and the ones in experiments will contribute to the discrepancy. Lastly, some experimental characterization of GP zones in Mg-Zn alloys are considered insufficient [3,21], indicating uncertainties in previous experiments. Nonetheless, with configurational thermodynamics from only short-ranged interactions in CE, the calculations for zigzagged GP zone on $\{01\bar{1}0\}_{\mathrm{Mg}}$ plane and single layer GP zone on $\{0001\}_{\mathrm{Mg}}$plane shows agreement with experiments, indicating the importance of solute ordering during the formation of GP zones.

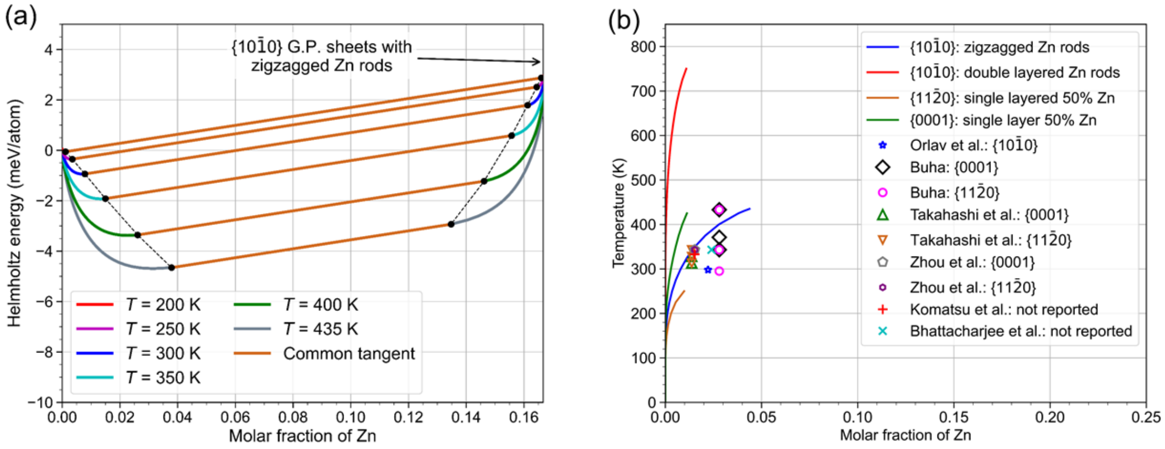

Fig. 3.6 The stability of the predicted GP zones at finite temperatures from Monte Carlo calculations and experiments: (a) Free energies and common tangents for the equilibrium between Mg solid solution and GP sheets on $\{01\bar{1}0\}$ plane; (b) The calculated phase boundaries (solid lines) between Mg solid solution and GP zones, compared with the aging temperatures and alloy compositions where various GP zones were observed (symbols).

3.3.4 Effects of the coherency strain on the stabilities of GP zones

Comparison between experiments and the analysis at finite temperatures indicate that the stability of the double-layered GP sheet on the $\{01\bar{1}0\}_{\mathrm{Mg}}$ plane is overestimated, i.e., unrealistically high transition temperature of its solvus. However, this stability analysis are based on energies from CE, where relatively small DFT cells (≤20 atoms) are used in the training set. As such, the number of atoms in the Mg matrix is limited; see the DFT cells marked by dashed purple lines in **Fig. 3.5**. This means the constraint from the Mg matrix on the GP zones can be incorrectly estimated compared with that in experiments. In our previous tests, the constraint from Mg matrix can slightly alter the relative stabilities between different GP zones calculated in small DFT cells [87]. Since this constraint comes from the coherency strain between GP zones and the matrix due to the lattice mismatch, Zn-concentration dependent CSE are adopted to analyze the effect of coherency strain on stabilities of GP zones. Here CSE were calculated on $\{0001\}_{\mathrm{Mg}}$,

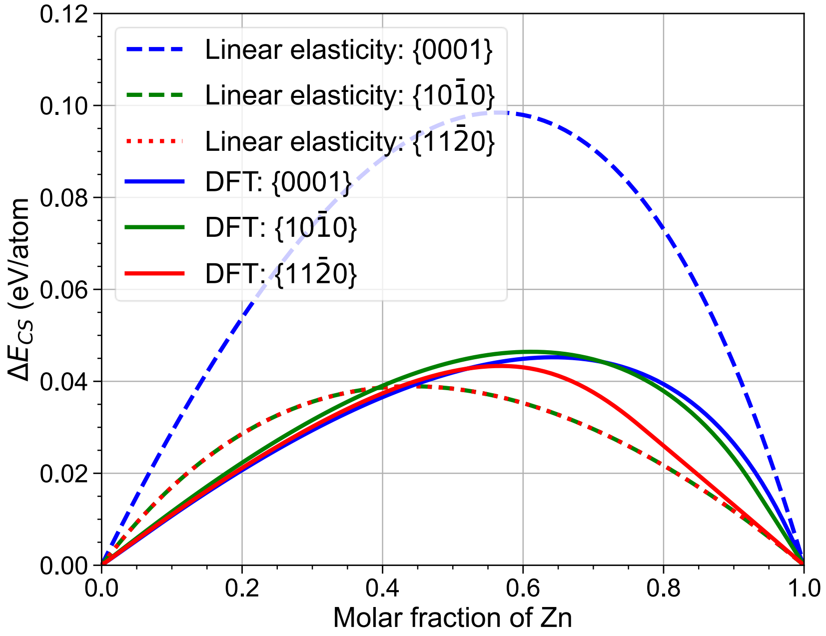

Fig. 3.7 The coherency strain energy of HCP Mg-Zn alloys as a function of Zn concentration on basal and prismatic planes calculated by DFT and linear elasticity theory

$\{2\bar{1}\bar{1}0\}_{\mathrm{Mg}}$, and $\{01\bar{1}0\}_{\mathrm{Mg}}$ planes, on which plate-like GP zones were experimentally reported to reside.

The CSE calculated from linear elasticity theory based on Eq. (3) are shown as dashed lines in **Fig. 3.7**. The CSE on the basal plane is significantly larger than those on the prismatic planes. This can be expected from the much larger mismatch along the *a* than the *c* axis between HCP Mg and HCP Zn, i.e., $\delta_a = 16.6\%$ and $\delta_c = 4.5\%$ based on the lattice mismatch defined by $\delta_a = \left(a_{\mathrm{Zn}} - a_{\mathrm{Mg}}\right)/a_{\mathrm{Mg}}$ [88]. However, the linear elasticity approach cannot consider the anharmonic lattice response, which is expected for Mg-Zn system, especially for the large lattice mismatch on the basal plane. Conversely, the anharmonic effects are incorporated in CSE calculated from DFT as shown by the solid lines in **Fig. 3.7**, which reveals a similar CSE on the basal and the two prismatic planes. Therefore, the large lattice mismatch on the basal plane is beyond the validity of linear elasticity and the CSE on this plane is overestimated consequently. Similar overestimation of the strain energy from linear elasticity was also reported for Cu [89].

At the Mg-rich side, the close CSE from DFT on the three planes means absence of a single epitaxially soft plane, and the three planes are almost equally favored in terms of coherency strain. This agrees with the fact that GP sheets on these planes are experimentally reported (Table 1), as opposed to the case of Al-Cu alloys, where GP zones are only observed on (001) plane [90].

As shown in **Fig. 3.7**, the CSE is proportional to the Zn concentration at the Mg-rich side. This means the CSE penalties increase for GP zones of higher Zn concentrations in a large Mg matrix. To focus on the role of the Zn concentration, the analysis is performed for the two types of GP zones both residing on the $\{01\bar{1}0\}_{\mathrm{Mg}}$ plane, i.e., the double-layered one in the B19 family and the zigzagged one in the $D0_{19}$ family, so that the effect on CSE due to crystallographic orientations is excluded. The double-layered GP sheet in the B19 family has 100 at. % Zn within the sheet, while the zigzagged one in the $D0_{19}$ family has 50 at. % Zn within the sheet. Thus, the CSE penalty on the double-layered GP sheet is larger than that on the zigzagged GP sheet when they are in large Mg matrixes of the same size. Consequently, the double-layered GP sheets will be destabilized by CSE compared with the zigzagged one.

To confirm the trend of increased CSE with larger Zn concentration, a double-layered GP sheet in the B19 family and a zigzagged GP sheet in the $D0_{19}$ family are embedded in DFT supercells with the same large Mg matrixes. The Mg matrix consists of 42 layers of Mg along $[10\bar{1}0]_{\mathrm{Mg}}$, which was tested to be sufficiently large to eliminate the interaction between GP sheets due to the periodic boundary conditions, as shown in **Fig. 3.8**. After DFT relaxation, the solutes in GP sheets do not move due to the symmetry of DFT cells, while the Mg atoms move towards the GP sheets due to the coherency strain. In comparison, the Mg atoms around the double-layered GP sheet in B19 family show much larger displacements than those around the zigzagged GP sheet in $D0_{19}$ family, which indicates a larger CSE penalty for the double-layered GP sheet.

The destabilization of the double-layered GP sheet in B19 family is confirmed by directly comparing the formation energies of the two supercells, where the constraint from the large Mg matrix on GP zones is better realized than the previous small cells in **Fig. 3.5**. The distance of the formation energy of the zigzagged GP sheet to the HCP convex hull is 2.2 meV/atom, while that of the double-layered GP sheet is 4.5 meV/atom. Therefore, with the constraint from Mg matrix, the zigzagged GP zone will be slightly favored than double-layered GP zone. Considering that this energy difference is close to the error bar of the DFT energy, both GP zones are likely to be observed in experiments. This is consistent with the observation of GP sheets on $\{01\bar{1}0\}_{\mathrm{Mg}}$ plane in Mg-5.78Zn-0.44Zr wt.% alloy[63], as shown in **Fig. 3.9**. Careful examination of the HAADF-STEM image shows that the zigzagged GP zones (yellow arrows in **Fig. 3.9**) can be observed.

Besides the zigzagged GP zones, there are also GP zones with the same thickness of zigzagged ones, but denser Zn and clearly a different pattern from the zigzag, as marked by the orange arrow

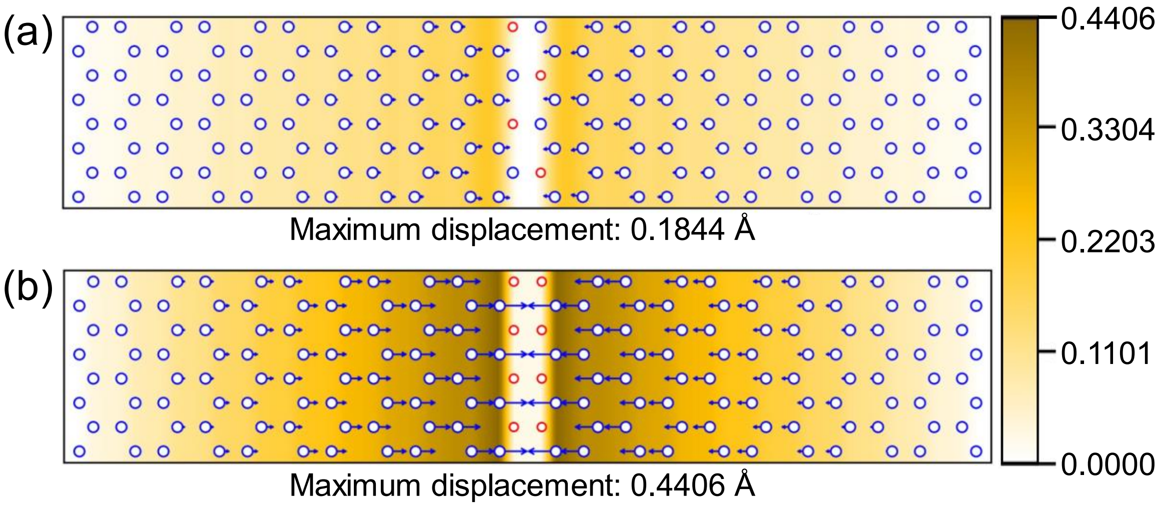

Fig. 3.8 The large supercell containing **(a)** a GP sheet that resembles D019 Mg3Zn phase, **(b)** a GP sheet that resembles B19 MgZn phase. The displacements of Mg atoms after relaxation in DFT are marked with arrows, which indicates a larger CSE with GP zones resembling B19 MgZn.

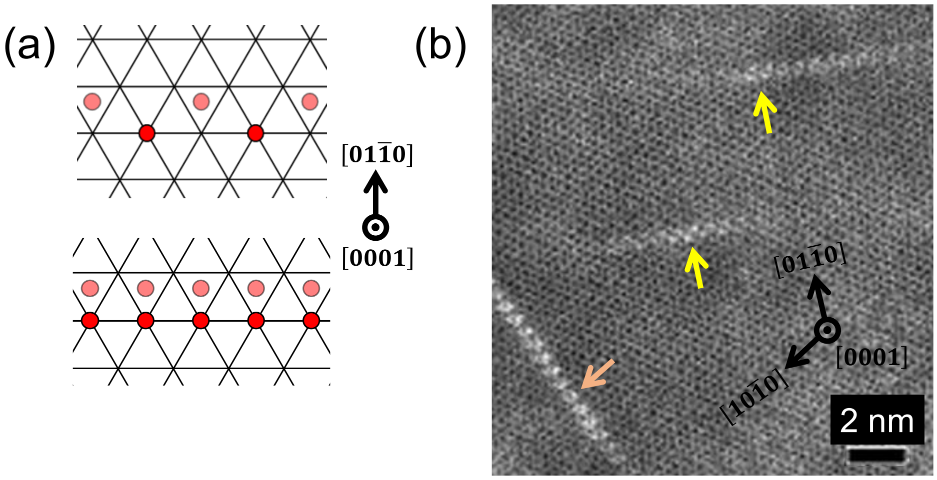

Fig. 3.9 **(a)** The predicted GP sheet on $(01\bar{1}0)_\alpha$ plane, and **(b)** experimentally observed nanoscale prismatic GP sheets on $\{01\bar{1}0\}$ plane of Mg matrix in Mg-5.78Zn-0.44Zr wt.% (Mg-2.23Zn-0.12Zr at. %) alloys [63], where Zr works as the grain refiner [64,65]. Note that zigzagged pattern of Zn can be vaguely observed. **Fig. (b)** is adapted from [63].

in **Fig. 3.9**. This GP zone likely belongs to the B19 family.

3.3.5 Structure and stability of β_1' precipitates

β_1' precipitates have rod-like morphology along $[0001]_{\mathrm{Mg}}$ direction and are formed in the peak-aged binary Mg-Zn alloys [18,20,62]. Recent TEM and HADEF-STEM observations [25,44,55] show that the crystal structure of β_1' is complex. Specifically, on the cross sections of the rods as shown in **Fig. 3.10(a)**, various arrangements of the $MgZn_2$ rhombic units and the Mg_6Zn_7 elongated hexagonal units on $(2\bar{1}\bar{1}0)_{\mathrm{C14}}$ plane lead to precipitates that are totally or partially composited by C14 $MgZn_2$, C15 $MgZn_2$, Mg_4Zn_7, 2D quasicrystals and approximants. To study the stability of β_1', the stabilities of this hierarchy of structures built by the $MgZn_2$ rhombic units and the Mg_6Zn_7 elongated hexagonal units are needed to be analyzed.

To probe the huge structural and compositional space of these complex crystalline structures, we built two structures, i.e., $Mg_{32}Zn_{59}$ and Mg_8Zn_{11}, using the two basic units and analyze them together with other decagonal quasicrystal approximants, i.e., Mg_4Zn_7, $Mg_{29}Zn_{48}$, $Mg_{22}Zn_{34}$, $Mg_{28}Zn_{41}$ from the Alloy Database by Mihalkovic et al. [78]. The structural files of these phases can be found in Supplementary Materials. Here only three phases, i.e., Mg_4Zn_7, Mg_8Zn_{11} and $Mg_{22}Zn_{34}$ are selected as examples to illustrate the detailed atomic structures, as shown in **Figs. 3.10(b)-(d)**, respectively. Viewed along $[010]_{\mathrm{Mg4Zn7}}$ (or $[2\bar{1}\bar{1}0]_{\mathrm{C14}}$) direction, their primitive cells are indicated in dashed purple line, the two basic units in dashed black lines and structural features of C14 and C15 from the rhombic units in blue and green solid lines, respectively. Mg_4Zn_7 in **Fig. 3.10(b)** has the elongated Mg_6Zn_7 hexagonal units at the four corners of the quadrilateral primitive cell, the $MgZn_2$ rhombic units forming C14 at a pair of opposite sides of the quadrilateral and C15 within the quadrilateral. Similarly, Mg_8Zn_{11} in **Fig. 3.10(c)** have the Mg_6Zn_7 elongated hexagonal units at the four corners of the quadrilateral primitive cell, but no $MgZn_2$ rhombic units within the cell compared with Mg_4Zn_7. $Mg_{22}Zn_{34}$ in **Fig. 3.10(d)** have the two units arranged in a rotational way, leading to the structural feature of the five-pointed star.

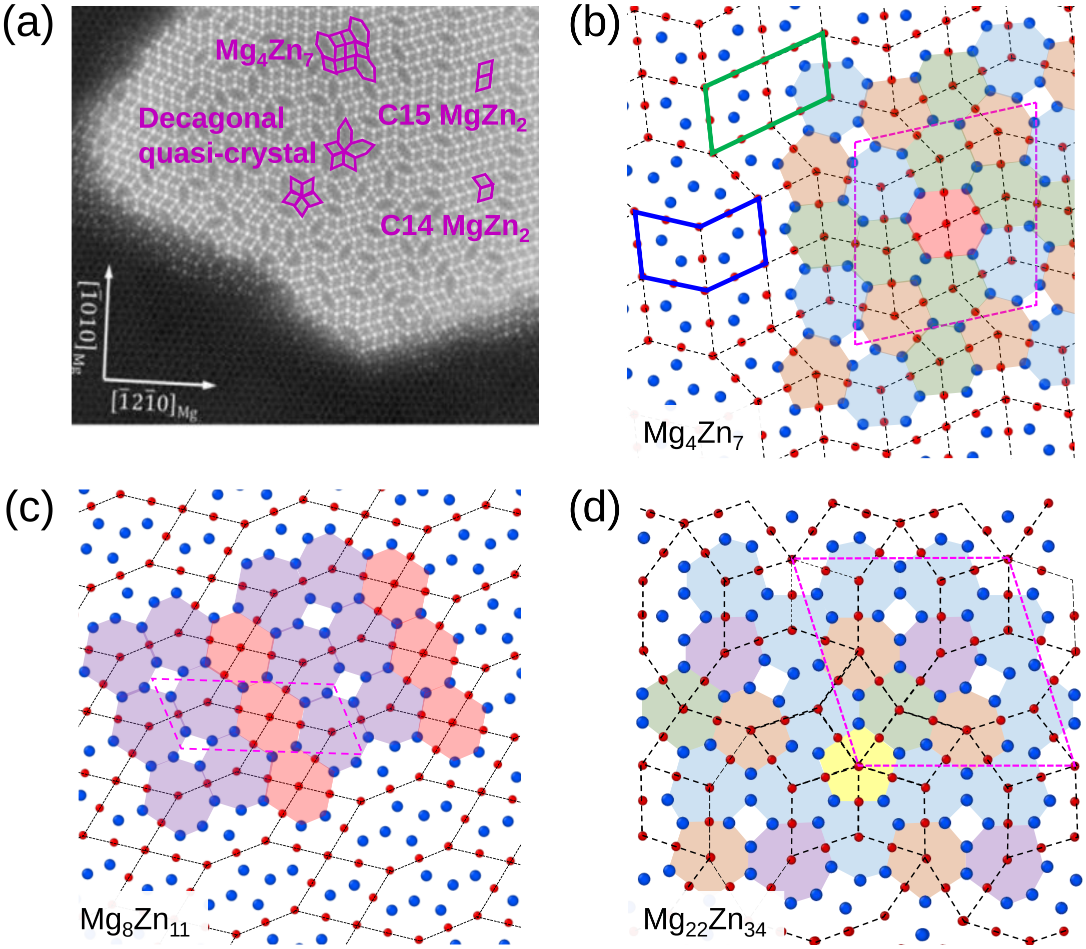

Fig. 3.10 (a) The cross section of a β_1' rod on $(0001)_{\text{Mg}}$ plane adapted from [25], **(b)** atomic structure of Mg4Zn7, (c) Mg8Zn11, (d) Mg22Zn34 viewed along direction equivalent to $[2\bar{1}\bar{1}0]_{\text{C}14}$. The blue and red spheres represent Mg and Zn atoms respectively. The basic units are indicated by thin dashed black lines. The primitive cells are indicated by dashed pink lines. The blue and green lines indicate the structural features of C14 and C15 MgZn2 phase, respectively. The colored polygons indicate different icosahedra.

The formation energies of the six structures from DFT are shown with global convex hull in **Fig. 3.11**, where $Mg_{32}Zn_{59}$ (-137.9 meV/atom), Mg_4Zn_7 (-134.8 meV/atom), $Mg_{29}Zn_{48}$ (-133.4 meV/atom) and $Mg_{22}Zn_{34}$ (-130.0 meV/atom) are within 1 meV/atom from the global convex hull, which essentially reside on the convex hull considering that the error bar of DFT energies. In contrast, $Mg_{28}Zn_{41}$ (-126.4 meV/atom) and Mg_8Zn_{11} (-106.9 meV/atom) are 2.5 and 19.8 meV/atom above the global convex hull, respectively. With the increasing Zn concentration, these structures are more stable with structurally decreasing portion of the Mg_6Zn_7 elongated hexagonal units and increasing portion of the $MgZn_2$ rhombic units based on their relative positions to the global convex hull. Therefore, it is inferred that the $MgZn_2$ rhombic unit is more thermodynamically favored than the Mg_6Zn_7 elongated hexagonal unit within β_1' rods, while the

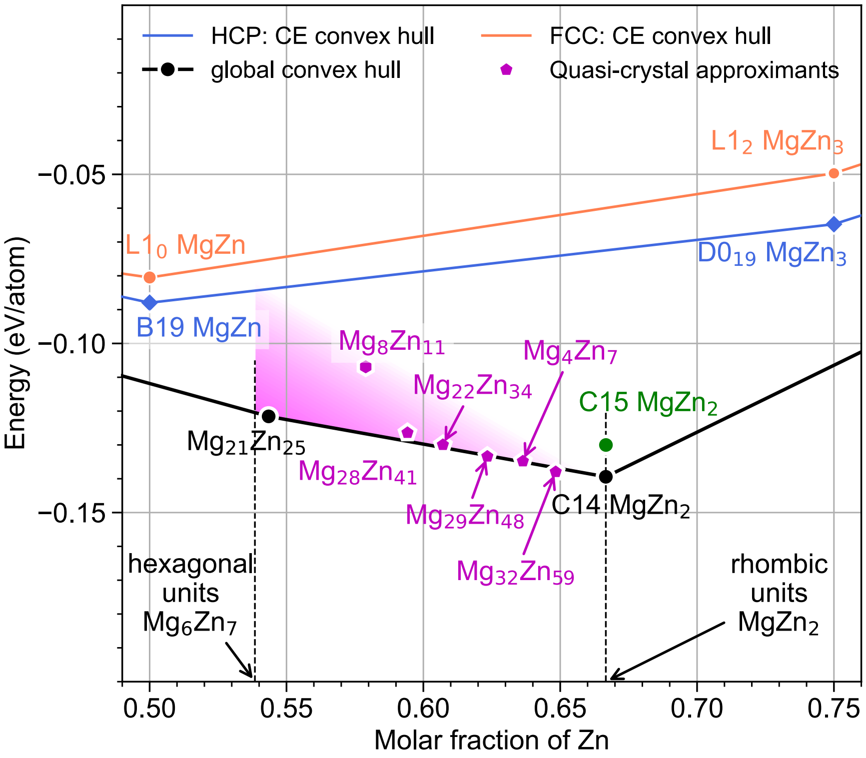

Fig. 3.11 Formation energies and relative positions to the convex hulls of six structures formed by the $MgZn_2$ rhombic and Mg_6Zn_7 elongated hexagonal units

latter are formed due to the Mg enrichment in the local regions. Thus, a general trend is expected for the stabilities of crystalline structures built by the $MgZn_2$ rhombic and the Mg_6Zn_7 hexagonal units: as the fraction of rhombic units (or Zn concentration) increases, the structures in this family become more stable. This means that there are many structures with large portions of the $MgZn_2$ rhombic units, especially when forming C14 $MgZn_2$, residing on the global convex hull, which is consistent with many observed β_1' rods having large domains of C14 $MgZn_2$ in experiments [25,55,111].

With various arrangements of the two basic units, the crystalline structures can have large primitive cells (e.g., hundreds of atoms or more), and the upper limit is the structures with infinitely large cells, i.e., 2D quasicrystal with the lack of translational symmetry on the plane equivalent to $\{2\bar{1}\bar{1}0\}_{\mathrm{C14}}$ within β_1' precipitates [25,44]. Several independent experiments revealed the existence of 2D decagonal quasi-crystalline structures [25,44]. These decagonal quasi-crystalline structures can be built from relatively simple icosahedra with 13 atoms [44]. Since these 2D quasicrystals and their approximants share similar local structures, Mg_4Zn_7, Mg_8Zn_{11} and $Mg_{22}Zn_{34}$ in **Figs. 3.10(b)-(d)**, respectively, are used for illustration. These approximants are built from 6 types of icosahedral chains packed by simple icosahedra along the direction equivalent to $[0001]_{\mathrm{C14}}$ or $[001]_{\mathrm{Mg4Zn7}}$, identified by different colors. The arrangement of green and red icosahedral chains leads to the zigzagged and aligned arrangements of the $MgZn_2$ rhombic units corresponding to C14 and C15 $MgZn_2$, respectively. The yellow one corresponds to the five-pointed star. Icosahedral chains in other colors are on the corners of the Mg_6Zn_7 elongated hexagonal units. Thus, from the DFT calculations, it is inferred that the energies of these clusters are higher than the green ones leading to C14 $MgZn_2$. Rather than only determined by thermodynamic stability, the specific atomic structure of the quasicrystal is very sensitive to local atomic environment (e.g., composition and structural defect) and is determined by the competition between the assimilation of the icosahedral clusters with relative lower energies and the trapping of local configurations due to suppressed kinetics [92,93].

Based on their HAADT-STEM results, Bendo et al. reported that there is a positive correlation between the aspect ratios of the $(0001)_\alpha$ cross-section of β_1' precipitates and the Zn/Mg ratios within β_1'. [25] Combining this trend with the one in current stability analysis, there is a further correlation between the stability and morphology of β_1'. Those β_1' with lower Zn concentration (more hexagonal Mg_6Zn_7 units) and correspondingly a smaller cross-sectional aspect ratio following the rod-like morphology is less stable. Oppositely, those β_1' with higher Zn concentration (more rhombic $MgZn_2$ units) and correspondingly a lager cross-sectional aspect ratio following the lath-like morphology is more stable.

3.4 Discussion and Conclusion

3.4.1 Discussion

It has been reported that both C14 (zigzagged-packed $MgZn_2$ rhombic units on $(2\bar{1}\bar{1}0)_{C14}$ plane) and C15 $MgZn_2$ (aligned-packed $MgZn_2$ rhombic units on $[010]_{C15}$ plane) Laves phases can be formed directly from the relaxation of HCP orderings [26,114]. Detailed analysis in the current study shows that both phases can be formed from the orderings with same ordered unit layers but stacked differently along $[0001]$ direction of the HCP lattice. As shown in the blue rectangle in **Fig. 3.12**, such unit layer is characterized by one layer of Zn on the basal plane and another layer of each Zn atom 6-fold coordinated by Mg atoms on the neighboring basal plane. If the ordering units are stacked along the $[0001]_\alpha$ direction without shift on basal plane, relaxation

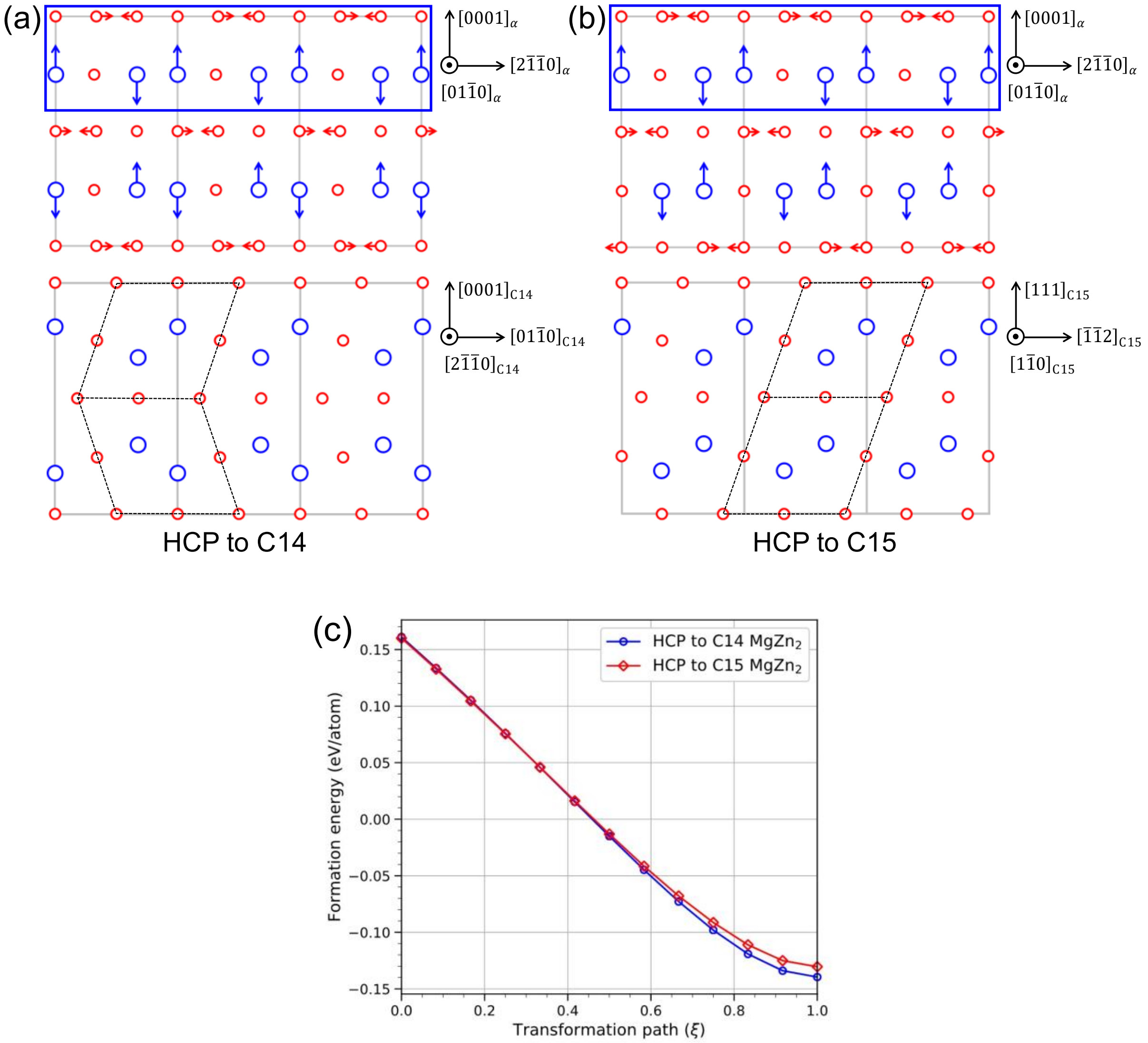

Fig. 3.12 Transformation paths from HCP ordering phases to C14 and C15 MgZn2: **(a)** atomic displacements of HCP ordering (upper) that leads to C14 MgZn2 (lower); **(b)** atomic displacements of HCP ordering (upper) that leads to C15 MgZn2 (lower); **(c)** Changes of formation energies along the linearly interpolated transformation paths. Note that the blue and red circles denote Mg and Zn, respectively.

of such structures leads to the C14 $MgZn_2$ phase (**Fig. 3.12(a)**). Alternatively, if adjacent ordering units are shifted by a along $[2\bar{1}\bar{1}0]_\alpha$ direction, relaxation would lead to C15 $MgZn_2$ phase (Fig. 12(b)).

For both cases, during relaxation, atoms on the pure Zn layers move within this layer to form the Kagome network, and Mg atoms on the adjacent layers move upward or downward along $[0001]_\alpha$ direction towards the open area of the Kagome nets on the neighboring layers [26,114]. The atomic displacements during the structural relaxation are indicated by the arrows in **Fig. 3.12**. The changes of formation energies along the linearly interpolated transformation pathways are shown in **Fig. 3.12(c)**, where no energy barrier is observed, indicating both transitions proceed instantaneously. Specifically, the energies of the HCP orderings before transformation are the same while C14 (-139.5 meV/atom) is more stable than C15 (-130.4 meV/atom) at the end of the transformation path, which explains the prevalence of C14 over C15 in Mg-Zn alloy system. These transformation paths lead to orientation relationship with the Mg matrix of $(0001)_{\mathrm{C14}} \parallel (0001)_{\mathrm{Mg}}$ and $[1\bar{1}00]_{\mathrm{C14}} \parallel [11\bar{2}0]_{\mathrm{Mg}}$ for C14 $MgZn_2$ and $(111)_{\mathrm{C15}} \parallel (0001)_{\mathrm{C14}}$ and $[1\bar{1}0]_{\mathrm{C15}} \parallel [2\bar{1}\bar{1}0]_{\mathrm{C14}}$ for C15 $MgZn_2$. Note that these orientation relationships for C14 and C15 $MgZn_2$ with HCP Mg agree with the experimentally observed orientation relationships between β_2' laths and β_1' rods with the Mg matrix [18,25].

Based on the OR between α-Mg and C14 $MgZn_2$ determined by the above transformation paths, the origin of the two major distinct orientation relationships of C14 $MgZn_2$ in β_2' with α-Mg are discussed, i.e., β_2' plates on the $(0001)_\alpha$ plane with $(0001)_{\mathrm{C14}} \parallel (0001)_{\mathrm{Mg}}$ and $[11\bar{2}0]_{\mathrm{C14}} \parallel [10\bar{1}0]_{\mathrm{Mg}}$ (denoted as OR1) and β_2' laths with $[0001]_{\mathrm{C14}} \parallel [11\bar{2}0]_\alpha$ and $(11\bar{2}0)_{\mathrm{C14}} \parallel (0001)_\alpha$ (denoted as OR2). [18,20] The β_2' plate with OR1 is consistent with the OR determined by the discussed transformation path. On the other hand, the β_2' lath with OR2 (observed along with β_1') have the similar structure, orientation relationship and morphology as some β_1' precipitates with a large cross-sectional aspect ratio [20,25]. Therefore, β_2' lath with OR2 is a structural limit of β_1' precipitates built almost entirely by C14 $MgZn_2$.

Based on the combined information of the ORs, the stability analysis of structures in Sec. 4, and the observation of precipitation in experiments, it is inferred that β_2' precipitates with the two distinct ORs and morphologies forms in different paths. The plate-like β_2' precipitates with OR1 can be formed from (i) the relaxation of the coherent ordering on HCP Mg matrix as discussed, and further coarsens to plates on basal plane of α-Mg; (ii) the decomposition of the less stable β_1' rods to the stable C14 $MgZn_2$, which corresponds to the decreased amount of β_1' rods and increased amount of β_2' plates with OR1 in prolonged aging process [18]. In contrast, the lath-like β_2' precipitates with OR2 are formed in the same way as β_1' rods but with very large fraction (or completely) of the structure being C14 $MgZn_2$. Additionally, it is suggested that β phase has a structure of $Mg_{21}Zn_{25}$ (space group $R\bar{3}c$), which consists of hexagonal prisms of C14 $MgZn_2$ and Mg-rich transition regions [38]. Note that β_2' (i.e., the C14 Laves phase) is a very stable compound and is very unlikely to transform to other structures at the common aging temperatures of Mg alloys, e.g., 300 K (27 °C) to 500 K (227 °C), where the kinetics is suppressed. Therefore, in practical aging treatment, the formation of β precipitate is likely to be suppressed due to low temperatures and difficult to be observed, although β is the equilibrium phase with α-Mg [20,39,62].

Based on the current understanding on the precipitation process in the Mg-Zn alloy, the likely precipitation sequence is summarized in **Fig. 3.13**. In the usual notation for precipitation sequence, two precipitates that form consecutively during aging are connected by solid arrows, i.e., A→B. This notation can lead to some confusion, since, other than thermodynamic stability, it can also be interpreted that B nucleates kinetically on the structure of A, where there usually exists a specific orientation relationship between A and B. To avoid the confusion in **Fig. 3.13**, arrows

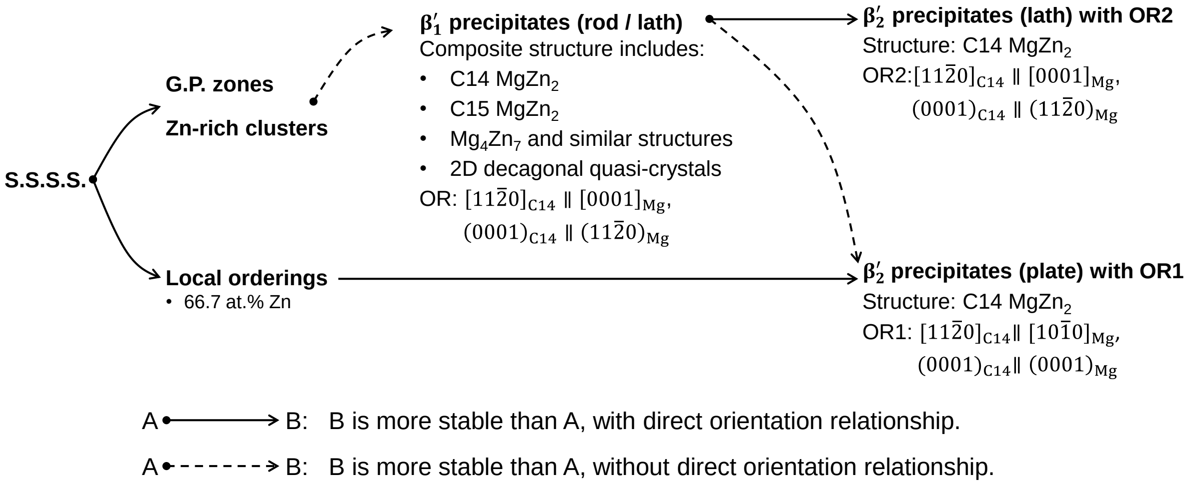

Fig. 3.13 The proposed precipitation sequence for supersaturated Mg-Zn solid solution during aging.

with solid lines are used if an orientation relationship exists between consecutively formed precipitates, while arrows with dashed lines are used if there is no clear orientation relationship.

3.4.2 Conclusions

In the current work, the research status on crystal structures and stabilities of phases in Mg-Zn system is reviewed, and comprehensive first-principles calculations are performed to examine the crystal structures and phase stability of precipitates and explore the remaining controversies. The main conclusions are summarized as the following.

(1) Current calculations predict GP zones on $\{01\bar{1}0\}_{Mg}$, $\{2\bar{1}\bar{1}0\}_{Mg}$ and $\{0001\}_{Mg}$ planes, on which plate-like GP zones are reported in experiments to reside. The stabilities of the predicted GP zones at finite temperature are calculated and compared with experiments. Further, the effect of CSE on the stabilities of GP zones is explained in the case of GP sheets on $\{01\bar{1}0\}_{Mg}$ plane, i.e., the double-layered GP sheet in B19 family and the zigzagged one in $D0_{19}$ family.

(2) The β_1' precipitate is made up of the $MgZn_2$ rhombic and the Mg_6Zn_7 elongated hexagonal units, which, with different arrangements, leads to domains of C14 and C15 $MgZn_2$, Mg_4Zn_7, 2D decagonal quasi-crystals and other decagonal approximants. The β_1' with more Mg_6Zn_7 elongated hexagonal units are less stable than ones with more $MgZn_2$ rhombic units building regions of C14 $MgZn_2$.

(3) The β_2' (C14 $MgZn_2$) precipitates with OR1, i.e., $(0001)_{C14} \parallel (0001)_{Mg}$ and $[11\bar{2}0]_{C14} \parallel [10\bar{1}0]_{Mg}$ can form from the relaxation of the specific low energy ordering with 66.7 at. % Zn, while the β_2' with OR2, i.e., $[0001]_{C14} \parallel [11\bar{2}0]_{Mg}$ and $(11\bar{2}0)_{C14} \parallel (0001)_{Mg}$ forms by the same mechanism as that of the β_1' rod.

References

[1] T.M. Pollock, Weight loss with magnesium alloys, *Science (80-.).* 328 (2010) 986–987.

[2] M. Hakamada, T. Furuta, Y. Chino, Y. Chen, H. Kusuda, M. Mabuchi, Life cycle inventory study on magnesium alloy substitution in vehicles, *Energy*. 32 (2007) 1352–1360.

[3] J.F. Nie, Precipitation and hardening in magnesium alloys, *Metall. Mater. Trans. A*. 43A (2012) 3891–3939.

[4] Y. Lu, A.R. Bradshaw, Y.L. Chiu, I.P. Jones, The role of β′ precipitates in the bio-corrosion performance of Mg-3Zn in simulated body fluid, *J. Alloys Compd.* 614 (2014) 345–352.

[5] B. Zhou, J. Chen, H. Yan, W. Xia, B. Su, H. Guo, W. Zhu, To improve strength and bio-corrosion resistance of Mg-4Zn alloy via high strain rate rolling combined with double aging, *Mater. Lett.* 227 (2018) 301–304.

[6] H. Pan, Y. Ren, H. Fu, H. Zhao, L. Wang, X. Meng, G. Qin, Recent developments in rare-earth free wrought magnesium alloys having high strength: A review, *J. Alloys Compd.* 663 (2016) 321–331.

[7] H. Okamoto, Comment on Mg-Zn (Magnesium-Zinc), *J. Phase Equilibria*. 15 (1994) 129–130.

[8] N.E.L. Saris, E. Mervaala, H. Karppanen, J.A. Khawaja, A. Lewenstam, Magnesium: An update on physiological, clinical and analytical aspects, *Clin. Chim. Acta*. 294 (2000) 1–26.

[9] D. Zhu, I. Cockerill, Y. Su, Z. Zhang, J. Fu, K.W. Lee, J. Ma, C. Okpokwasili, L. Tang, Y. Zheng, Y.X. Qin, Y. Wang, Mechanical strength, biodegradation, and in vitro and in vivo biocompatibility of Zn biomaterials, *ACS Appl. Mater. Interfaces*. 11 (2019) 6809–6819.

[10] P. Han, M. Tan, S. Zhang, W. Ji, J. Li, X. Zhang, C. Zhao, Y. Zheng, Y. Chai, Shape and site dependent in vivo degradation of Mg-Zn pins in rabbit femoral condyle, *Int. J. Mol. Sci.* 15 (2014) 2959–2970.

[11] M. Gupta, N.M.L. Sharon, Introduction to Magnesium, *Magnesium, Magnes. Alloy. Magnes. Compos.* (2010) 1–12.

[12] J.B. Clark, Transmission electron microscopy study of age hardening in a Mg-5 wt.% Zn alloy, *Acta Metall.* 13 (1965) 1281–1289.

[13] J.S. Chun, J.G. Byrne, Precipitate strengthening mechanisms in magnesium zinc alloy single crystals, *J. Mater. Sci.* 4 (1969) 861–872.

[14] G. Mima, Y. Tanaka, Main factors affecting the aging of magnesium- zinc alloys, *Trans. Japan Inst. Met.* 12 (1971) 76–81.

[15] G. Mima, Y. Tanaka, Mechanism of Precipitation Hardening of Magnesium-Zinc Alloys, *Trans. Japan Inst. Met.* 12 (1971) 323–328.

[16] G. Mima, Y. Tanaka, The aging characteristics of magnesium-4wt% zinc alloy, *Trans. Japan Inst. Met.* 12 (1971) 71–75.

[17] T. Takahashi, Y. Kojima, K. Takanishi, Study of precipitates in an aged Mg-3. 6 wt% Zn alloy by an X-ray method, *Japan Inst. Light Met.* 23 (1973) 376–382.

[18] L.Y. Wei, G.L. Dunlop, H. Westengen, Precipitation Hardening of Mg-Zn and Mg-Zn-RE Alloys, *Metall. Mater. Trans. A.* 26 (1995) 1705–1716.

[19] S.Y. Komatsu, M. Ikeda, U. Mori, M. Abe, Increase in resistivity of Mg-Zn alloys by low temperature aging, *J. Japan Inst. Light Met.* 54 (2004) 131–136.

[20] X. Gao, J.F. Nie, Characterization of strengthening precipitate phases in a Mg-Zn alloy, *Scr. Mater.* 56 (2007) 645–648.

[21] J. Buha, Reduced temperature (22-100 °C) ageing of an Mg-Zn alloy, *Mater. Sci. Eng. A.* 492 (2008) 11–19.

[22] R. Alizadeh, R. Mahmudi, T.G. Langdon, Creep mechanisms in an Mg-4Zn alloy in the as-cast and aged conditions, *Mater. Sci. Eng. A.* 564 (2013) 423–430.

[23] M. Němec, V. Gärtnerová, M. Klementová, A. Jäger, Analysis of intermetallic particles in Mg-12 wt.%Zn binary alloy using transmission electron microscopy, *Mater. Charact.* 106 (2015) 428–436.

[24] B. Langelier, G. Sha, A. Korinek, P. Donnadieu, S.P. Ringer, S. Esmaeili, The effects of microalloying on the precipitate microstructure at grain boundary regions in an Mg-Zn-based alloy, *Mater. Des.* 119 (2017) 290–296.

[25] A. Bendo, T. Maeda, K. Matsuda, A. Lervik, R. Holmestad, C.D. Marioara, K. Nishimura, N. Nunomura, H. Toda, M. Yamaguchi, K. ichi Ikeda, T. Homma, Characterisation of structural similarities of precipitates in Mg–Zn and Al–Zn–Mg alloys systems, *Philos. Mag.* 99 (2019) 2619–2635.

[26] S. Liu, G. Esteban-Manzanares, J. Llorca, First-principles analysis of precipitation in Mg-Zn alloys, *Phys. Rev. Mater.* 4 (2020) 93609.

[27] W. Kohn, L.J. Sham, Self-Consistent Equations Including Exchange and Correlation Effects, *Phys. Rev.* 140 (1965) A1133.

[28] P. Hohenberg, W. Kohn, Inhomogeneous Electron Gas, *Phys. Rev.* 136 (1964) 864.

[29] A. van de Walle, Methods for first-principles alloy thermodynamics, *JOM*. 65 (2013) 1523–1532.

[30] A. van de Walle, M. Asta, Self-driven lattice-model Monte Carlo simulations of alloy thermodynamic properties and phase diagrams, *Model. Simul. Mater. Sci. Eng.* 10 (2002) 521–538.

[31] I. Higashi, N. Shiotani, M. Uda, T. Mizoguchi, H. Katoh, The crystal structure of Mg51Zn20, *J. Solid State Chem.* 36 (1981) 225–233.

[32] M. Hida, Y. Matsui, The pseudocubic approximant Mg51Zn20 interpreted as a modulated crystal, *Philos. Mag. A*. 82 (2002) 831–839.

[33] X. Gao, J.F. Nie, Structure and thermal stability of primary intermetallic particles in an Mg-Zn casting alloy, *Scr. Mater.* 57 (2007) 655–658.

[34] L. Tarschisch, Röntgenographische Untersuchung der Verbindungen MgZn und MgZn5, *Zeitschrift Für Krist. Mater.* 86 (1933) 423–438.

[35] R. Černý, G. Renaudin, The intermetallic compound Mg21Zn25, *Acta Crystallogr. C*. 58 (2002) 154–155.

[36] Y. Khan, Dynamic temperature crystallization behaviour of amorphous and liquid Mg70Zn30 alloy, *J. Mater. Sci.* 24 (1989) 963–973.

[37] J.B. Clark, F.N. Rhines, Central region of the Mg-Zn phase diagram, *JOM*. 9 (1957) 425–430.

[38] L. Zhang, W. Wang, W. Hu, Z. Yang, H. Ye, Nanometer-sized domain structure in complex Mg21Zn25 formed by eutectoid phase transformation in a Mg-Zn alloy, *J. Alloys Compd.* 745 (2018) 319–330.

[39] C.C. Kammerer, S. Behdad, L. Zhou, F. Betancor, M. Gonzalez, B. Boesl, Y.H. Sohn, Diffusion kinetics, mechanical properties, and crystallographic characterization of intermetallic compounds in the Mg-Zn binary system, *Intermetallics*. 67 (2015) 145–155.

[40] K. Cenzual, E. Parthé, R.M. Waterstrat, Zr21Re25, a new rhombohedral structure type containing 12 Å-thick infinite MgZn2(Laves)-type columns, *Acta Crystallogr. C*. 42 (1986) 261–266.

[41] J. Gallot, R. Graf, ., *Comptes. Rendus. Acda. Sci.* 262B (1966) 1219.

[42] Y. Yarmolyuk, Crystal Structure of Mg4Zn7, *Kristallografiya*. 20 (1975) 538–542.

[43] Q. -B Yang, K.H. Kuo, A new description of pentagonal Frank–Kasper phases and a possible structure model of the icosahedral quasicrystal, *Acta Crystallogr. A*. 43 (1987) 787–795.

[44] Z. Yang, L. Zhang, M.F. Chisholm, X. Zhou, H. Ye, S.J. Pennycook, Precipitation of binary quasicrystals along dislocations, *Nat. Commun.* 9 (2018) 1–7.

[45] A. Ovchinnikov, V. Smetana, A.V. Mudring, Metallic alloys at the edge of complexity: structural aspects, chemical bonding and physical properties, *J. Phys. Condens. Matter*. 32 (2020).

[46] W.Z. Wang, X.Z. Zhou, Z.Q. Yang, Y. Qi, H.Q. Ye, A decagonal quasicrystal with rhombic and hexagonal tiles decorated with icosahedral structural units, *IUCrJ*. 7 (2020) 535–541.

[47] E. Abe, A.P. Tsai, short communications Orthorhombic tau -Zn - Mg - Dy phase related to a Frank- Kasper type decagonal quasicrystal, *Acta Crystallogr. B*. (2000) 915–917.

[48] M. Mihalkovič, J. Richmond-Decker, C.L. Henley, M. Oxborrow, Ab-initio tiling and atomic structure for decagonal ZnMgY quasicrystal, *Philos. Mag.* 94 (2014) 1529–1541.

[49] J.B. Friauf, The crystal structure of magnesium di-zincide, *Phys. Rev.* 29 (1927) 34–40.

[50] F. Laves, K. Lohberg, Die Kristallstruktur von intermet- allischen Verbindungen der Formel AB2 (The crystal structure of intermetallic compounds with formula AB2; in German), *Nachr Ges Wiss Go¨ttingen, Math-Phys Kl IV, Neue Folge*. 1 (1934) 59–66.

[51] F. Laves, H. Witte, Die Kristallstruktur des MgNi2 und seine Beziehungen zu den Typen des MgCu2 und MgZn2 (The crystal structure of MgNi2 and its relations to the MgCu2 and MgZn2 types; in German), *Met. Met. Met. Tech*. 14 (1935) 645–649.

[52] F. Stein, A. Leineweber, Laves phases: a review of their functional and structural applications and an improved fundamental understanding of stability and properties, *J. Mater. Sci.* 56 (2021) 5321–5427.

[53] T. Ohba, Y. Kitano, Y. Komura, The charge-density study of the Laves phases, MgZn2 and MgCu2, *Acta Crystallogr. C*. 40 (1984) 1–5.

[54] W.J. Kim, S.I. Hong, K.H. Lee, Structural characterization of Laves-phase MgZn2 precipitated in Mg-Zn-Y alloy, *Met. Mater. Int.* 16 (2010) 171–174.

[55] J.M. Rosalie, H. Somekawa, A. Singh, T. Mukai, Orientation relationships between icosahedral clusters in hexagonal MgZn2 and monoclinic Mg4Zn7 phases in Mg-Zn(-Y) alloys, *Philos. Mag.* 91 (2011) 2634–2644.

[56] A. Jain, S.P. Ong, G. Hautier, W. Chen, W.D. Richards, S. Dacek, S. Cholia, D. Gunter, D. Skinner, G. Ceder, K.A. Persson, Commentary: The materials project: A materials genome approach to accelerating materials innovation, *APL Mater.* 1 (2013).

[57] M. Andersson, M. de Boissieu, S. Brühne, C. Drescher, W. Assmus, S. Ohahshi, A.P. Tsai, M. Mihalkovič, M. Krajčí, Ö. Rapp, Electronic and structural properties of Laves-phase MgZn2 of varying chemical disorder, *Phys. Rev. B.* 82 (2010) 024202.

[58] A. Singh, J.M. Rosalie, Lattice correspondence and growth structures of monoclinic mg4 zn7 phase growing on an icosahedral quasicrystal, *Crystals*. 8 (2018).

[59] S. Samson, Ø. Ellefsen, O. Hassel, A. Kainulainen, A. Halonen, E. Pulkkinen, Die Kristallstruktur von Mg2Cu6Al5., *Acta Chem. Scand.* 3 (1949) 809–834.

[60] H. Euchner, M. Mihalkovič, F. Gähler, M.R. Johnson, H. Schober, S. Rols, E. Suard, A. Bosak, S. Ohhashi, A.-P. Tsai, S. Lidin, C.P. Gomez, J. Custers, S. Paschen, M. de Boissieu, Anomalous vibrational dynamics in the Mg2Zn11 phase, *Phys. Rev. B.* 83 (2011) 144202.

[61] Y. Murakami, K. Kawano, H. Tamura, Kyoto Univ. Memoirs of the Faculty of Eng., 1962.

[62] T. Bhattacharjee, C.L. Mendis, K. Oh-ishi, T. Ohkubo, K. Hono, The effect of Ag and Ca additions on the age hardening response of Mg-Zn alloys, *Mater. Sci. Eng. A.* 575 (2013) 231–240.

[63] D. Orlov, D. Pelliccia, X. Fang, L. Bourgeois, N. Kirby, A.Y. Nikulin, K. Ameyama, Y. Estrin, Particle evolution in Mg-Zn-Zr alloy processed by integrated extrusion and equal channel

angular pressing: Evaluation by electron microscopy and synchrotron small-angle X-ray scattering, *Acta Mater*. 72 (2014) 110–124.

[64] T. Bhattacharjee, C.L. Mendis, T.T. Sasaki, T. Ohkubo, K. Hono, Effect of Zr addition on the precipitation in Mg-Zn-based alloy, *Scr. Mater*. 67 (2012) 967–970.

[65] T. Bhattacharjee, T. Nakata, T.T. Sasaki, S. Kamado, K. Hono, Effect of microalloyed Zr on the extruded microstructure of Mg-6.2Zn-based alloys, *Scr. Mater*. 90 (2014) 37–40.

[66] L. Sturkey, J.B. Clark., Mechanism of age-hardening in magnesium-zinc alloys, *J. Inst. Met.* 88 (1959) 1960.

[67] L.L. Rokhlin, A. Oreshkina, Research Into the Structure of a Metastable Phase Formed During the Breakdown of a Supersaturated Solution in Magnesium--Zinc Alloys, *Fiz. Met. Met.* 66 (1988) 12–17.

[68] A. Singh, A.P. Tsai, Structural characteristics of β1′precipitates in Mg-Zn-based alloys, *Scr. Mater*. 57 (2007) 941–944.

[69] A. van de Walle, Multicomponent multisublattice alloys, nonconfigurational entropy and other additions to the alloy theoretic automated toolkit, Calphad 33 (2009) 266–278 .

[70] K. Wang, D. Cheng, C. Fu, B. Zhou, First-principles investigation of the phase stability and early stages of precipitation in Mg-Sn alloys, Phys. Rev. Mater. 013606 (2020) 1–13.

[71] M. Hellenbrandt, The inorganic crystal structure database (ICSD) - Present and future, *Crystallogr. Rev*. 10 (2004) 17–22.

[72] J.E. Saal, S. Kirklin, M. Aykol, B. Meredig, C. Wolverton, Materials design and discovery with high-throughput density functional theory: The open quantum materials database (OQMD), *JOM*. 65 (2013) 1501–1509.

[73] S. Wasiur-Rahman, M. Medraj, Critical assessment and thermodynamic modeling of the binary Mg-Zn, Ca-Zn and ternary Mg-Ca-Zn systems, *Intermetallics*. 17 (2009) 847–864.

[74] N.C. Verissimo, C. Brito, C.R. Afonso, J.E. Spinelli, N. Cheung, A. Garcia, Microstructure characterization of a directionally solidified Mg-12wt.%Zn alloy: Equiaxed dendrites, eutectic mixture and type/ morphology of intermetallics, *Mater. Chem. Phys.* 204 (2018) 105–131.

[75] C. Ravi, C. Wolverton, First-principles study of crystal structure and stability of Al-Mg-Si-(Cu) precipitates, *Acta Mater.* 52 (2004) 4213–4227.

[76] D. Wang, M. Amsler, V.I. Hegde, J.E. Saal, A. Issa, B.C. Zhou, X. Zeng, C. Wolverton, Crystal structure, energetics, and phase stability of strengthening precipitates in Mg alloys: A first-principles study, *Acta Mater.* 158 (2018) 65–78.

[77] R. Agarwal, S.G. Fries, H.L. Lukas, G. Petzow, E. Sommer, T.G. Chart, G. Effenberg, Assessment of the Mg-Zn System, *Int. J. Mater. Res.* 83 (1992) 216–223.

[78] M. Mihalkovic, M. Widom, Alloy database, *Http://Alloy.Phys.Cmu.Edu/*. (2011).

[79] A. Schneider, H. Klotz, J. Stendel, G. Strauss, Zur Thermochemie von Legierungen, *Pure Appl. Chem.* 2 (1961) 13–16.

[80] L.W. McKeehan, ., *Z. Krist. Tl. A.* 91 (1935) 501–503.

[81] R. King, O. Kleppa, A thermochemical study of some selected laves phases, *Acta Metall.* 12 (1964) 87–97.

[82] M. Morishita, H. Yamamoto, S. Shikada, M. Kusumoto, Y. Matsumoto, Thermodynamics of the formation of magnesium-zinc intermetallic compounds in the temperature range from absolute zero to high temperature, *Acta Mater.* 54 (2006) 3151–3159.

[83] A. Berche, C. Drescher, J. Rogez, M.C. Record, S. Brühne, W. Assmus, Thermodynamic measurements in the Mg-Zn system, *J. Alloys Compd.* 503 (2010) 44–49.

[84] V.W. Blitz, G. Hohorst, Die Bildungswärmen der Verbindungen von metallischem Magnesium mit metallischem Zink, Cadmium, Aluminium und Calcium, (1922) 1–21.

[85] Y. Komura, K. Tokunaga, Structural studies of stacking variants in Mg-base Friauf–Laves phases, *Acta Crystallogr. B.* 36 (1980) 1548–1554.

[86] A.R. Natarajan, E.L.S. Solomon, B. Puchala, E.A. Marquis, A. Van Der Ven, On the early stages of precipitation in dilute Mg-Nd alloys, *Acta Mater.* 108 (2016) 367–379.

[87] D. Cheng, E.R. Hoglund, K. Wang, J.M. Howe, S.R. Agnew, B. Zhou, Atomic structures of ordered monolayer GP zones in Mg-Zn-X (X = Ca , Nd) systems, *Scr. Mater.* 216 (2022) 114744.

[88] V. Vaithyanathan, C. Wolverton, L.Q. Chen, Multiscale modeling of θ′ precipitation in Al-Cu binary alloys, *Acta Mater.* 52 (2004) 2973–2987.

[89] V. Ozoliņš, C. Wolverton, A. Zunger, Strain-induced change in the elastically soft direction of epitaxially grown face-centered-cubic metals, *Appl. Phys. Lett.* 72 (1998) 427–429.

[90] C. Wolverton, First-principles theory of 250,000-atom coherent alloy microstructure, *Model. Simul. Mater. Sci. Eng.* 8 (2000) 323–333.

[91] J.M. Rosalie, H. Somekawa, A. Singh, T. Mukai, Structural relationships among MgZn2 and Mg4Zn 7 phases and transition structures in Mg-Zn-Y alloys, *Philos. Mag.* 90 (2010) 3355–3374.

[92] P.J. Steinhardt, H.C. Jeong, A simpler approach to Penrose tiling with implications for quasicrystal formation, *Nature*. 382 (1996) 431–433.

[93] A.S. Keys, S.C. Glotzer, How do quasicrystals grow?, *Phys. Rev. Lett.* 99 (2007) 1–4.

[94] A.R. Natarajan, A. Van Der Ven, Connecting the Simpler Structures to Topologically Close-Packed Phases, *Phys. Rev. Lett.* 121 (2018) 255701.

Chapter 4 includes: 1) the atomic structures of the GP zones, 2) the calculated lattice parameters and displacement fields. The first part is from the published paper: D. Cheng, E. R. Hoglund, K. Wang, J. M. Howe, S. R. Agnew, Bi-Cheng Zhou. “Atomic structures of ordered monolayer GP zones in Mg-Zn-X (X= Ca, Nd) systems.” Scripta Mater. 216 (2022): 114744. Author contributions: D. Cheng and K. Wang performed the DFT and CE calculations. E. R. Hoglund performed the STEM and SAED simulations and analyzed the results under the supervision of J. M. Howe. B.C. Zhou and S. R. Agnew conceived and supervised the project. All authors participated in discussion and writing the manuscript.

Chapter 4 GP zones in Mg-Zn-X (X=Ca, Nd) systems

4.1 Introduction

In a landmark study of Mg-2.4RE[1]-0.4Zn-0.6Zr (wt.%) alloy, Ping et al. [1] revealed that the monolayer disc-shaped Guinier-Preston (GP) zones on the basal plane of the hexagonal close-packed (HCP) Mg crystal possess an ordered structure. Previous studies of Mg-RE alloys revealed rod-shaped GP-zones parallel to the c-axis of α-Mg [2,3], and the addition of Zn was known to alter the precipitate sequence, inducing plate-shaped GP zones on the basal plane [1,4]. Ping et al. employed high-resolution transmission electron microscopy (HRTEM) and 3D atom probe (3D-APT) to show that the GP zones were comprised of enriched concentrations of both Nd and Zn solutes, and based on the selected area electron diffraction (SAED) patterns, these solutes are

---

[1] RE denotes a Ce-rich rare earth mischmetal comprised of 1.3 Ce, 0.6 La, 0.4 Nd and 0.1Pr (wt.%)

ordered. Based upon both the composition measured by 3D-APT and the symmetry of the SAED patterns, they surmised that each solute atom of Nd/Zn was surrounded by 6 Mg atoms on the basal plane (similar to **Fig. 4.4(a)** but with X=Nd/Zn).

Later, Oh-ishi et. al. [5] showed that Zn additions to Mg-0.3Ca (at%) give rise to an enhanced age-hardening response. This enhancement was attributed to a high number density of GP zones observed in peak-aged Mg-0.3Ca-0.6Zn (at.%). Such minor alloying additions had been previously suggested [6,7] as a means to overcome a classic challenge of heat treatable Mg alloys, namely a low number density of precipitates [8,9]. As in the case of the Mg-RE-Zn-Zr alloy discussed above, the GP zones were again found to be monolayer structures on the $(0001)_\alpha$ plane, and further, contrast variation high angle annular dark field-scanning transmission electron microscopy (HAADF-STEM) images revealed that these GP zones are ordered. In addition, their SAED patterns were consistent with those observed in Mg-RE-Zn-Zr [1], Mg-Gd-Zn [10] and Mg-Ca-Zn (-Nd) [11,12] alloys. Thus, it was concluded that the GP zones in the Mg-Ca-Zn alloys possess the previously suggested ordered structure, where each Zn/Ca solute atom is surrounded by 6 Mg atoms on the basal plane. Recently, Li et. al. used 3D-APT to reveal a 1:1 composition ratio of Zn/Ca within the GP zones in the Mg-0.3Ca-0.6Zn (at.%) alloy [13], suggesting that preferential solute interaction that leads to the GP zone with the concentrations different from the solute ratio in the solid solution. The present study was undertaken to determine the exact atomic structure of the ordered GP zones within Mg-Zn-X, where X is a solute with large atomic radius such as an alkaline earth element, Ca, or a rare earth element, Nd, and to show the driving force that leads to these orderings.

4.2 Calculations

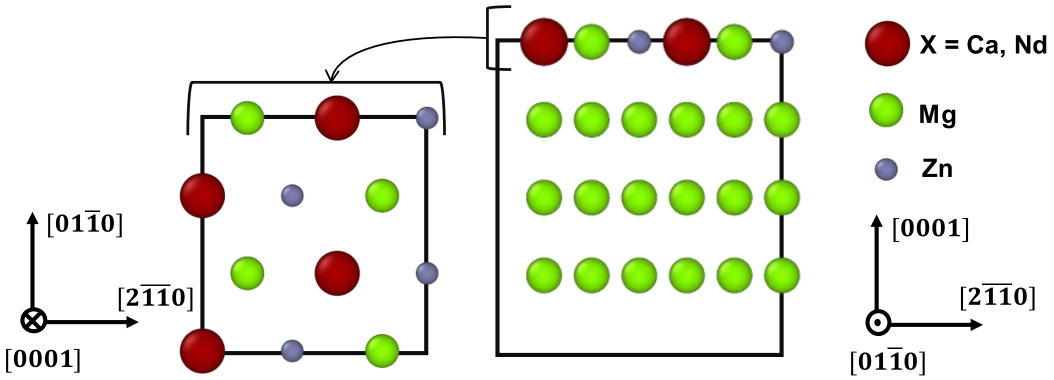

Fig. 4.1 The cluster expansion (CE) simulation cell: the atomic sites on the top layer along [0001] can be occupied by Mg-Zn-Ca or Mg-Zn-Nd atoms to form symmetrically distinct configurations (as shown in the left panel), and the sites on other layers can only be occupied by Mg atoms.

Here, first-principles electronic structure methods based on density functional theory (DFT) combined with the statistical-mechanical approach of cluster expansion (CE) were used to study the atomic structures of GP zones in Mg-Zn-X (X=Ca, Nd) systems. Since GP zones in both systems are confirmed to be ordered monolayer structures on the basal plane of HCP Mg matrix [1,5], CE is a suitable tool to search the 0 K ground states in the monolayer configurational space formed by the 3 species (Mg-Zn-Ca or Mg-Zn-Nd) on the basal plane of an HCP crystal.

The Alloy Theoretic Automated Toolkit (ATAT) [14] was used to perform CE to search for low energy GP zone structures. The CE unit cell employed in this work consists of four HCP basal planes, where the sites on the top layer can be occupied by Mg/Zn/Ca or Mg/Zn/Nd atoms, and the sites in the other three layers are occupied only by Mg, as shown in **Fig. 4.1**. The total energies of the supercell with symmetrically distinct orderings on the top layer were calculated by DFT, as implemented in the Vienna Ab-Initio Simulation (VASP) Package [15,16]. An energy cutoff of 400 eV was adopted for the plane-wave expansion of the electronic wave functions. The Methfessel-Paxton technique was employed, with a smearing parameter of 0.2 eV for integration over k-points. The Brillouin zone was sampled by Gamma-centered grids. The minimum density of k-points along reciprocal lattice vectors is 58 per $Å^{-1}$, which corresponds to 21×21×12 mesh for primitive HCP cell. The atomic positions were allowed to relax, while the cell shape and volume were fixed to mimic the constraint from the Mg matrix.

The MAPS code [14] in ATAT was used to generate the training sets and automate the DFT calculations. In both Mg-Zn-Ca and Mg-Zn-Nd systems, the low energy structures were searched among all the symmetrically distinct structures with the top layer of the CE cell up to 9 atoms. The ones below or close to the current convex hull predicted by CE were calculated by DFT and added to the training set iteratively. The leave one out cross-validation (LOOCV) score was used to optimize the choice of clusters to be included in a truncated CE. In this study, convergence of CE is reached once LOOCV is smaller than 5 meV/atom with no new ground state being predicted, and the effective cluster interactions (ECIs) do not change significantly if more configurations from DFT calculations are added into the training sets [17].

To better quantify the mixing tendencies of solute atoms on the top layer of the CE cell, the formation energy per CE site (or equivalently per atom in the monolayer GP zones) is adopted,

$$\Delta E_f^{GP}\left(Mg_pZn_qX_r\right) = \frac{E - pE_{GP-Mg} - qE_{GP-Zn} - rE_{GP-X}}{p+q+r} \tag{1}$$

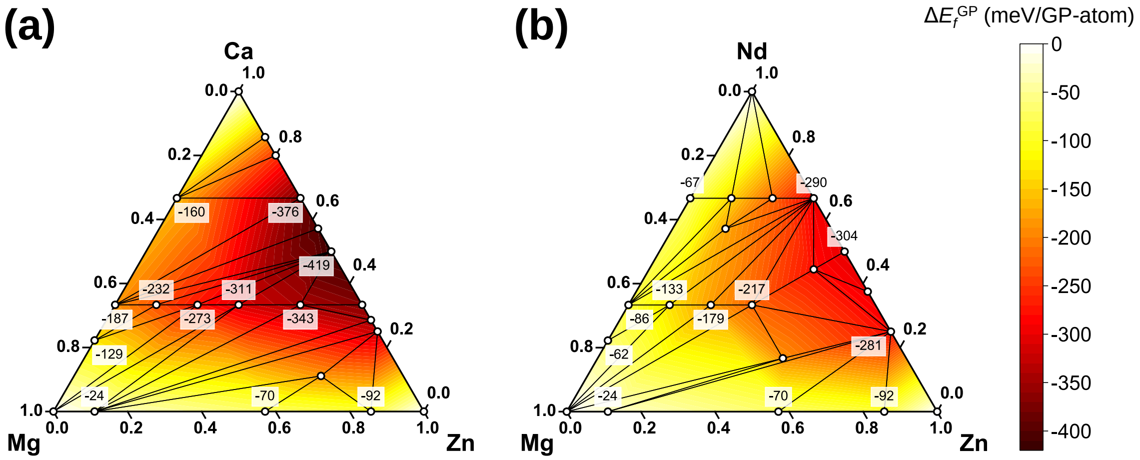

Fig. 4.2 The formation energy landscape of monolayer GP zones showing the mixing tendency of solutes in **(a)** Mg-Zn-Ca system and **(b)** Mg-Zn-Nd system. The endmember corresponds to the GP zone structure in which all the sites in the top layer of CE cell are occupied by one kind of atom.

where E is the energy of the CE cell; E_{GP-Mg}, E_{GP-Zn}, and E_{GP-X} are energies of endmembers with the top layer in the CE cell completely occupied by Mg, Zn, and Ca/Nd, respectively; p, q, and r are the number of Mg, Zn, and Ca/Nd atoms on the top layer. Color-coded using the defined formation energy (Eq. (1)), the energy landscape of the ground state structures at different compositions at 0 K for Mg-Zn-X (X= Ca, Nd) systems are shown in **Fig. 4.2(a) and 2(b)**, respectively. In **Fig. 4.2(a)**, based on the energies of ground state structures on the bounding binary systems, the bonding between Ca and Zn atoms are shown to be the most energetically favored, followed by the bonding between Mg and Ca atoms, while the bonding between Mg and Zn is the least favorable. This trend agrees with the experimental thermodynamic evaluation for the Mg-Zn-Ca system [5]. A similar trend is observed in the Mg-Zn-Nd system, as shown in **Fig. 4.2(b)**. The Zn-Nd bond is most energetically favorable, and Mg-Zn bond is the least favorable.

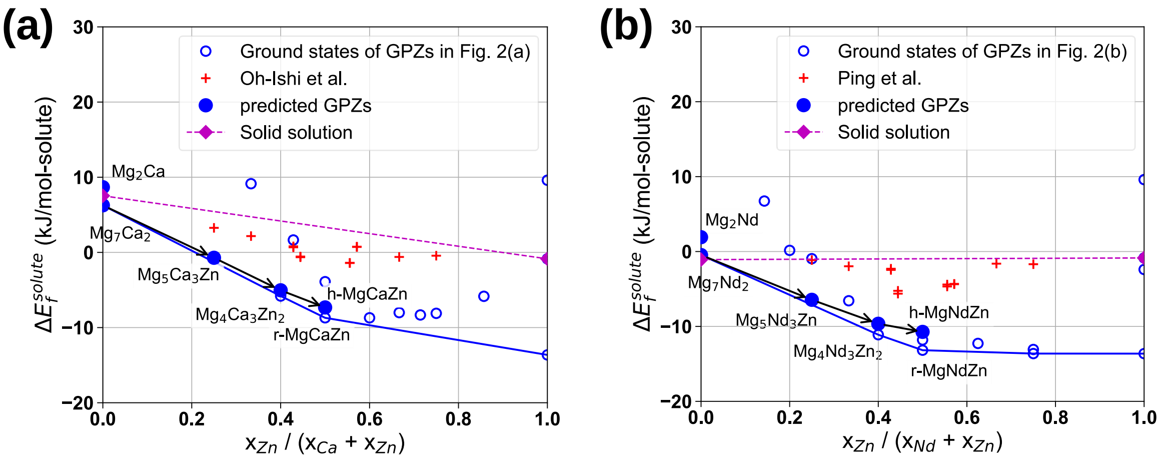

Fig. 4.3 The convex hull of formation energy *per solute atom* ΔE_f^{solute} of the monolayer ground states in **(a)** Mg-Zn-Ca system and **(b)** Mg-Zn-Nd system. The rationale for such plots can be found in [18,19]. The red crosses represent the calculated formation energies of GP zones using the structures proposed by Ping et al. [1] and Oh-ishi et. al. [5] based upon experiments.

To compare the thermodynamic stability of ground state GP zone structures in **Fig. 4.2** with varying Mg content and fixed Zn/X ratio, the formation energies *per solute atom* of the GP zones as bulk structures defined in CE cell are calculated using the following equation [18,19],

$$\Delta E_f^{solute}\left(Mg_P Zn_Q X_R\right) = \frac{\Delta E_f\left(Mg_P Zn_Q X_R\right)}{x_{Zn}+x_X} = \left(\frac{E-PE_{Mg}-QE_{Zn}-RE_X}{P+Q+R}\right)/(x_{Zn}+x_X) \qquad (2)$$

where E is the energy of the CE cell; E_{Mg}, E_{Zn}, and E_X are energies of pure constituents in their equilibrium crystal structures (HCP Mg, HCP Zn, FCC (face centered cubic) Ca and DHCP (double hexagonal close-packed) Nd); P, Q, and R are the number of Mg, Zn, and Ca/Nd atoms in the CE cell; x_{Zn} and x_X are the molar fractions; ΔE_f is the formation energy of a GP zone as bulk structure in the CE cell. The convex hulls of $\Delta E_f^{soulte}\left(Mg_P Zn_Q X_R\right)$ are plotted as a function of $x_{Zn}/(x_{Zn}+x_X)$ in **Fig. 4.3**. Several orderings in both Mg-Zn-X (X= Ca, Nd) systems fall on the convex hulls of ΔE_f^{soulte}, suggesting that the ordered monolayer GP zone in these two systems may have multiple structures, depending on the local composition ratio between the two solutes. It is noteworthy that the structures with only solutes atoms (X and Zn) in the monolayer GP zones show the lowest formation energies in the ternary diagrams of the two systems (**Fig. 4.2(a) and 2(b)**), but they are above the convex hull of ΔE_f^{soulte}, and thus not among the most stable structures under a given Zn/X ratio (**Fig. 3(a) and 3(b)**).

Table 4.1 DFT formation energies $\Delta E_f\left(Mg_P Zn_Q X_R\right)$ of predicted GP zones as bulk structures defined in CE cell (i.e., monolayer GP zone separated by 3 layers of Mg) in Mg-Zn-X (X = Ca, Nd) system. The reference states are HCP Mg, HCP Zn, FCC Ca, and DHCP Nd. Energies are in units of J/mol-atom.

	ΔE_f(X = Ca)	ΔE_f(X = Nd)
Mg_2X	722.7	159.2
Mg_7X_2	348.3	-26.1
Mg_5X_3Zn	-79.1	-715.9
$Mg_4X_3Zn_2$	-699.5	-1340.2
h-MgXZn	-1220.5	-1787.9

4.3 Predicted atomic structures of GP zones

The stable GP zones at different Zn/X ratios are derived based on the values of ΔE_f^{soulte} together with the 3-/6-fold rotational symmetry observed in experiments [1,5], as represented by the blue solid circles in **Fig. 4.3**. The atomic structure of Mg_2X (every X atom is 6-fold coordinated by Mg atoms on the $(0001)_{HCP}$ plane (shown in **Fig 4.4(a)**) is similar to the monolayer Mg_2(X, Zn) derived by Ping [1] and Oh-Ishi [5] based on their SAED patterns for the Mg-Zn-Nd and Mg-Zn-Ca systems, respectively. In Ping and Oh-ishi's Mg_2(X, Zn) structure, large X and small Zn atoms both reside on the X sites (the red sites in **Fig. 4.4(a)**), but the occupations of X and Zn are not determined. To compare the Mg_2(X, Zn) structures proposed by Ping [1] and Oh-Ishi [5] with the predicted GP zones in the current study, the possible site occupations of X and Zn in Mg_2(X, Zn) are enumerated up to 27 atoms per layer and DFT calculations were performed for the structures with $x_{Zn}/(x_{Zn}+x_X)$ close to 0.5 and 3-/6-fold rotational symmetry. As shown in **Fig.**

4.3(a) and 3(b), these structures have higher ΔE_f^{soulte} , and thus are thermodynamically unfavorable.

The energies of the Mg-rich solid solutions in both systems are estimated by the tie-line connecting the energies of isolated X and Zn impurities in Mg matrix [18] (purple diamonds in **Fig. 4.3**). Most predicted GP zones are below the tie lines, meaning there are enthalpic driving forces for their formation from solid solutions. Although Mg_2X GP zones are above the tie lines, they may form as intermediate structures along the path of more stable GP zones as X atoms aggregate in Mg matrix. For both systems, there is a correlation between decreasing ΔE_f^{soulte} and increasing Zn/X ratio in the X-rich side, suggesting that the precipitation process of the predicted GP zones may proceed as $Mg_7X_2 \rightarrow Mg_5X_3Zn \rightarrow Mg_4X_3Zn_2 \rightarrow$ h-MgCaZn, as shown by the black

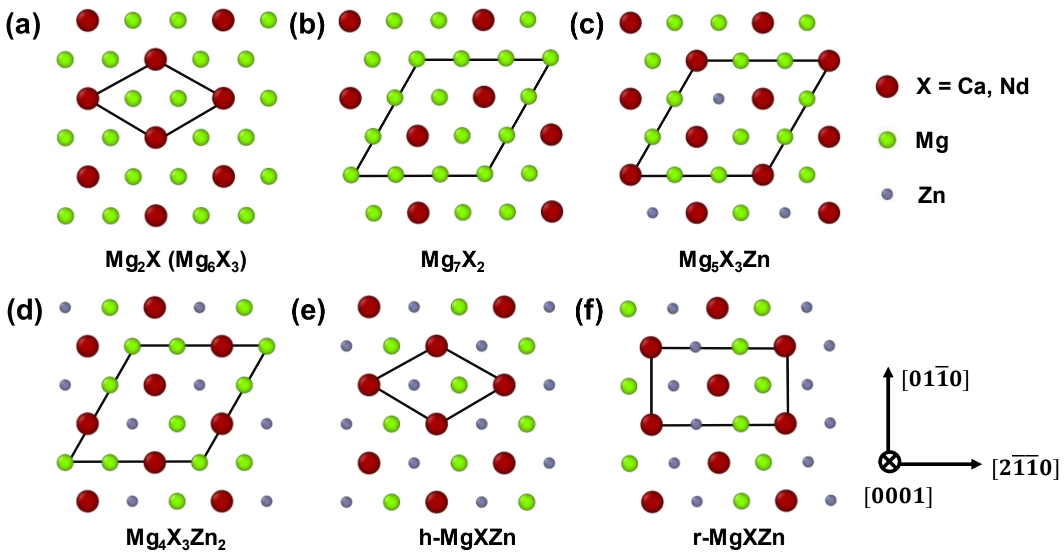

Fig. 4.4 Potential ordered coherent monolayer GP zones at $(0001)_{HCP}$ plane under different ratios of $x_{Zn}/(x_{Zn}+x_X)$. Primitive cells of each ordered structure are denoted in black lines. (a) monolayer Mg_2X at $x_{Zn}/(x_{Zn}+x_X) = 0$; (b) Mg_7X_2 at $x_{Zn}/(x_{Zn}+x_X) = 0$; (c) Mg_5X_3Zn at $x_{Zn}/(x_{Zn}+x_X) = 0.25$; (d) $Mg_4X_2Zn_2$ at $x_{Zn}/(x_{Zn}+x_X) = 0.4$; (e) h-MgXZn at $x_{Zn}/(x_{Zn}+x_X) = 0.5$; (f) r-MgXZn at $x_{Zn}/(x_{Zn}+x_X) = 0.5$.

arrows in **Fig. 4.3**. The formation energy ΔE_f of the predicted GP zones as bulk structures in CE cell are listed in Table1.

The atomic structures of the predicted coherent GP zones for the two systems are shown in **Fig. 4(a)-(f)**. With striking similarity, the predicted GP zones in the two systems are structurally related to monolayer Mg_2X. The structure of Mg_7X_2 in **Fig. 4.4(b)** is on the convex hull at $x_{Zn}/(x_{Zn}+x_X) = 0$ in **Fig. 4.3(a) and (b)**. It has a lower X concentration than Mg_2X in **Fig. 4.4(a)**. Specifically, one Mg atom sits on an X site in the monolayer Mg_6X_3 (3×monolayer Mg_2X). If this Mg atom is later replaced by X during the aggregation of solutes, it is accompanied by a decrease of energy (**Fig. 4.3**), as the GP zone composition heads towards that of the equilibrium precipitate phase, and Mg_7X_2 thus evolves toward structures with a higher Zn/X ratio. The other structures in **Figs. 4.4(c)-4(f)** are monolayer Mg_6X_3 with 1, 2 and 3 Mg atoms replaced by Zn atoms, corresponding to the $x_{Zn}/(x_{Zn}+x_X)$ equals 0.25, 0.4, and 0.5, respectively.

Unlike the GP zone structure proposed by Ping et al. [1] and Oh-ishi et al. [5] where each solute atom (i.e., X or Zn) is surrounded by 6 Mg atoms, Zn atoms prefer to occupy the site of Mg atoms rather than sharing the symmetrically equivalent site of X within the monolayer Mg_2X in our calculations. Based on the energy surface in **Fig. 4.2(a)**, it is clear that the replacement of X with Zn in the monolayer Mg_2X will increase the number of Mg-Zn bonds and correspondingly increase the formation energy. Meanwhile the replacement of Mg with Zn will increase the number of Ca-Zn bonds and decrease the formation energy. Thus, the monolayer Mg_2X structure, with Mg replaced by Zn is thermodynamically preferable in both systems.

The predicted GP zones with a Zn/X ratio of 1:1 is consistent with the 3D-APT result of the GP zones in the Mg-0.3Ca-0.6Zn (at.%) alloy from Li et al. [13]. Note that there are two different 1:1 orderings, i.e., hexagonal (h-MgXZn) and rectangular (r-MgXZn). In both Mg-Zn-

Ca and Mg-Zn-Nd systems, h-MgXZn is near the convex hull and r-MgXZn is on the convex hull, as annotated in **Fig. 4.3**. The structural difference between the two orderings depends on the arrangement of the three Zn atoms that replace the three Mg atoms within the monolayer Mg_6X_3 in **Fig. 4.4(a)**. In h-MgXZn, three Zn atoms replace every other Mg atom around each X atom, leading to a 3-fold symmetric precipitate, as shown in **Fig. 4.4(e)**. In r-MgXZn, three consecutive Zn atoms replace Mg atoms around each X atom, leading to zigzag patterns of Zn and Mg atoms along a $[01\bar{1}0]$ direction with 2-fold symmetry, as shown in **Fig. 4.4(f)**. The maximum 2-fold symmetry of the r-MgXZn structure does not agree with the minimal 3- or 6-fold symmetry found in experimental SAED patterns [1,5]. Therefore, we determine that h-MgXZn with the minimal 3-fold symmetry a viable candidate at $x_{Zn}/(x_{Zn}+x_X) = 0.5$.

Of the MgXZn structures, with relaxed atomic positions, DFT predicts that r-MgXZn has lower energy than h-MgXZn, as shown in **Fig. 4.3(a) and (b)**. However, when atoms are not relaxed from the initial position at Mg crystal, strain exists in the supercell and leads to h-MgXZn having a lower energy than r-MgXZn. Note that the atomic size difference between Zn and Nd is larger than that between Zn and Ca. Therefore, the strain penalty may play a larger role in Mg-Zn-Nd, which is reflected in the larger energy difference between h-MgXZn and r-MgXZn at a composition of $x_{Zn}/(x_{Zn}+x_X) = 0.5$ in **Fig. 4.3(b)** of Mg-Zn-Nd than that in **Fig. 4.3(a)** of Mg-Zn-Ca. Therefore, the strain energy contributions are enough to change the favorable metastable states in the monolayer structure. This result suggests that the matrix provides a higher degree of constraint during the early stages of aging than that is provided by the surrounding three Mg layers of the supercell employed in the present simulations. In the present calculations, it is found that structures with $x_{Zn}/(x_{Zn}+x_{Ca}) > 0.5$ (or Zn/Ca ratio larger than 1) often relaxe away from HCP lattice, indicating strong local distortions that could ultimately drive a loss of coherency toward the formation of other metastable phases like η’ or η” [13]. These later stage precipitates are beyond the scope of the current paper.

To determine the validity of the predicted GP zone structures, we simulated a HAADF image (**Fig. 4.5(a)**) and electron diffraction patterns (EDPs) along different zone axes (**Fig. 4.5(b) and (c)**) using h-MgCaZn as an example. Simulations of the atomic contrast were performed using the software abTEM [20]. The input parameters for all simulations include the acceleration voltage (E_0 = 200 kV), defocus (Δf = -0.05 nm), two-fold astigmatism (C_{12} = 0.05 nm), spherical aberration (C_s = 1.15 μm), and the defocus spread (9.3 nm) accounting for chromatic aberrations and a 1.3 eV energy resolution. Higher-order aberrations were included but will minimally affect the HAADF images, and to an even lesser extent the SAED patterns. The potentials for each supercell included three frozen-phonon configurations to account for atom thermal vibrations with a root-mean-square displacement of 21.4 pm, which was calculated from a thermal parameter of B = 1.2 given by reference [21].

For the HAADF image simulation, a convergence semi-angle of 25 mrad, inner collection angle of 90 mrad, and outer collection angle of 200 mrad were used. $[10\bar{1}0]$ zone axis supercells were created with [0001] parallel to the y-axis. A supercell ~6.7×1.0×10.0 nm using a 1×6 PRISM [22] interpolation was found to well represent the GP zone structures. The GP zones were half-circles with a 5 nm radius centered at upper x-bound and centered in the yz-plane, such that the left bound of the cell was pure Mg and the right bound had a monolayer of pure GP zone. EDPs were simulated with a 0.01 mrad convergence semi-angle. For [0001] and $[10\bar{1}0]$ zone axis EDPs, a supercell with a GP zone of h-MgCaZn structure extending infinitely in the xz-plane and bound by eight Mg basal planes was tilled to a supercell size of ~20×20×16 nm. Tiling in the y-axis introduces periodic GP zones that lead to finely spaced reciprocal lattice peaks rather than streaks

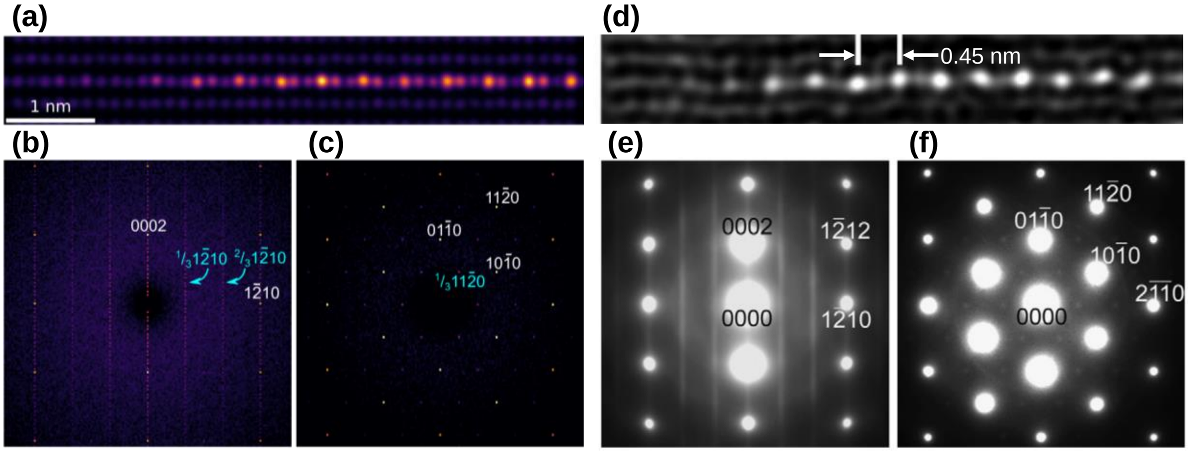

Fig. 4.5 (a) Simulated HAADF image of h-MgCaZn along the [10$\bar{1}$0] direction; **(b)** Simulated EDP of h-MgCaZn from the [10$\bar{1}$0] direction and **(c)** the [0001] direction; **(d)** HAADF images of the monolayer GP zone in peak-aged Mg–0.3Ca–0.6Zn alloy taken from the [10$\bar{1}$0] direction and **(e)** corresponding SAED patterns of the [10$\bar{1}$0] direction and **(f)** the [0001] directions. Figures (d)~(f) are reproduced from Oh-Ishi et al. [5].

found in experimental SAED patterns from randomly distributed GP zones. [0001] EDPs were also ~20×20×16 nm with the GP zone ~8 nm in the z-axis extending infinitely in the xy-plane. [0001] EDPs do not suffer from periodic GP zone tiling because tiling is performed in the xy-plane, which contain the GP zones.

Through the TEM simulations, it is found that the periodicity in the simulated [10$\bar{1}$0] HAADF image and EDPs share the 3×$(11\bar{2}0)$ ordering reported in experimental findings [1,5]. Streaked ordered reflections at 1/3[11$\bar{2}$0] and $2/3[11\bar{2}0]$ in the [10$\bar{1}$0] EDP (**Fig. 4.5(b)**) are from the relaxed Laue condition of a two-dimensional lattice. Theordering periodicity is consistent with experimental HAADF and SAED patterns of the monolayer GP zone in peak-aged Mg–0.3Ca–0.6Zn alloy (**Fig. 4.5(d)-(f)**) [5] In the [0001] EDP shown in **Fig. 4.5(c)**, there are 1/3$\langle 11\bar{2}0\rangle$ and 2/3$\langle 11\bar{2}0\rangle$ peaks further confirming that the h-MgXZn structure is a plausible candidate.

To summarize, through first-principles based cluster expansion, we predict multiple ordered monolayer GP zones exist in both Mg-Zn-Ca and Mg-Zn-Nd systems, which depend on the local solute concentration. Striking similarity is found in all the predicted GP zones in both systems that are all structurally related with monolayer Mg_2X. As the Zn/X ratio increases, Zn atoms replace Mg to decrease the formation energy of the GP zones. This is distinct from previously suggested replacement of X atoms by Zn, but is intuitive since Zn-X bonds are stronger than Mg-X. Through TEM simulations we find good agreement between the predicted low-energy h-MgCaZn structure and experimental observations, which further supports the predicted low-energy GP zone structures over previously less ordered counterparts. This new understanding helps to rationalize the occurrence of GP zones in the presently considered alloys and provides guidance for promotion of GP zones in other similar systems such as Mg-Al-Ca or Mg-Zn-Gd.

4.4 Lattice parameters of GP zones in Mg-Zn-Ca

The lattice parameter of pure Mg in DFT calculations are $a_{\mathrm{Mg}} = 0.319\ nm; c_{\mathrm{Mg}} = 0.518\ nm$. The coherent ordered GP zones in Mg-Zn-Ca have lattice mismatch with the Mg matrix. This mismatch can lead to the strain fields around monolayer GP zones and further interact with the dislocations. Therefore, the lattice parameters are important information required by the continuum mechanical model to predict the strengthening effect of the strain field.

There are three types of ternary GP zones predicted in the last section. Here we show the calculated lattice parameters of them from DFT calculations. Due to the limit size of DFT cells, the interspacing between two monolayer GP zones is limited, which will inevitably cause some interactions between the two precipitates and affect the lattice parameters. Additionally, the relaxation scheme will directly affect the atomic motion in DFT calculations. Therefore, we tested how the parameters change with 1) the interspacing of two GP zones due to periodic boundaries, 2) the relaxation scheme.

GP zone of MgZnCa

Table 4.2 The lattice parameters calculated in DFT under two relaxation schemes and 5 types of spacing between two monolayer GP zones along the $[0001]_{\alpha}$ direction.

DFT Cell size	full relaxation		Atomic position relaxation	
	a/nm	c/nm	a/nm	c/nm
c_{Mg} (1 Mg layers)	0.598 (CaCu5-type Laves phase)	0.476(CaCu5-type Laves phase)	0.553	0.519
$2c_{\mathrm{Mg}}$(3 Mg layers)	0.554	1.049	0.553	1.037
$3c_{\mathrm{Mg}}$(5 Mg layer)	0.553	1.569	0.553	1.554
$4c_{\mathrm{Mg}}$(7 Mg layer)	0.553	2.088	0.553	2.072
$5c_{\mathrm{Mg}}$(9 Mg layer)	0.553	2.605	0.553	2.590

GP zone of $Mg_4Zn_2Ca_3$

Table 4.3 The lattice parameters calculated in DFT under two relaxation schemes and 5 types of spacing between two monolayer GP zones along the $[0001]_{\alpha}$ direction.

DFT Cell size	full relaxation		Atomic position relaxation	
	a/nm	c/nm	a/nm	c/nm

c_{Mg}(1 Mg layer)	1.037(CaCu5-type Laves phase)	0.475(CaCu5-type Laves phase)	0.958	0.518
$2c_{\text{Mg}}$(3 Mg layers)	0.966	1.050	0.958	1.035
$3c_{\text{Mg}}$(5 Mg layer)	0.963	1.570	0.958	1.552
$4c_{\text{Mg}}$(7 Mg layer)	0.962	2.088	0.958	2.070
$5c_{\text{Mg}}$(9 Mg layer)	0.961	2.604	0.958	2.587

GP zone of Mg_5ZnCa_3

Table 4.4 The lattice parameters calculated in DFT under two relaxation schemes and 5 types of spacing between two monolayer GP zones along the $[0001]_{\alpha}$ direction.

DFT Cell size	**full relaxation**		**Atomic position relaxation**	
	a/nm	c/nm	a/nm	c/nm
c_{Mg}(1 Mg layers)	1.040 (CaCu5-type Laves phase)	0.485(CaCu5-type Laves phase)	0.958	0.518
$2c_{\text{Mg}}$(3 Mg layers)	0.972	1.052	0.958	1.035
$3c_{\text{Mg}}$(5 Mg layers)	0.967	1.572	0.958	1.552
$4c_{\text{Mg}}$(7 Mg layer)	0.964	2.090	0.958	2.070
$5c_{\text{Mg}}$(9 Mg layers)	0.964	2.606	0.958	2.587

As shown in the **Tables 4.2-4.4**, all the three types of GP zones have larger parameters than those of Mg matrix, which means GP zones will push Mg in the matrix away and cause a compressed region around them. In the DFT calculations, with the increasing concentration of Zn in GP zones, its lattice parameters decrease. This is reasonable, considering the small size of Zn atoms compared with Mg and Ca atoms. For cases with increasing Mg layers between GP zones due to periodic boundaries, it can be seen that more Mg buffer layers in DFT cells lead to larger lattice parameters of c along the $[0001]_\alpha$ direction, but have relatively very small effect on the lattice parameter of a within the basal plane. This trend is also reasonable, since the two GP zone plates will push against each other and compress each other along the c direction. On the other hand, the increase of DFT cell along c direction doesn’t affect the case on the plane perpendicular to it. For the two different relaxation schemes, the lattice parameters under the full relaxation are generally larger than those under the relaxation of atomic positions. With the increasing buffer Mg layer along c, the c parameters under atomic position relaxations approach the one under full relaxations, which means full relaxation are more reasonable when focusing on the lattice parameter. Because in experiments, the distance between GP zones can be much larger than the case in DFT calculations.

4.5 Displacement fields around GP zones in Mg-Zn-Ca

As the trend shown in the last section, the size mismatch between GP zones and the Mg matrix decreases with the increasing Zn in the GP zones based on the difference of lattice parameters. Therefore, to better shown the displacement fields around GP zones in the Mg-Zn-Ca system, we use the GP zones Mg2Ca to calculate the trend of the fields on both the basal plane and also in the Mg matrix along c direction.

Displacements of GP zone Mg_2Ca

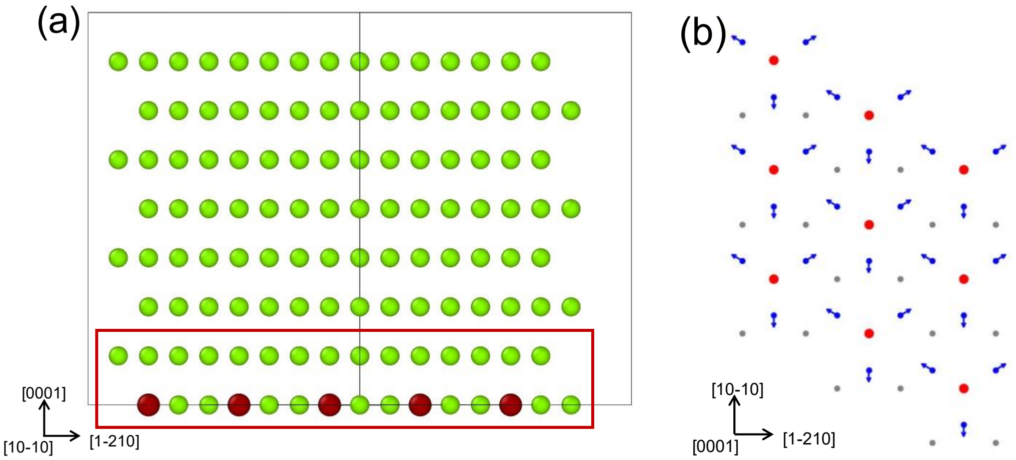

Fig. 4.6 (a) The DFT cell with the atoms shown in the left figure marked by red box; **(b)** the displacements of atoms on the basal plane.

The DFT cells used to calculate the displacement of atoms includes 7 Mg buffer layers to avoid the interaction between GP zones due to the periodic boundaries, as shown in the **Fig. 4.6(a)**. The displacement of atoms relative to the atoms on the HCP lattice sites are shown in Fig. 4.6(b), where Ca atoms are colored by red and Mg atoms are colored by blue. The Mg atoms in the neighboring layer are also shown in grey. As shown, the big Ca atoms don't move and push away

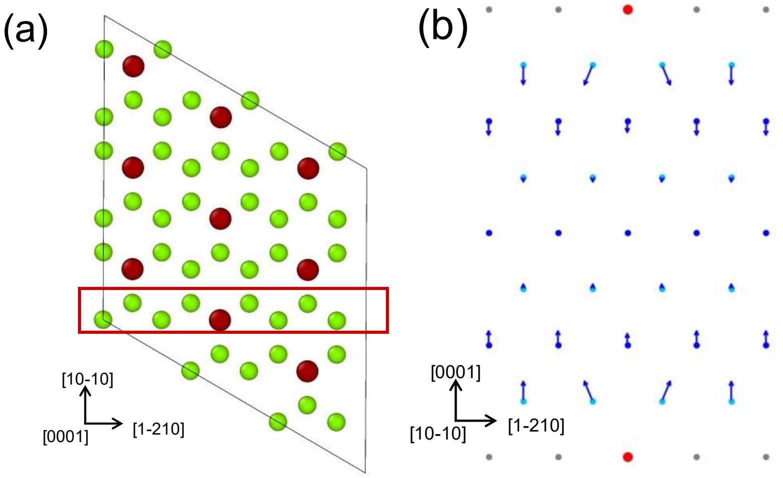

Fig. 4.7 (a) The DFT cell with the atoms shown in the left figure marked by red box; **(b)** the displacements of atoms on the prismatic plane.

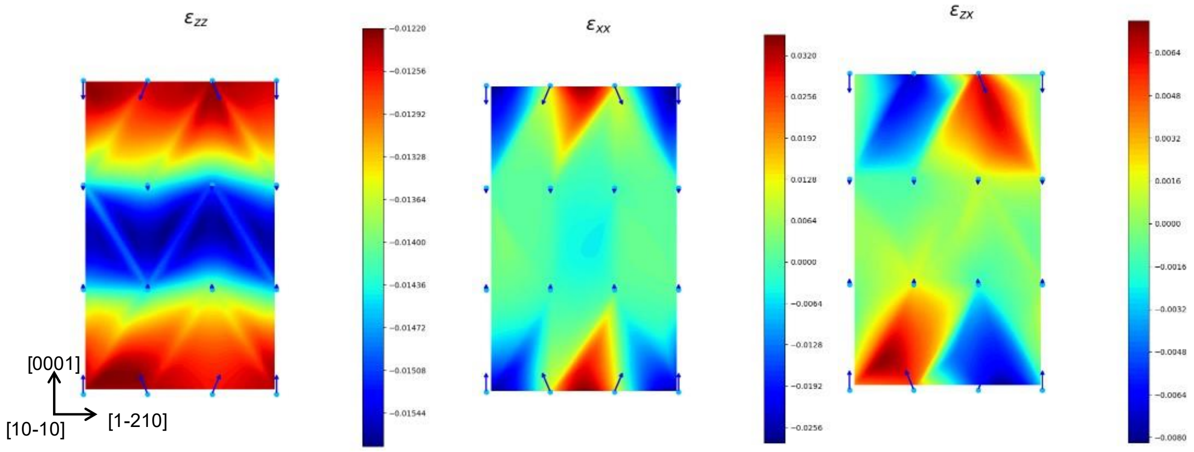

Fig. 4.8 The strain field in between the two GP zones on the top and bottom of the figures.

the small Zn atoms round them. Zn atoms moves direct towards the far neighboring Ca atoms due to the symmetry. The displacements of atoms in Mg matrix along c direction are shown in **Fig. 4.7**. To better show the trend, disclaimants are 10 times larger than their real value. The atoms in the Mg matrix are pushed away from the GP zones along c, and approach zero due to the symmetry of the cell along this direction. The displacements cancel out for atoms in the middle of the two GP zones. According to the displacements, the strain field, which is the first derivative of displacements with respect to the positions, are shown for the prismatic plane in **Fig. 4.8**. It is seen that Ca push away Mg atoms and Zn atoms attract Mg atoms, which is consistent with the size difference of the three elements.

Displacements of Mg in matrix due to GP zones

The strain field around GP zones is what interacts with dislocations. Since the displacements along c is more significant than them along other directions, we only focus on the former for the four types of GP zones predicted in the chapter. Previously, it is shown that lattice paraments c decrease with increase of Zn in the monolayer GP zones. In **Fig. 4.9**, we show in detail how the displacements of Mg atoms between the two GP zones changes with different type of GP zones and the position of the layer in the 7 Mg buffer layers. Different type of GP zones are marked with different colors. It is shown that the scale of displacement is consistent with the lattice parameter of GP zones. With the increase of Zn atoms in the monolayer GP zone, the displacement along *c* decrease for atoms at all buffer layers. For each type of GP zone, the displacement decreases with position of atoms farer from the GP zone. But due to the periodic boundary, the displacements cancel out in the middle of the two GP zones.

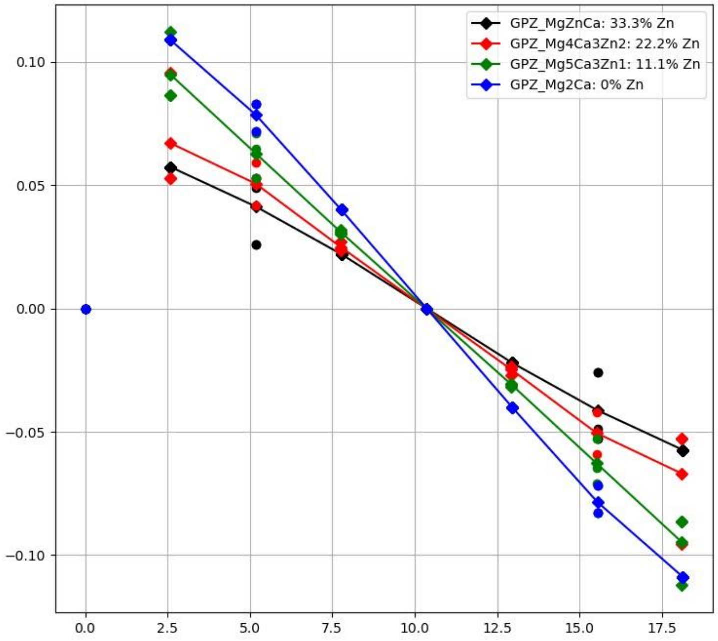

Fig. 4.9 The displacements along the *c* direction of Mg atoms in each of the 7 buffer layers between two GP zones.

References

[1] D.H. Ping, K. Hono, J.F. Nie, Atom probe characterization of plate-like precipitates in a Mg-RE-Zn-Zr casting alloy, *Scr. Mater.* 48 (2003) 1017–1022.

[2] T.J. Pike, B. Noble, The formation and structure of precipitates in a dilute magnesium-neodymium alloy, *J. Less-Common Met.* 30 (1973) 63–74.

[3] J.F. Nie, Precipitation and hardening in magnesium alloys, *Metall. Mater. Trans. A Phys. Metall. Mater. Sci.* 43A (2012) 3891–3939.

[4] C.J. Bettles, M.S. Dargusch, Creep and Bolt-load Retention of Sand Cast Elektron MEZ, WILEY-VCH Verlag Gmbh, Weinheim, Germany, 2000, Magnesium alloys and their applications.

[5] K. Oh-ishi, R. Watanabe, C.L. Mendis, K. Hono, Age-hardening response of Mg-0.3 at.%Ca alloys with different Zn contents, *Mater. Sci. Eng. A.* 526 (2009) 177–184.

[6] C.L. Mendis, C.J. Bettles, M.A. Gibson, S. Gorsse, C.R. Hutchinson, Refinement of precipitate distributions in an age-hardenable Mg-Sn alloy through microalloying, *Philos. Mag. Lett.* 86 (2006) 443–456.

[7] C.L. Mendis, C.J. Bettles, M. a. Gibson, C.R. Hutchinson, An enhanced age hardening response in Mg–Sn based alloys containing Zn, *Mater. Sci. Eng. A.* 435–436 (2006) 163–171.

[8] J.B. Clark, Transmission electron microscopy study of age hardening in a Mg-5 wt.% Zn alloy, *Acta Metall.* 13 (1965) 1281–1289.

[9] J.B. Clark, Age hardening in a Mg-9 wt.% Al alloy, *Acta Metall.* 16 (1968) 141–152.

[10] J.F. Nie, K. Oh-ishi, X. Gao, K. Hono, Solute segregation and precipitation in a creep-resistant Mg-Gd-Zn alloy, *Acta Mater.* 56 (2008) 6061–6076.

[11] J.C. Oh, T. Ohkubo, T. Mukai, K. Hono, TEM and 3DAP characterization of an age-hardened Mg-Ca-Zn alloy, *Scr. Mater.* 53 (2005) 675–679.

[12] X. Gao, S.M. Zhu, B.C. Muddle, J.F. Nie, Precipitation-hardened Mg-Ca-Zn alloys with superior creep resistance, *Scr. Mater.* 53 (2005) 1321–1326.

[13] Z.H. Li, T.T. Sasaki, K. Hono, Unpublished work, (2022).

[14] A. van de Walle, G. Ceder, Automating first-principles phase diagram calculations, *J. Phase Equilibria*. 23 (2002) 348–359.

[15] G. Kresse, Efficient iterative schemes for ab initio total-energy calculations using a plane-wave basis set, *Phys. Rev. B*. 54 (1996) 11169–11186.

[16] M. Methfessel, A.T. Paxton, High-precision sampling for Brillouin-zone integration in metals, *Phys. Rev. B*. 40 (1989) 3616–3621.

[17] K. Wang, D. Cheng, C. Fu, B. Zhou, First-principles investigation of the phase stability and early stages of precipitation in Mg-Sn alloys, *Phys. Rev. Mater.* 013606 (2020) 1–13.

[18] C. Ravi, C. Wolverton, First-principles study of crystal structure and stability of Al-Mg-Si-(Cu) precipitates, *Acta Mater.* 52 (2004) 4213–4227.

[19] D. Wang, M. Amsler, V.I. Hegde, J.E. Saal, A. Issa, B.C. Zhou, X. Zeng, C. Wolverton, Crystal structure, energetics, and phase stability of strengthening precipitates in Mg alloys: A first-principles study, *Acta Mater.* 158 (2018) 65–78.

[20] J. Madsen, T. Susi, The abTEM code: transmission electron microscopy from first principles, *Open Res. Eur.* 1 (2021) 24.

[21] J. Laursen, J. Staun Olsen, Temperature dependence of the Debye–Waller factor for magnesium measured by energy-dispersive diffractometry, *Acta Crystallogr. Sect. A*. 35 (1979) 482–484.

[22] C. Ophus, A fast image simulation algorithm for scanning transmission electron microscopy, *Adv. Struct. Chem. Imaging*. 3 (2017) 1–11.

Chapter 5 is the calculation part of the submitted paper to Acta Mater.: Z.H. Li*, D. Cheng*, K. Wang, E. R. Hoglund, J. M. Howe, B.C. Zhou, T.T. Sasaki, T. Ohkubo, K. Hono. “Revisit of precipitation process in dilute Mg-0.3Ca-0.6Zn alloy” (*equally contributions). In this paper, Z.H. Li, T.T. Sasaki, T. Ohkubo, and K. Hono contributes to the experimental part. For the calculation part, D. Cheng proposed the atomic structures for precipitates, performed the DFT calculations, and draft the corresponding part of manuscript under the supervision of K. Wang and B.C. Zhou. Z.H. Li generated the simulated STEM and SAED images. E. R. Hoglund and J. M. Howe analyzed the results of simulated TEM images. All authors reviewed and contributed to the final manuscript.

Chapter 5 Precipitates in the Mg-0.6Zn-0.3Ca alloy

5.1 Introduction

Broad interests in lightweight magnesium (Mg) alloys have been provoked by the compelling weight-saving demand in the transportation and medical sectors [1,2]. Among recently developed Mg alloys, heat-treatable Mg-Ca-Zn alloys are potential candidates for various applications, including structural and biomedical applications, etc. [3-9]. The rapid age-hardenability of Mg-Ca-Zn dilute alloys leads to good combinations of extrudability and strength in extrusions and formability and strength in sheets that have never been achieved in commercial Mg alloys [3-6]. The precipitation-hardened Mg-Ca-Zn alloys also exhibit good creep resistance and biocompatibility [6-9]. While the wrought alloys are used in under-aged or peak-aged conditions to gain as high precipitation-strengthening effect as possible [5], the creep-resistant ones are over-aged at elevated temperatures [7], and the precipitate distribution significantly affects the degradation behavior in the biodegradable alloys [8,9]. Therefore, an in-depth understanding of the whole precipitation process in the Mg-Ca-Zn alloy is crucial to correlate the microstructure with properties, providing guidelines for further improvements of in-service performance.

The precipitation sequence in the Mg-Ca-Zn alloy is proposed in the literature as follows [10]:

$$\text{SSSS} \rightarrow \alpha\text{-Mg} + \text{ordered Guinier Preston (G.P.) zones} \rightarrow \alpha\text{-Mg} + \eta' \rightarrow \alpha\text{-Mg} + \eta$$

In previous experimental studies [4,6,11-14], the G.P. zone was suggested to be a monolayer precipitate (hexagonal, a = 0.56 nm) forming on the $(0002)_\alpha$ plane of the Mg matrix with Ca or Zn atoms six-fold coordinated by Mg atoms while specific configurations of Ca and Zn were not detailed. A recent density functional theory (DFT) study considered detailed configurations of Ca and Zn and suggested several structures consistent with experimentally reported diffraction patterns and STEM images [15]. In the suggested structures, Ca atoms are six-fold coordinated by Mg or Zn atoms in the monolayer G.P. zones, and the most stable one is consistent with the measured Ca/Zn ratio (i.e., ~ 1:1 [4,6]). However, the structure and composition of the metastable η' and equilibrium η phases are still under debate. The η' phase is a thin plate-like precipitate forming on the $(0002)_\alpha$ planes with a hexagonal structure ($P6_3/mmc$, a = 0.56 nm, c =1.04 nm) in Mg-0.6Ca-0.4Zn (at.%) alloy [16], while Oh-ishi *et al.*, reported the one have a similar monolayer structure to that of the G.P. zone in Mg-0.3Ca-0.6Zn (at.%) alloy [13]. In addition, the η' single plates gradually form in plate pairs during over-aging [12]. Since such precipitate microstructure evolution is similar to that of γ'' phase in the Mg-RE-Zn (RE: Y or Gd) alloys, a more complicated precipitation sequence may be expected in the Mg-Ca-Zn dilute alloy like the following one, which is well established in the Mg-RE-Zn alloys [17-20];

SSSS → α-Mg + ordered G.P. zones → α-Mg + γ'' → α-Mg + γ' → α-Mg + γ + δ

Different structures and compositions have been also reported for the equilibrium η phase depending on the alloy compositions. The η phase is a Mg_2Ca structure type phase with a hexagonal structure ($P6_3/mmc$, a =0.62 nm, c =1.01 nm) in Mg-0.6Ca-0.4Zn (at.%) alloy, and has different orientation relationships (ORs) depending on the shape as listed in Table 1. However, a trigonal structure ($P\bar{3}1c$, a = 0.97 nm, c =1.01 nm) with a chemical composition of $Ca_2Mg_6Zn_3$ was reported for the η phase in Mg-1Ca-2.3Zn (at.%) alloy [21,22]. More recently, Schäublin *et al.* analyzed the precipitates formed in an as-extruded Mg-0.2Ca-0.6Zn alloy and concluded that the structure of the ternary phase is hexagonal ($P6_3/mmc$, a = 0.96 nm, c =1.00 nm) with a composition close to $Ca_2Mg_5Zn_5$ or $Ca_3Mg_{11}Zn_4$. [23-25].

Mg-0.3Ca-0.6Zn (at.%) alloy exhibits the largest age-hardening among the precipitation hardenable Mg-Ca-Zn alloys [13]. Therefore, the exploration of atomic structures of the precipitates in this particular alloy would provide a basis for the further determination of physical properties of each kind of precipitates and design the desired microstructures in Mg-Ca-Zn dilute alloys [26]. In this Chapter, we thoroughly analyzed the atomic structures of precipitates formed in Mg-0.3Ca-0.6Zn (at%) alloy during artificial aging at 200 °C which is close to the aging temperature for wrought alloys and service temperature for creep-resistant ones. The atomic structures of metastable η'', η', η_1 phases and equilibrium η phase are deduced, which are not only thermodynamically stable based on first-principles calculations, but also fulfill the structural and compositional information from STEM and 3D-APT measurements. The phase stability of each precipitate type in first-principles calculations provides the thermodynamic rationale for the precipitation sequence.

5.2 Computational Methods

The atomic structures of precipitates were determined based on symmetry from diffraction pattern, composition from 3D-APT analysis, contrast from STEM and thermodynamic stability from first-principles calculations. For a given structural template, numerous unique atomic structures exist depending on the atomic decoration of the lattice sites in the template. Based on the prototypical template from experiments, all the ordered structures are enumerated with the size of unit cell determined by diffraction pattern and STEM images. The experimentally measured symmetry, compositions and SAED patterns were used to screen the atomic structures. For the disordered or partially disordered structures, the random distribution of solutes on the structural template is modeled using the special quasi-random structures (SQS) [27,28], where the correlation between solutes in a small cell mimics the completely random distribution of solutes in an infinitely large supercell. The Alloy Theoretic Automated Toolkit (ATAT) is used to enumerate ordered structures and build SQS [29]. When optimizing the correlations between solutes in SQS, the cut-off distances for pair, triplet and quadruplet clusters were at least 9.91, 6.39 and 5.54’ .

After the candidate structures were chosen, first-principles electronic structure methods based on density functional theory (DFT) were performed to optimize the structures and calculate their formation energies [30,31]. The ion-electron interaction was described by the projector augmented plane-wave method [32] and the exchange-correlation functional was described by an improved general gradient approximation of Perdew-Burke-Ernzerhof [33], as implemented in the Vienna ab initio simulation package (VASP, version 5.4) [34,35]. The detailed DFT settings and the methods for stability analysis can be found in our previous work [15]. In addition to agreeing with the symmetry and composition from experiments, a candidate structure is chosen only if it does not collapse during structural optimization (*i.e.*, mechanical stability) and has negative formation energy (*i.e.*, thermodynamic stability) with respect to pure metals. Note that formation energies per solute are used to compare the relative stabilities of precipitates in different compositions and reflect the changing chemical potential of the observed precipitates during the aging process [36,37]. In DFT calculations, the atomic positions were allowed to relax while the cell shape and volume were fixed for the early-stage precipitates (*i.e.*, η' and η'') to mimic the constraint from the Mg matrix. Meanwhile, all degrees of freedom were relaxed for the precipitates with bulk structures (i.e., η_1 and η).

To prove the validity of the proposed structures for the observed precipitates, the HAADF STEM images and diffraction patterns were simulated and compared with the experimental results. The STEM images were simulated by xHREM. The simulated diffraction patterns were performed using the software Crystal Maker [48]. For the HAADF STEM simulations, the aperture radius of 11.9 mrad, spherical aberration Cs of 0.5mm, and center defocus of 354 Å were used for the optical parameters. The bright field of 11.9 mrad and annular dark field of 56 mrad were used for detector parameters. For tri-layer phases of η'' and η', supercells were created with the tri-layer plates extending infinitely on the basal plane and embedded in the Mg matrix along c direction. The size of the supercells along c is around 21 Å. For the bulk structures of η_1 and η, the unit cells with periodic boundaries were used during simulations.

5.3 Computational Results based on Experiments

In this Chapter, an in-depth analysis is reported to clarify the structures of precipitates formed in the Mg-0.3Ca-0.6Zn alloy during isothermal aging at 200 °C. The atomic structures for the observed metastable η'', η', η_1 phases and equilibrium η phase are proposed based on the structural and compositional information in HAADF-STEM and 3D-APT. The proposed structures were validated by their stabilities in DFT calculations, and the simulated STEM and SAED patterns. In the calculations, It is found that there are usually several structures for each phase with the same structural template and similar formation energies but slightly different site occupations on the template (hence fluctuations in overall composition). The ones that best match the experimental observations are chosen as the final candidates in the current work. The relative

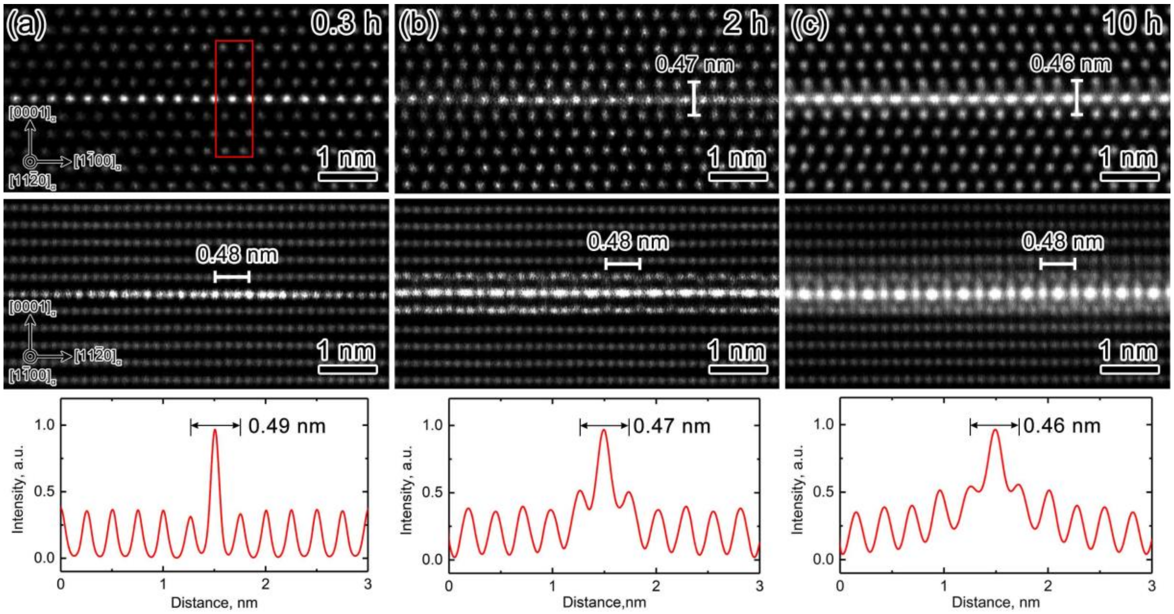

Fig. 5.1 Atomic-resolution HAADF-STEM images and intensity profiles measured across the nanoscale precipitates observed in (a) 0.3 h, (b) 2 h, (d) 10 h at 200 °C. Note that the images on the upper and middle row are taken from the zone axes of $[11\bar{2}0]_\alpha$ and $[1\bar{1}00]_\alpha$, respectively.

stabilities of the proposed structures of the precipitates in DFT provide the thermodynamic reasoning behind the observed precipitation sequence in the current experiments:

$$\text{S.S.S.S} \rightarrow \text{G.P. zones} \rightarrow \eta'' \rightarrow \eta' \rightarrow \eta' \text{ pairs and stacks} / \eta_1 \rightarrow \eta.$$

Fig. 5.1a through c show atomic-resolution HAADF-STEM images of the nanoscale precipitates in the 0.3 h, 2 h, and 10 h aged samples at 200 °C, respectively. The ordered G.P. zone in the 0.3 h-aged sample is a monolayer plate, **Fig. 3a**. The $[11\bar{2}0]_\alpha$ image shows bright columns containing either Ca or Zn arranged closely on a single $(0002)_\alpha$ plane, while a periodical arrangement of Zn/Ca-rich columns with an interval of every two columns are observed along the $[1\bar{1}00]_\alpha$. This observation is consistent with the simulated HADDF-STEM image of the predicted GP zones in Mg-Zn-Ca alloys in Chapter 4. After aging for 2 h, the monolayer G.P. zones within the sample transform into tri-atomic-layer plates designated as the η'' phase, **Fig. 5.1b**. The middle layer of the η'' shows the brightest contrast from the $[11\bar{2}0]_\alpha$, indicating a strong Zn enrichment compared to the two side layers. The $[1\bar{1}00]_\alpha$ image shows a similar atomic arrangement for all three layers with a periodicity of every two brighter columns separated by one dark column. The plate-like precipitates in the 10 h-aged sample are also tri-atomic-layer ones forming on the $(0002)_\alpha$ planes, **Fig. 5.1c**. Unlike the η'' phase, the atomic positions in the brightly imaged middle layer shift by a distance of $\sqrt{3}/6$ along each $[1\bar{1}00]_\alpha$ direction, allowing them to designate as the η' phase. The η'' and η' are similar to those in HAADF-STEM images of γ'' precipitates in Mg-RE-Zn alloys, *i.e.*, tri-layer structures consisting of two undulating side layers and a middle layer [11, 18,38-39]. Therefore, the atomic structures of the η'' and η' phases are constructed based on the reported structural template for γ'' precipitate [40].

Fig. 5.2 shows atomic models, simulated STEM images, and diffraction patterns of η'' phase embedded in the Mg matrix along the $[1\bar{1}00]_\alpha$ and $[11\bar{2}0]_\alpha$ directions. This phase is proposed to be $Mg_5Ca_2Zn_2$ with the Zn/Ca ratio of 1:1. Note that this Zn/Ca ratio approximates the statistical average of the composition fluctuation observed in 3D-APT. In this tri-layer phase, the two side layers have an ordered pattern with Ca atoms six-folded coordinated by Mg atoms on the basal plane, where some Ca are randomly replaced by Mg with the Ca/Mg ratio of ~ 3:1 and some Mg atoms are replaced by Zn with the Mg/Zn of ~3:1, **Fig. 5.2a**. The Ca/Mg and Mg/Zn ratios are proposed according to the atomic column intensities in the two side layers in the experimental STEM image, **Fig. 5.1b**. The Mg-rich columns in the side layers of η'' are slightly brighter than the Mg columns in the matrix, which indicates some solutes are in these Mg-rich columns in the side layers. In our previous analysis of G.P. zones in Chapter 4, we found that Zn

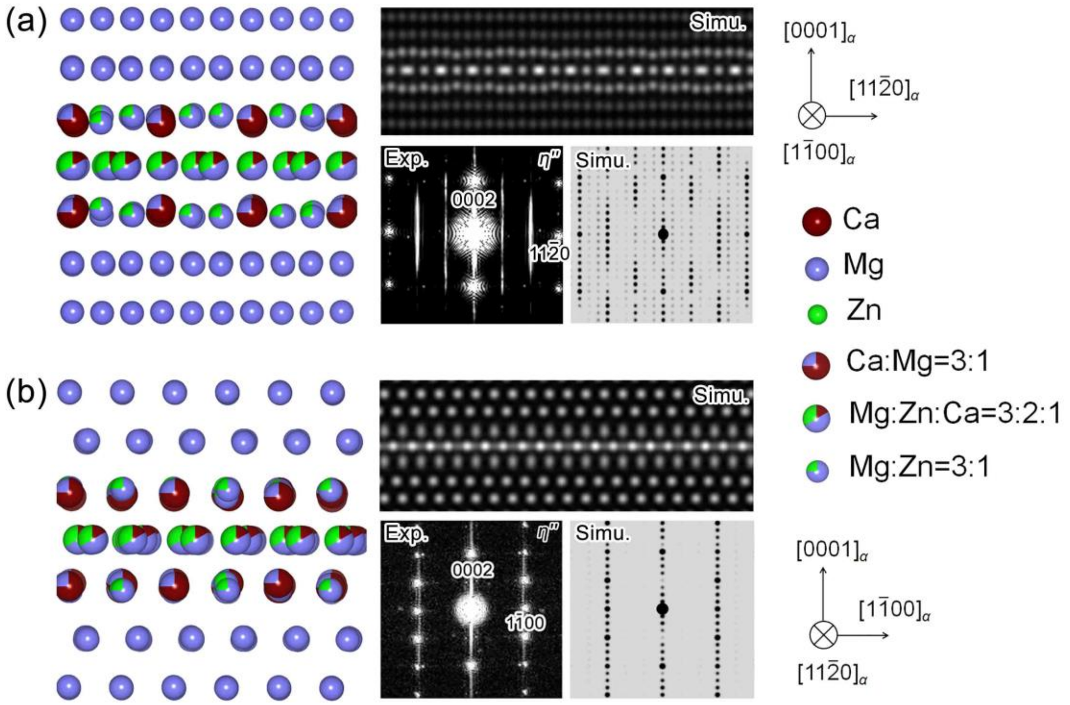

Fig. 5.2 The proposed atomic models, simulated STEM images, and diffraction patterns of the η'' phase embedded in Mg matrix viewed along the (a) $[1\bar{1}00]_\alpha$ and (b) $[11\bar{2}0]_\alpha$ directions.

atoms are favored compared with Ca atoms on the Mg-rich columns along $[1\bar{1}00]_\alpha$. Considering the similarity between G.P. zones and the side layers in η'', some Mg atoms in the Mg-rich columns of the side layer of η'' are replaced with Zn. Furthermore, Ca-rich columns in the side layers are dimmer than or equally bright to the Mg-rich columns, indicating atoms with a smaller atomic number are on these sites. The ordered pattern on the two side layers of the η'' corresponds to the streaks of the 1/3 and 2/3 $[11\bar{2}0]_\alpha$ on the experimental $[1\bar{1}00]_\alpha$ diffraction pattern, **Fig. 5.2a**. The middle layer contains Mg, Ca and Zn atoms distributed randomly with a ratio of 3:2:1 (mixed atomic symbols) with two columns closer to each other within each periodicity viewed along the $[1\bar{1}00]_\alpha$. The randomness of the atom species on the middle layer corresponds to the lack of fractional indexed ordered streaks in the experimental $[11\bar{2}0]_\alpha$ diffraction pattern, **Fig. 5.2b**. DFT calculations show that the two columns close to each other within a period can be stable instead of merging into one in the η' phase only when Ca atoms are in the middle layer, **Fig. 5.1c**.

Based on the proposed atomic model of the η'' phase, four DFT supercells with different configurations are built by SQS following the elemental ratio on each mixed site. The four supercells show mechanical and thermodynamic stabilities after structural relaxations using DFT with close formation energies. Two of the supercells after relaxation are shown along $[11\bar{2}0]_\alpha$ and

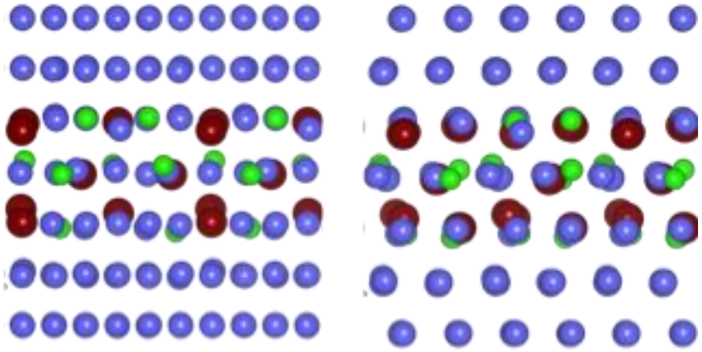

Fig. 5.3 A supercell from SQS based on the proposed atomic models of the η'' phase after relaxations view along $[1\bar{1}00]_\alpha$ and $[11\bar{2}0]_\alpha$ directions.

$[1\bar{1}00]_\alpha$ directions in **Fig. 5.3**. As observed in the relaxed structures, the positions of atoms within the tri-layer η'' phase after relaxation in DFT is sensitive to the specific configurations of elements on those mixed sites. Therefore, the one captured in **Fig. 5.1b** may have configurations different from those in the two exhibited examples and correspondingly slightly different atomic positions of the mixed sites. In addition to the stability, the proposed mixed atomic model is further validated by the well-matched intensities of atomic columns between experimental and simulated STEM images and the matched diffraction patterns. Note that the experimentally measured Zn/Ca ratio of the η'' varies within a small range. It is likely that the η'' phase could adopt a different Zn/Ca ratio because many similar structures of different compositions with low formation energies per solute are also found in our DFT calculations.

Fig. 5.4 shows the proposed atomic structure of the η' phase embedded in the Mg matrix along the $[1\bar{1}00]_\alpha$ and $[11\bar{2}0]_\alpha$ directions. This phase is proposed to be $Mg_4Ca_2Zn_3$ ($P\bar{6}2m$, a = 0.55 nm and c = 0.49 nm) with the Zn/Ca ratio of 3:2. Compared to the η'' phase, the two side layers of the tri-layer η' also have an ordered pattern with Ca atoms six-folded coordinated by Mg atoms on the basal plane but with no mixed atoms. Because the atomic intensities of the Mg columns in the side layers are the same as those of Mg columns in the matrix in the experimental $[1\bar{1}00]_\alpha$ STEM images, **Fig. 5.1c**, which indicates few solutes in the Mg columns. Additionally, the intensities of Ca columns are stronger than those of Mg columns in the matrix, **Fig. 5.1c**, which is different from the case in η'', i.e., Ca-rich columns having equal or dimmer intensities than Mg columns in the matrix, **Fig. 5.1b**. The ordered pattern on the two side layers of the η' corresponds to the streaks of the 1/3 and 2/3 $[11\bar{2}0]_\alpha$ on the experimental $[1\bar{1}00]_\alpha$ diffraction pattern, **Fig. 5.4a**. The middle layer of the tri-layer η' only consists of pure Zn atoms, which corresponds to the lack of fractional indexed ordered streaks in the experimental $[11\bar{2}0]_\alpha$ diffraction pattern, **Fig. 5.4b**.

Based on the proposed atomic structure in **Fig. 5.4**, the DFT supercell is built, and the cell shows mechanical and thermodynamic stabilities after structural relaxations using DFT. Furthermore, the simulated STEM images and diffraction patterns of the proposed η' phase agree with the experimental ones, which further confirms the validity of the proposed structure. Compared with the η'' phase, the η' phase shows a more ordered structure with an increased concentration of Zn, which means the partially ordered η'' phase can be a structural precursor for the ordered η' phase.

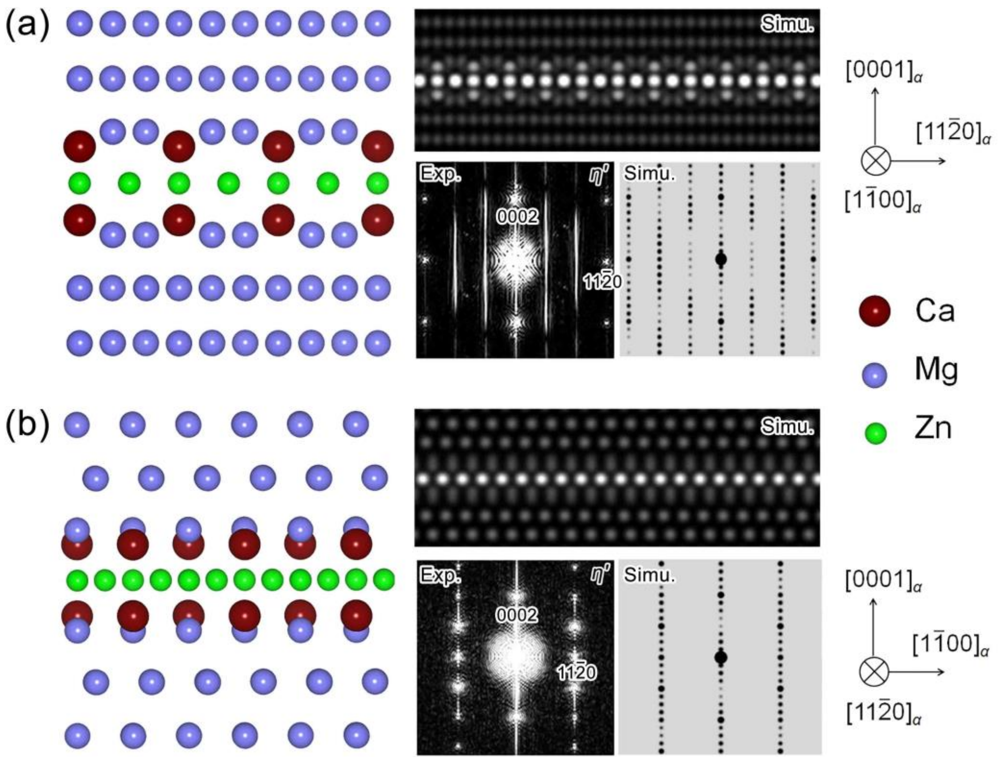

Fig. 5.4 The proposed atomic models, simulated STEM images, and diffraction patterns of the η' phase embedded in Mg matrix viewed along the (a) $[1\bar{1}00]_\alpha$ and (b) $[11\bar{2}0]_\alpha$ directions.

After prolonged aging to 100 h, the η' plates tend to form in pairs followed by stacks with the interplanar spacing mostly concentrated in 5 α-Mg layers. **Figs. 5.5a through d** show an atomic-resolution HAADF-STEM image of the precipitates obtained from the 100 h- and 300 h-aged samples. A η' plate pair composed of two single η' plates are observed from the $[11\bar{2}0]_{\alpha}$ and $[1\bar{1}00]_{\alpha}$ zone axes with an interplanar spacing of ~five α-Mg layers, **Figs. 5.5a and b**. Further aging to 300 h leads to the precipitation of the other two η' plates to form the η' plate stack,

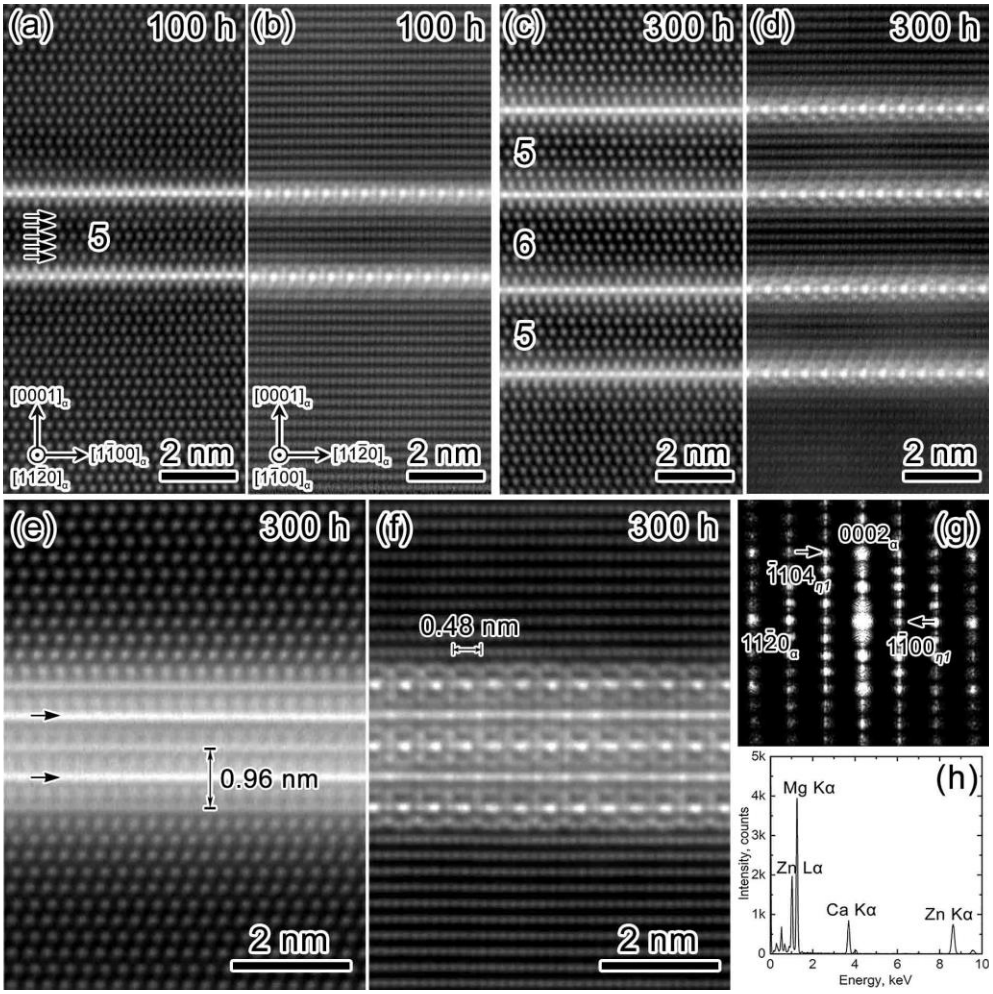

Fig. 5.5 Atomic-resolution HAADF-STEM images of the (a,b) η' plate pair seen in 100 h-aged sample and (c,d) η' plate stack seen in 300 h-aged sample, respectively. (e,f) is a part of η_1 phase precipitate observed in 300 h-aged sample. (g) and (h) are the FFT pattern and EDX spectrum obtained from the η_1 phase, respectively. Note that (a,c,e) and (b,d,f) are taken from the zone axes of $[11\bar{2}0]_{\alpha}$ and $[1\bar{1}00]_{\alpha}$, respectively.

and the number of the α-Mg layer between neighboring η' plates is five in most of the cases, **Figs. 5.5c and d**. Therefore, to explain the thermodynamic origin behind that regular spacing between η' plates, DFT calculations encoding both strain and interfacial free energies is done.

Based on the atomic structure of η' phase ($Mg_4Ca_2Zn_3$), we build a supercell with two tri-layer η' plates separated by 1 to 7 Mg layers within the Mg matrix of 30 atomic layers along the $[0001]_\alpha$, **Fig. 5.6a**. The Mg layers in the matrix are used to separate the interaction between η' plates due to periodic boundaries in DFT calculations. As shown in **Fig. 5.6b**, the formation energy of the whole supercell decreases rapidly when the number of the separating Mg layers varies from 1 to 4, and gradually increases from 4 to 7. The system reaches the minimum energy when the number of the Mg layers is around 4, which is quite close to the experimental observations, **Figs. 5.5a-d**. That is similar to the case of the inter-plate distance of γ'' precipitates in Mg-6Y-2Ag-1Zn-0.6Zr (wt pct) alloy [18]. Therefore, the presence of 4-5 atomic layers of Mg is the most energetically stable when forming a plate pair of η' plates.

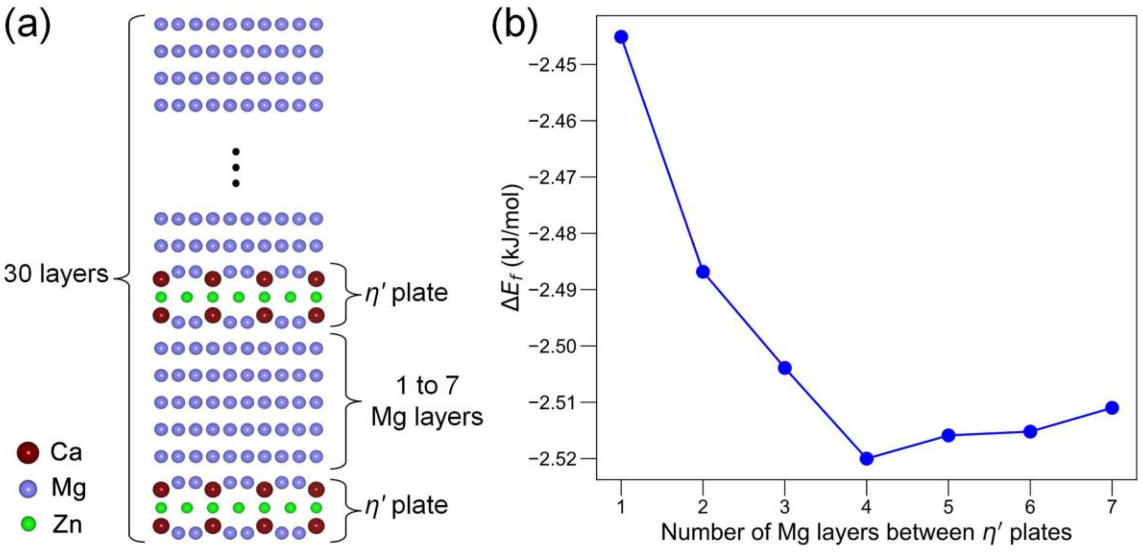

Fig. 5.6 (a) Schematic diagram of the supercell with various number of Mg layers between two η' plates along $[0001]_\alpha$ direction. (b) Variation of formation energy as a function of number of Mg layers.

In the 300 h-aged sample, Coarse η_1 plates heterogeneously formed in the matrix during over-aging. As shown in **Fig. 5.7,** a low-magnification bright field (BF)-TEM image of 300 h-aged Mg-0.3Ca-0.6Zn alloy obtained from the $[1\bar{1}00]_\alpha$ zone axis. Coarse lath and rod-like precipitates are clearly visible, meanwhile a few thin but very long platelets; ~ 400 ± 100 nm lie on the (0001) planes solely or link with coarse precipitates as indicated by arrows. Considering the board interface and uneven distribution in the matrix, the formation of η_1 plates may be facilitated by defects such as dislocations, which leads to the heterogeneously nucleation during the prolonged over-aging. The enlarged image of the dashed-line region shows that these coarse basal plates are much thicker than the η'' or η' plates with a much larger aspect ratio; length over thickness of ~ 150: 1, **Fig. 5.7b.** A similar long-period superlattice structure was reported for the $Mg_{17}Zn_3Yb_4$; $P\bar{6}2m$, a = 0.6 nm, c = 1.02 nm in a high-pressure synthesized $Mg_{97}Zn_1Yb_2$ alloy [47], while such η_1 thick plate, to our best knowledge, is firstly observed in the Mg-Ca-Zn alloys.

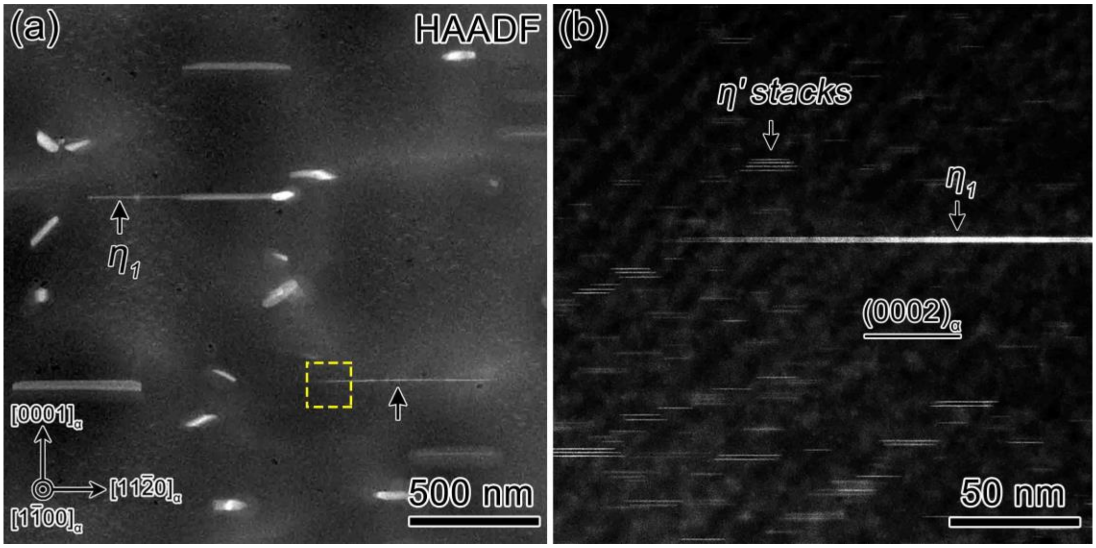

Fig. 5.7 (a) Low-magnification HAADF-STEM images obtained from the Mg-0.3Ca-0.6Zn alloy aged at 200 °C for 300 h. (b) Enlarged images of the region indicated by the dashed-line frame in (a). Note that the images were taken from the $[1\bar{1}00]_\alpha$ zone axis.

The higher magnification HAADF-STEM images show that η_1 phase looks like stacking η' plates with an inserted atomic layer enriched with Zn (and Ca) from $[11\bar{2}0]_\alpha$ and $[1\bar{1}00]_\alpha$ images, **Figs. 5.5e and f**. The corresponding FFT pattern along the $[1\bar{1}00]_\alpha$, **Fig. 5.5g**, shows that the $(0002)_\alpha$ and $(11\bar{2}0)_\alpha$ reflections are divided by three and two extra spots, respectively, indicating that the $d_{(0001)\eta1}$ and $d(1\bar{1}00)_{\eta1}$ are about four and $\sqrt{3}$ times that of $d_{(0002)_\alpha}$ and $d_{(11\bar{2}0)_\alpha}$. The unit cell height of the η_1 phase is measured to be ~ 0.96 nm. The standardless quantitative analysis from the EDX spectrum **(Fig. 5.5h)** indicates that the η_1 phase has an average composition of Mg-14.2±2Ca-

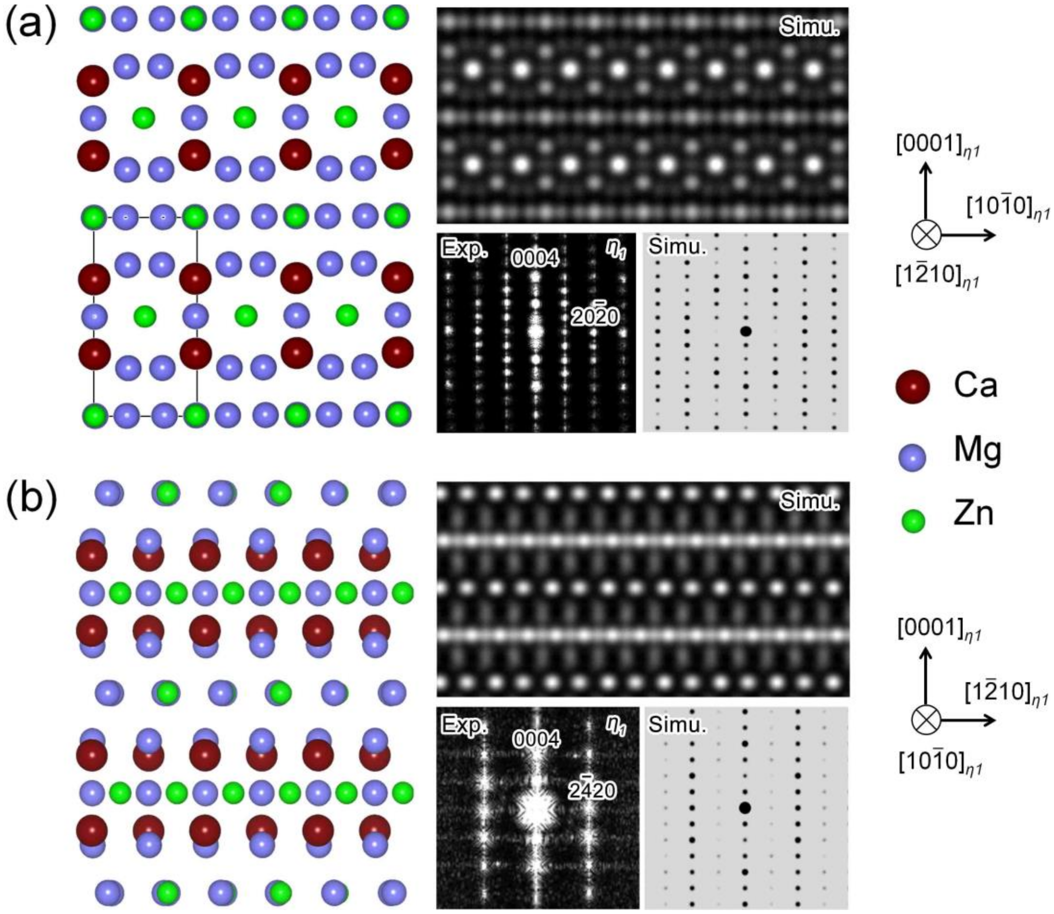

Fig. 5.8 The proposed atomic models, simulated STEM images, and diffraction patterns of the η_1 phase viewed along the (a) $[1\bar{2}10]_{\eta 1}$ and (b) $[10\bar{1}0]_{\eta 1}$ directions.

21.6±1Zn (at.%). The above results suggest that the η_1 phase has a hexagonal structure (P$\bar{6}$2m, a = 0.56 nm, c = 0.96 nm) with a Ca/Zn ratio remaining ~ 1.5.

Based on the experimental information and DFT calculations, $Mg_7Ca_2Zn_3$ (Pm, a = 0.57 nm, b = 2.26 nm, c = 0.97 nm, β = 120º) is proposed as the η_1 phase. The unit structure, as shown in **Fig. 5.8a and b**, contains 4 layers along the $[0001]_{\eta 1}$, including a tri-layer substructure like η''/η' and an additional layer of atoms concentrated with Zn and Mg atoms separating the tri-layer substructures. The separating layer has the same periodicity of three atomic columns on this plane, which agrees with the tri-layer substructure as shown in the experimental HAADF-STEM image along the $[1\bar{1}00]_\alpha$ direction, **Figure 5.5f.** Based on the intensities of atomic columns on the separating layer, the brightest spot within a periodicity correspond to the Zn-rich column with a Zn/Mg ratio of 1/1**,** and the two weak spots corresponds to two Mg-rich columns with a Zn/Mg ratio of 1/3. Within the tri-layer substructure, the two side layers are the same as that of η''/η', and the inner layer has a composition of $MgZn_2$, which leads to the overall composition of $Mg_7Ca_2Zn_3$ for the η_1 phase. Besides, the simulated patterns STEM and SAED patterns are also well consistent with the experimental ones, **Figs. 5.8a and b**. These results confirm the proposed structure for the η_1 phase.

In the 1000 h-aged sample, large bulk equilibrium precipitates of the η phase formed. Nanobeam electron diffraction (NBED) patterns were taken from different crystallographic directions to determine the crystal structure of the η phase, **Figures 5.9a through c**. Assuming the lattice parameters of the α-Mg matrix are a = 0.32 nm and c = 0.52 nm, these NBED patterns could be indexed based on a hexagonal structure with a = 1.00 nm and c = 1.01 nm. The point group and space group are provided as 6/mmm and $P6_3/mmc$, respectively, considering the symmetries and reflection conditions. (See **Table 5.1**, and **Table 5.2** for the detailed information) [44-46].

Therefore, the structure of the η phase (P6$_3$/mmc, a = 1.00 nm, c = 1.01 nm) is similar to that of the Ca$_2$Mg$_5$Zn$_5$ (P6$_3$/mmc, a = 0.96 nm, c = 1.00 nm), while the measured Mg/Zn ratio is lower than the reported one [25]. From the atomic resolution HAADF-STEM images of the η phase taken from the $[0001]_\eta$, $[11\bar{2}0]_\eta$, and $[1\bar{1}00]_\eta$ zone axes, respectively, the atomic columns with the brightest and weakest imaging contrast are supposed to be enriched with Zn and Mg, respectively, while the ones with dim contrast are considered as co-occupation by Zn/Mg (3:1), Mg/Zn (1:1), or

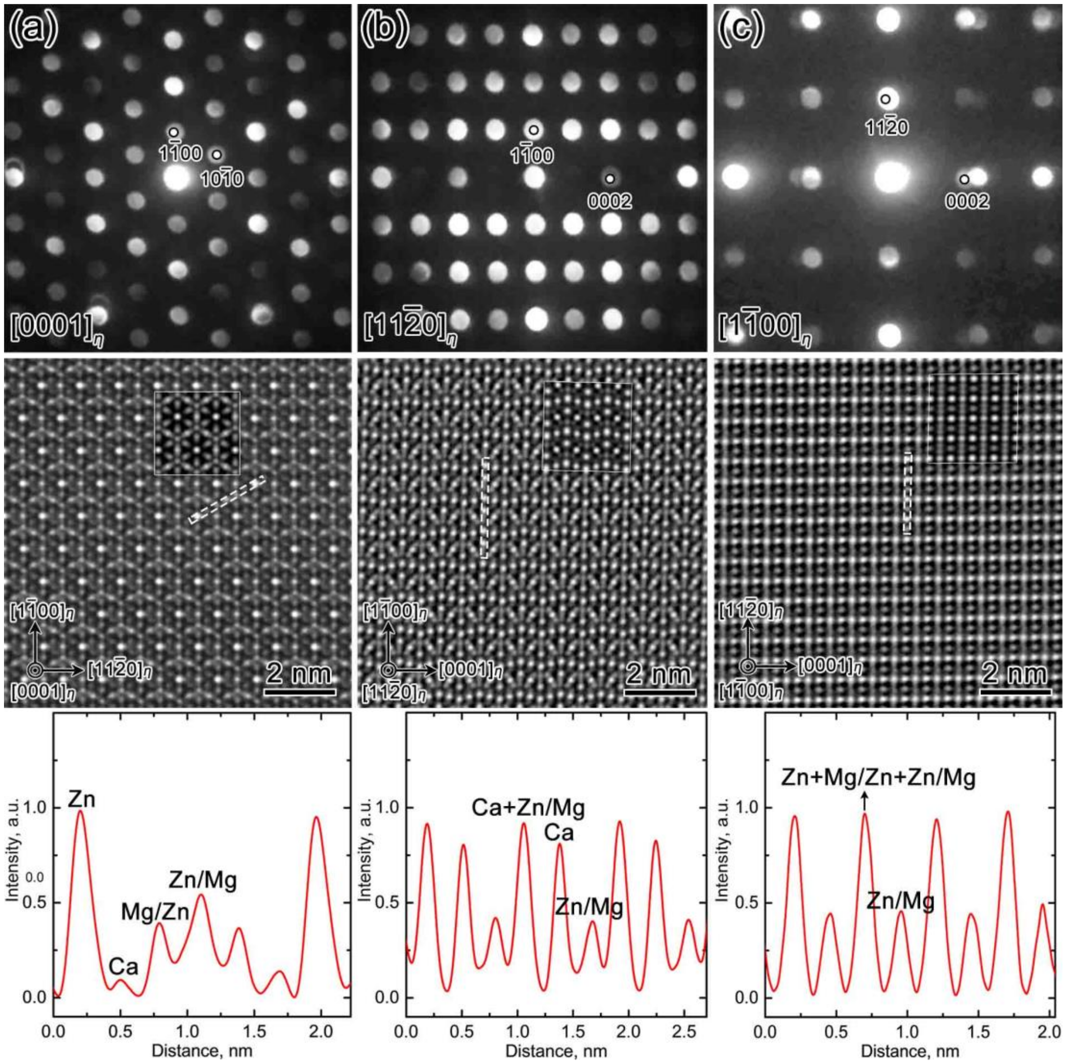

Fig. 5.9 The NBED patterns, atomic resolution HAADF-STEM images, and intensity profiles along selected atomic columns of the η phase taken from (a) $[0001]_\eta$, (b) $[11\bar{2}0]_\eta$, and (c) $[1\bar{1}00]_\eta$ zone axes, respectively. Inserted are simulated images enclosed by white frames.

Ca atoms. To distinguish the difference in the imaging contrast among the columns, the intensity profile analysis was performed to reveal the locations of different types of atoms along the selected columns. Based on the speculations, the HAADF-STEM simulations were performed repeatedly until the imaging contrast in simulated images is consistent with that in the HAADF-STEM one, as inserted in the atomic resolution HAADF-STEM images. As a result, the atomic model of η phase is supposed to have 38 atoms in the unit cell (6 Ca atoms, 2 Zn atoms, 14 Mg atoms, 12 Zn/Mg atoms, 4 Mg/Zn atoms) and a composition of $Mg_{10}Ca_3Zn_6$.

Table 5.1 NBED pattern symmetries, possible diffraction and point groups obtained from experimental NBED patterns

Zone axis	Ideal ZOLZ symmetry	Possible diffraction groups	Possible point groups
$\langle 0001\rangle_\eta$	6mm	$6m_Rm_R$, $6mm1_R$, 6mm, 6_Rmm_R	m3m, 6/mmm, 6mm, 622, $\bar{3}$m
$\langle 11\bar{2}0\rangle_\eta$ $\langle 1\bar{1}00\rangle_\eta$	2mm	$2m_Rm_R$, $2mm1_R$, 2mm, 2_Rmm_R	m3m, m3, 6/mmm, 622, 4/mmm, 422

Table 5.2 Reflection conditions obtained from experimental NBED patterns

Space group	$hh\overline{2h}l$	$h\bar{h}0l$	$000l$	$hkil$
P6/mmm	—	—	—	—
P6/mcc	$l = 2n$	$l = 2n$	$l = 2n$	$l = 2n$
$P6_3$/mcm	—	$l = 2n$	$l = 2n$	$l = 2n$
$P6_3$/mmc	$l = 2n$	—	$l = 2n$	$l = 2n$

Based on the experimental information, the the unit cell of atomic model of η phase is proposed, as shown in **Fig. 5.10 (a)-(c)**. Within the unit cell, 11 atomic columns are occupied by either Zn or Mg along the $[0001]_\eta$ direction with the Zn/Mg ratio of 3:1 or 1:1 on each atomic site, as marked by the mixed atomic symbols in **Fig. 5.10a**. The atomic model viewed from $[11\bar{2}0]_\eta$ and $[1\bar{1}00]_\eta$ are shown in **Figs. 5.10b and c**, respectively. Based on this atomic model, the STEM images and SAED patterns are simulated along the $[0001]_\eta$, $[11\bar{2}0]_\eta$, and $[1\bar{1}00]_\eta$, and these simulated results are consistent with the experimental patterns in **Fig. 5.9**.

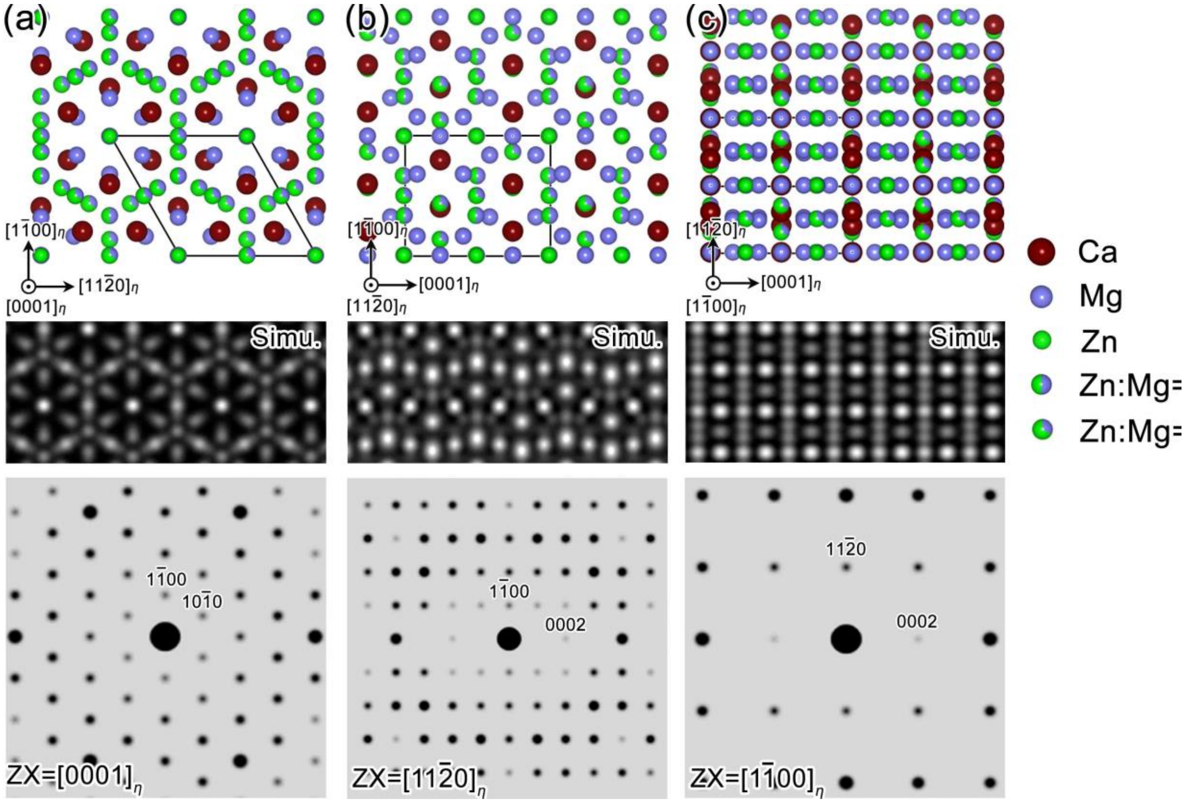

Fig. 5.10 The proposed atomic models, simulated STEM images, and SAED patterns of the η phase viewed along the (a) $[0001]_\eta$, (b) $[11\bar{2}0]_\eta$, and (c) $[1\bar{1}00]_\eta$ directions.

Structures with definitive configurations must be chosen for those mixed sites in DFT calculations to analyze the thermodynamic stability of the atomic model of the η phase in **Fig. 5.10** Considering the disordering on those mixed sites and the ordering pattern based on the experimentally determined group symmetry (*i.e.*, $P6_3/mmc$), both disordered and ordered supercells of the η phase were built. For the disordered ones, 6 different structures with Mg and Zn atoms randomly occupying the mixed sites were built using SQS following the elemental fraction of the proposed atomic model. The atomic structures of the 6 random structures are shown along the $[0001]_\eta$ direction in **Fig. 5.11**. For ordered configurations, the structures with definitive atomic occupations on mixed sites were enumerated to find the ones with the space group of $P6_3/mmc$. The search process is: (i) 3612 possible structures in the proposed atomic model of 38 atoms were enumerated on the non-determined mixed sites; (ii) 10 structures were selected after

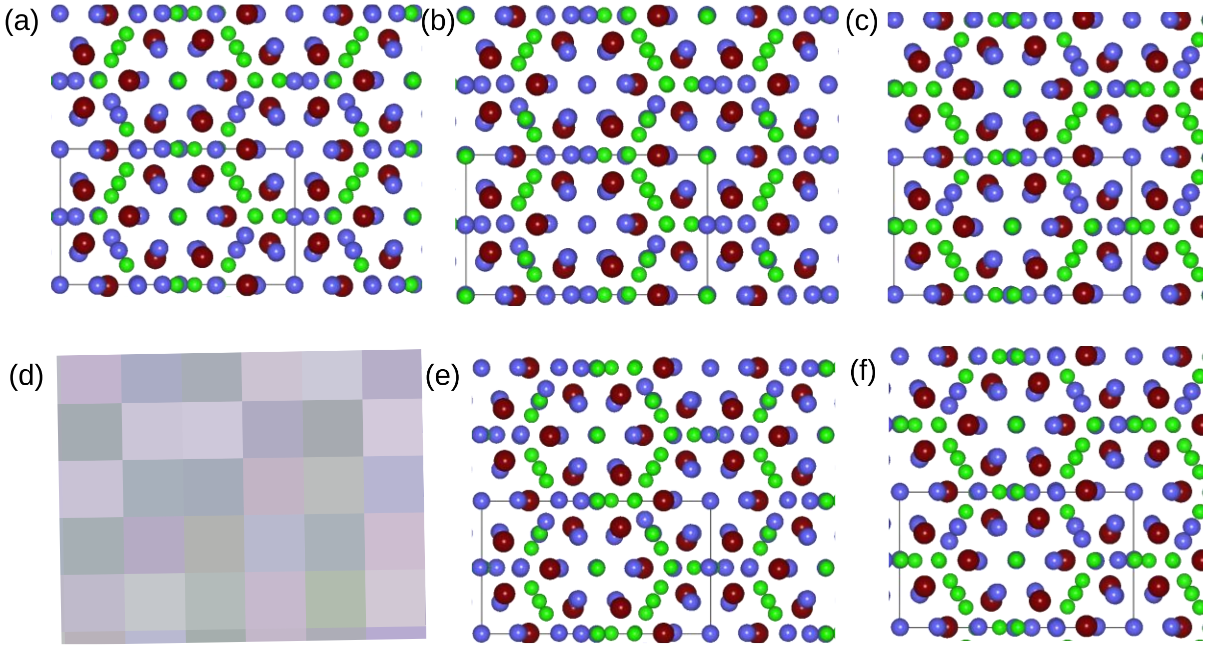

Fig. 5.11 The atomic structures of the 6 random configurations on the mixed sites in the atomic model of η phase viewed from the $[0001]_\eta$ directions. (a) Candidate 1, (b) Candidate 2, (c) Candidate 1, (d) Candidate 2, (e) Candidate 1, (f) Candidate 2.

limiting the concentration of Mg to 49-61 at.%, and the point group form the NBED pattern (listed in **Tables 5.1 and 5.2**); (iii) 2 structures with the composition of $Mg_{10}Ca_3Zn_6$ showing the space group of $P6_3/mmc$ (a = 0.96 nm, c = 1.03 nm) after structural optimization in DFT were determined as the final candidates.

The two searched structures with exact symmetry of $P6_3/mmc$ after all-degree relaxations are shown along the $[0001]_\eta$, $[11\bar{2}0]_\eta$, and $[1\bar{1}00]_\eta$ directions in **Fig. 5.12**. The main difference for the two structures is from the configurations the mixed sites. The As seen, despite the different elements on the mixed sites in the atomic model, the structures are stable, and atoms are stay almost on their ideal positions. This means the structure is not sensitive to the configurations, which is also confirmed by later random structures instructed by SQS based on the propose atomic model. **Fig.5.13** shows the simulated STEM images and SAED patterns of the two η candidates

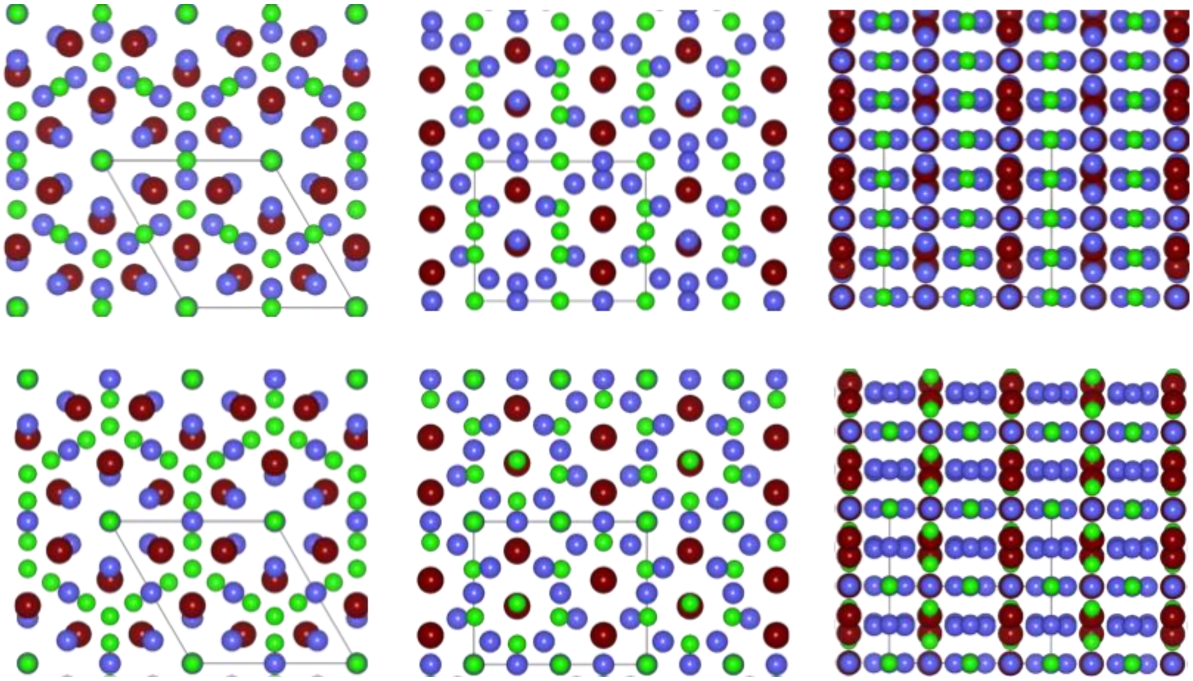

Fig. 5.12 The atomic structures of the two searched η phase with space group of $P6_3/mmc$ viewed from the $[0001]_\eta$, $[11\bar{2}0]_\eta$, and $[1\bar{1}00]_\eta$ directions, respectively. (a) Candidate 1, (b) Candidate 2.

obtained from DFT calculations with a composition of $Mg_{10}Ca_3Zn_6$ and space group of $P6_3/mmc$ along the $[0001]_\eta$, $[11\bar{2}0]_\eta$, and $[1\bar{1}00]_\eta$ directions, respectively. The atomic intensities of columns in the simulated STEM images for the two ordered structures are slightly different from those in the experiments in **Fig. 5.9**. From [0001] direction, the six bright dots within a unit hexagon connecting the six vertexes and the central dot is much brighter in **Fig. 5.9 (a)** of candidate 1 and less brighter in **Fig. 5.9 (b)** of candidate 2 compared with the experimental observation. Similar trend of brightness happens for zigzag along $[0001]_\eta$ from $[11\bar{2}0]_\eta$ direction. The simulated SAED patterns of both cases are agree well with the experimental results. The difference is due to the fact that experimental HAADF-STEM images reveal the statistically averaged information of atomic columns, while specific atomic configurations with a definitive cell must be chosen in DFT, where the elemental fractions in atomic columns may deviate from their statistical average. Therefore, it confirms the presence of disordering on the mixed sites because the

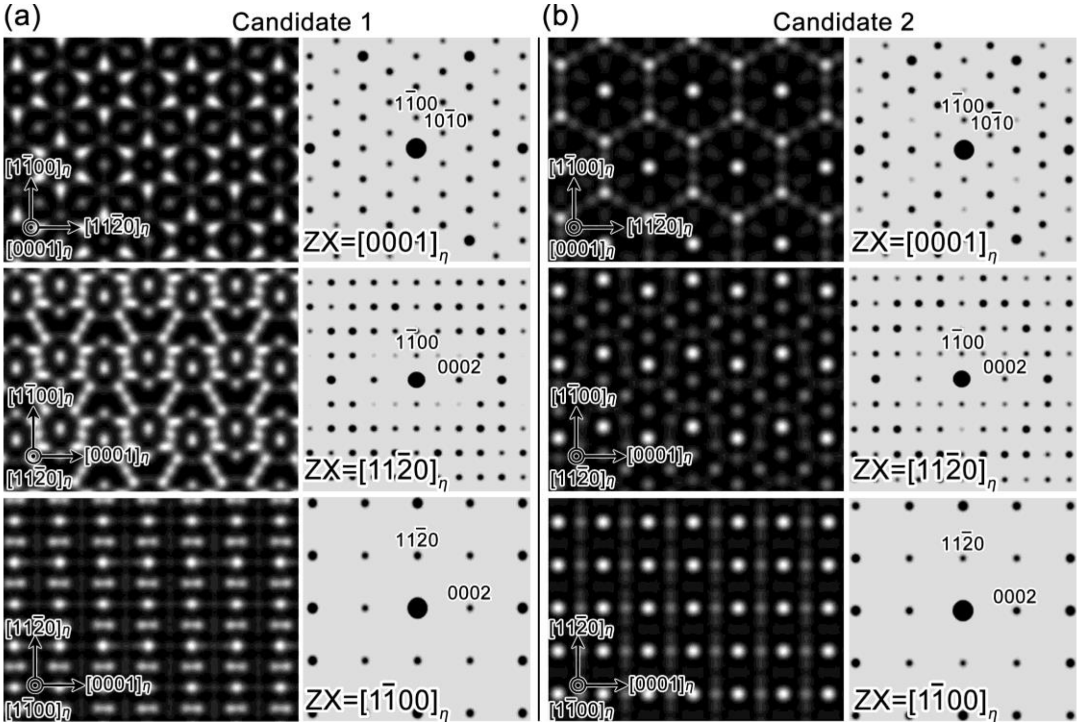

Fig. 5.13 Simulated STEM images and SAED patterns of the η phase obtained from the $[0001]_\eta$, $[11\bar{2}0]_\eta$, and $[1\bar{1}00]_\eta$ directions, respectively. (a) Candidate 1, (b) Candidate 2.

simulated and the experimental STEM images only match when considering the statistically averaged effect of atomic columns on the mixed sites, **Fig. 5.10**. This difference confirms the disordering on the mixed sites since the simulated and the experimental STEM images only match when considering the statistically averaged effect of atomic columns on the mixed sites (**Fig. 5.10**). Further, the structures with 6 random configurations and 2 ordered configurations on the mixed sites of η phase have the same composition and very close formation energies in DFT calculations, i.e., from -15.437 to -14.887 kJ/mol, which explains the disordering of Mg and Zn on those mixed sites of η phase.

To explore the thermodynamic stabilities of these phases, we calculated their formation energy per solute, *i.e.*, E_f^{solute}, based on the proposed atomic structures. In addition to these phases, the formation energy of ordered monolayer G.P. zones and solid solutions are also included for a complete picture [15]. The E_f^{solute} is analyzed as a function of $x_{\mathrm{Zn}}/(x_{\mathrm{Zn}}+x_{\mathrm{Ca}})$ to facilitate a comparison of structures with varying Mg concentration but fixed Zn/Ca ratios [36,37]. As shown

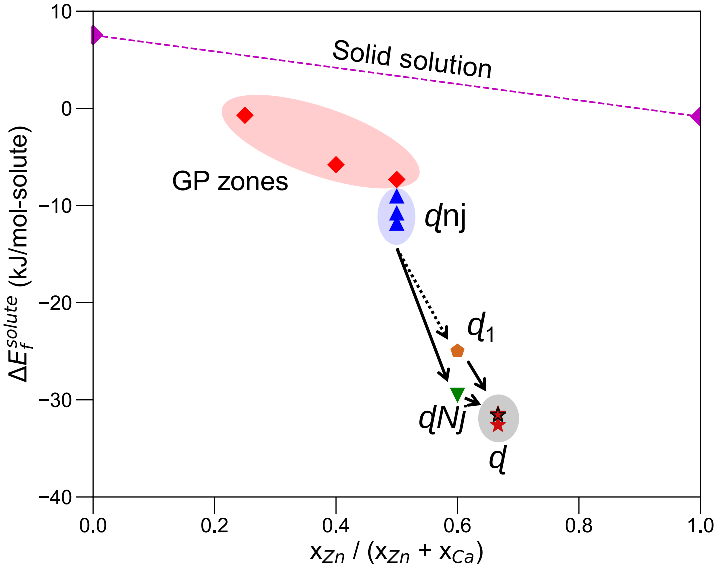

Fig. 5.14 Formation energy per solute E_f^{sloute} of series of precipitates observed during the aging process.

in **Fig. 5.14**, the E_f^{solute} decrease is generally consistent with the observed precipitation sequence: S.S.S.S → G.P. zones → η'' → η' / η_1 → η. Additionally, the Zn/Ca ratio generally increases along this sequence, which shows a correlation between decreasing energy and increasing Zn/Ca ratio as precipitation process proceeds. Note that the proposed η_1 phase has a slightly higher E_f^{solute} than that of η', which indicates the proposed η_1 phase can be less stable than η'. As discussed before, the formation of the η_1 phase is likely to be facilitated by defects, while the effect of defects on its formation energy is not incorporated in first-principles calculations due to the small simulation cells. Despite the small difference, the energies per solutes for η_1 and η' are close, indicating that they are likely to coexist in experiments. For the η phase, the formation energies per solute of structures with random occupations are marked by black stars, while the ordered ones with a space group of $P6_3/mmc$ are marked by red stars. As shown, the energies marked by both black and red stars are very close, indicating that these structures of η are nearly equally probable to be observed experimentally and their coexistence leads to the mixed sites in the observed η phase.

5.4 Conclusion

In this work, we thoroughly investigated the precipitation process and the structures of precipitates in the Mg-0.3Ca-0.6Zn alloy with a combined use of HAADF-STEM imaging, 3D-APT, and DFT calculations. The main conclusions are summarized as follows:

1. Precipitation during isothermal aging at 200 °C involves the evolution from the G.P. zones to the equilibrium η phase, and the formation of a series of metastable phases; η'', η', and η_1 in the intermediate process. The precipitation sequence is proposed as:

S.S.S.S_ G.P. zones_ η'' → η' → η' pairs and stacks / η_1 → η

The formation energies per solute of each phase decrease along this precipitation sequence in DFT calculations, which provides thermodynamic reasoning behind the observed sequence.

2. The monolayer G.P. zones in the peak-aged sample transform to the η'' and η' $(0001)_\alpha$ plates with single unit-cell height during the over-aging. The Zn/Ca ratio of plates evolves from 1 to 1.5. The η'' has a disordered hexagonal structure; Pm, a = 0.55 nm, c = 0.53 nm and a composition of $Mg_5Ca_2Zn_2$, while η' has a composition of $Mg_4Ca_2Zn_3$ with a symmetry group of $P\bar{6}2m$, a = 0.55 nm, c = 0.49 nm. The crystal structures and atomic occupancies of η'' and η' were deduced through a synthesis of the information from STEM, 3D-APT, and DFT calculations.

3. The η' plates develop into pairs and stacks with the interplanar spacing most in ~ 4 to 5 α-Mg layers after 100 h aging. This spacing is proven to be the most energetically stable in DFT for the stacking of η' plates in the Mg matrix. Coarse η_1 plates (Pm, a = 0.57 nm, c = 0.97 nm) also heterogeneously form on the $(0002)_\alpha$ plane with a composition of $Mg_7Ca_2Zn_3$. The orientation relationship between the η_1 and the α-Mg matrix is such that $(0001)_{\eta_1}$ // $(0001)_\alpha$, $[1\bar{1}00]_{\eta_1}$ // $[11\bar{2}0]_\alpha$.

4. The equilibrium η phase has a hexagonal structure; $P6_3/mmc$, a = 0.96 nm, c = 1.03 nm with a composition of $Mg_{10}Ca_3Zn_6$. The orientation relationship between the rhombic-shaped η basal plate and the α-Mg matrix is described as $(11\bar{2}0)_\eta$ // $(0001)_\alpha$, $[0001]_\eta$ // $[11\bar{2}0]_\alpha$, while the lath-shaped η non-basal plate is such that $(01\bar{1}0)_\eta$ // $(1\bar{1}03)_\alpha$, $[0001]_\eta$ // $[11\bar{2}0]_\alpha$. The mixed Mg/Zn sites within the phase are confirmed by DFT calculations, which leads to the statically averaged effect on the atomic column intensities in the experimental HAADF-STEM results.

References

[1] S. You, Y. Huang, K.U. Kainer, N. Hort, Recent research and developments on wrought magnesium alloys, J. Mag. Alloys 5 (2017) 239-253.

[2] Y. Chen, Z. Xu, C. Smith, J. Sankar, Recent advances on the development of magnesium alloys for biodegradable implants, Acta Biomater, 10 (2014) 4561-4573.

[3] C.L. Mendis, K. Oh-ishi, Y. Kawamura, T. Honma, S. Kamado, K. Hono, Precipitation hardenable Mg–2.4Zn–0.1Ag–0.1Ca–0.16Zr (at.%) wrought magnesium alloy, 57 (2009) 749-760.

[4] Z.H. Li, T.T. Sasaki, T. Shiroyama, A. Miura, K. Uchida, K. Hono, Simultaneous achievement of high thermal conductivity, high strength and formability in Mg-Zn-Ca-Zr sheet alloy, Mater. Res. Lett. 8 (2020) 335–340.

[5] M.Z. Bian, T.T. Sasaki, T. Nakata, Y. Yoshida, N. Kawabe, S. Kamado, K. Hono, Bake-hardenable Mg-Al-Zn-Mn-Ca sheet alloy processed by twin-roll casting, Acta Mater. 158 (2018) 278-288.

[6] Z.H. Li, T.T. Sasaki, T. Shiroyama, A. Miura, K. Uchida, K. Hono, Role of Zn on the rapid age-hardening in Mg-Ca-Zn alloys, Scr. Mater. 216 (2022) 114735.

[7] X. Gao, S.M. Zhu, B.C. Muddle, J.F. Nie, Precipitation-hardened Mg–Ca–Zn alloys with superior creep resistance, Scr. Mater. 53 (2005) 1321-1326.

[8] M. Cihova, E. Martinelli, P. Schmutz, A. Myrissa, R. Schäublin, A.M. Weinberg, P.J. Uggowitzer, J.F. Löffler, The role of zinc in the biocorrosion behavior of resorbable Mg–Zn–Ca alloys, Acta. Biomater. 100 (2019) 398-414.

[9] P. Holweg, L. Berger, M. Cihova, N. Donohue, B. Clement, U. Schwarze, N.G. Sommer, G. Hohenberger, J. van den Beucken, F. Seibert, A. Leithner, J.F. Loffler, A.M. Weinberg, A lean

magnesium-zinc-calcium alloy ZX00 used for bone fracture stabilization in a large growing-animal model, Acta Biomater. 113 (2020) 646-659.

[10] J.F. Nie, Precipitation and hardening in magnesium alloys, Metall. Mater. Trans. A 43A (2012) 3891–3939.

[11] D.H. Ping, K. Hono, J.F. Nie, Atom probe characterization of plate-like precipitates in a Mg–RE–Zn–Zr casting alloy, Scr. Mater. 48 (2003) 1017–1022.

[12] J.C. Oh, T. Ohkubo, T. Mukai, K. Hono, TEM and 3DAP characterization of an age-hardened Mg–Ca–Zn alloy, Scr. Mater. 53 (2005) 675–679.

[13] K. Oh-ishi, R. Watanabe, C.L. Mendis, K. Hono, Age-hardening response of Mg–0.3 at.% Ca alloys with different Zn contents, Mater. Sci. Eng. A 526 (2009) 177–184.

[14] B. Langelier, X. Wang, S. Esmaeili, Evolution of precipitation during non-isothermal ageing of an Mg-Ca-Zn alloy with high Ca content, Mat. Sci. Eng. A 538 (2012) 246-251.

[15] D. Cheng, E.R. Hoglund, K. Wang, J.M. Howe, S.R. Agnew, B. Zhou, Atomic structures of ordered monolayer GP zones in Mg-Zn-X (X= Ca, Nd) systems, Scr. Mater. 216 (2022) 114744.

[16] J.F. Nie, B.C. Muddle, Precipitation hardening of Mg-Ca (-Zn) alloys, Scr. Mater. 37 (1997) 1475-1481.

[17] J.F. Nie, K. Oh-ishi, X. Gao, K. Hono, Solute segregation and precipitation in a creep-resistant Mg–Gd–Zn alloy, Acta Mater. 56 (2008) 6061–6076.

[18] Y.M. Zhu, K. Oh-ishi, N.C. Wilson, K. Hono, A.J. Morton, J.-F. Nie, Precipitation in a Ag-containing Mg-Y-Zn Alloy, Metall. Mater. Trans. A 47 (2016) 927–940.

[19] K. Saito, M. Nishijima, K. Hiraga, Stabilization of Guinier-Preston zones in hexagonal close-packed Mg-Gd-Zn alloys studied by transmission electron microscopy, Mate. Trans. 51 (2010) 1712-1714.

[20] K. Saito, A. Yasuhara, K. Hiraga, Microstructural changes of Guinier-Preston zones in an Mg–1.5at.%Gd–1at.%Zn alloy studied by HAADF-STEM technique, J. Alloy Compd. 509 (2011) 2031-2038.

[21] G. Levi, S. Avraham, A. Zilberov, M. Bamberger, Solidification, solution treatment and age hardening of a Mg–1.6 wt.% Ca–3.2 wt.% Zn alloy, Acta Mater. 54 (2006) 523–530.

[22] P.M. Jardim, G. Solorzano, J.B. Vander Sande, Precipitate crystal structure determination in melt spun Mg-1.5wt%Ca-6wt%Zn alloy, Microsc. Microanal. 8 (2002) 487–496.

[23] Y.-N. Zhang, D. Kevorkov, F. Bridier, M. Medraj, Experimental study of the Ca-Mg-Zn system using diffusion couples and key alloys, Sci. Technol. Adv. Mat. 12 (2011) 025003.

[24] J.D. Cao, T. Weber, R. Schäublin, J.F. Löffler, Equilibrium ternary intermetallic phase in the Mg-Zn-Ca system, J. Mater. Res. 31 (2016) 2147-2155.

[25] R.E. Schäublin, M. Becker, M. Cihova, S.S.A. Gerstl, D. Deiana, C. Hébert, S. Pogatscher, P.J. Uggowitzer, J.F. Löffler, Precipitation in lean Mg–Zn–Ca alloys, Acta Mater. 239 (2022) 118223.

[26] A. J. Ardell, Precipitation hardening, Metal. Trans. A, 16 (1985) 2131-2165.

[27] A. Zunger, S.H. Wei, L.G. Ferreira, J.E. Bernard. Special quasirandom structures, Phys. Rev. Lett. 65 (1990) 353.

[28] A. van de Walle, P. Tiwary, M. de Jong, D.L. Olmsted, M. Asta, A. Dick, D. Shin, Y. Wang, L.Q. Chen, Z.K. Liu, Efficient stochastic generation of special quasirandom structures, Calphad. 42 (2013) 13-18.

[29] A. van de Walle, Multicomponent multisublattice alloys, nonconfigurational entropy and other additions to the Alloy Theoretic Automated Toolkit, Calphad. 33 (2009) 266-278.

[30] W. Kohn, L.J. Sham, Self-consistent equations including exchange and correlation effects, Phys. Rev. 140 (1965) A1133.

[31] P. Hohenberg, W. Kohn, Inhomogeneous electron gas, Phys. Rev. 136 (1964) 864.

[32] D. Joubert, From ultrasoft pseudopotentials to the projector augmented-wave method, Phys. Rev. B 59 (1999) 1758-1775.

[33] J.P. Perdew, K. Burke, M. Ernzerhof, Generalized gradient approximation made simple, Phys. Rev. lett. 77 (1996) 3865-3868.

[34] G. Kresse, Efficient iterative schemes for ab-initio total-energy calculations using a plane-wave basis set, Phys. Rev. B. 54 (1996) 11169-11186.

[35] G. Kresse, J. Furthmuller, Efficiency of ab-initio total energy calculations for metals and semiconductors using a plane-wave basis set, Comput. Mater. Sci. 6 (1996) 15-50.

[36] C. Ravi, C. Wolverton, First-principles study of crystal structure and stability of Al-Mg-Si-(Cu) precipitates, Acta Mater. 52 (2004) 4213-4227.

[37] D. Wang, M. Amsler, V.I. Hegde, J.E. Saal, A. Issa, B.C. Zhou, X. Zeng, C. Wolverton, Crystal structure, energetics, and phase stability of strengthening precipitates in Mg alloys: A first-principles study, Acta Mater. 158 (2018) 65-78.

[38] Z. Li, J. Zheng, B. Chen, Unravelling the structure of γ″ in Mg-Gd-Zn: an atomic-scale HAADF-STEM investigation, Mater. Charact. 120 (2016) 345–348.

[39] X. Gu, T. Furuhara, T. Kiguchi, T.J. Konno, L. Chen, P. Yang, On the atomic structure of γ″ phase in Mg-Zn-Gd alloy, Scr. Mater. 146 (2018) 64–67.

[40] H. Xie, H. Pan, Y. Ren, S. Sun, L. Wang, H. Zhao, B. Liu, X. Qi, G. Qin, Magnesium alloys strengthened by nanosaucer precipitates with confined new topologically close-packed structure, Cryst. Growth Des. 18 (2018) 5866–5873.

[41] R.K.W. Marceau, G. Sha, R. Ferragut, A. Dupasquier, S.P. Ringer, Solute clustering in Al–Cu–Mg alloys during the early stages of elevated temperature ageing, Acta Mater. 58 (2010) 4923–4939.

[42] M.W. Zandbergen, Q. Xu, A. Cerezo, G.D.W. Smith, Study of precipitation in Al–Mg–Si alloys by Atom Probe Tomography I. Microstructural changes as a function of ageing temperature, Acta Mater. 101 (2015) 136–148.

[43] K.Buchanan, K.Colas, J.Ribis, A.Lopez, J.Garnier, Analysis of the metastable precipitates in peak-hardness aged Al-Mg-Si(-Cu) alloys with differing Si contents, Acta Mater. 132 (2017) 209-221.

[44] J.P. Morniroli, J.W. Steeds, Microdiffraction as a tool for crystal structure identification and determination, Ultramicroscopy 45 (1992) 219–239.

[45] B.F. Buxton, J.A. Eades, J.W. Steeds, G.M. Rackham, The symmetry of electron diffraction zone axis patterns, Philos. Trans. Royal Soc. A 281 (1976) 171–194.

[46] T. Hahn, International Table for Crystallography, Volume A: Space-Group Symmetry, 5th ed., Springer, New York, 2005.

[47] N. Fujita, M. Matsushita, R. Tsukamoto, M. Yamasaki, Y. Kawamura, T. Irifune, E. Abe, The structure of a novel long-period superlattice phase in $Mg_{97}Zn_1Yb_2$ alloys, Scr. Mater. 150 (2018) 78–81.

[48] Palmer, D. C. (2014). CrystalMaker. CrystalMaker Software Ltd, Begbroke, Oxfordshire, England.

Chapter 6 includes: 1) theoretical derivations of extending the MSCE method; 2) the ternary CE results in the Mg-Zn-Ca system. The first part is adapted from the submitted paper to npj Computational Materials: K. Wang, D. Cheng, B.C. Zhou. “Mixed-space cluster expansion in multicomponent system with arbitrary lattice”. For the content of this chapter, B.C. Zhou, K. Wang conceived the study. K. Wang extended the theory of MSCE to systems of multi-sublattices. D. Cheng generalized the algorithm of CSE to the system with arbitrary symmetry and lattice mismatch, proposed a method to extend MSCE to multicomponent systems, and performed the CE calculations of the Mg-Zn-Ca system.

Chapter 6 Development of Mixed Space Cluster Expansion

6.1 Introduction

The site occupation of atoms on parent lattice determines the thermodynamic interaction, and thus the variation of the site occupation gives rise to the configurational degrees of freedom for alloy thermodynamics [1–6]. Cluster expansion (CE) describe the energies as a function of configurations on a given lattice by an Ising Hamiltonian, **Eq. (2.11)**. It has been proven that, for m component system on a lattice of N sites, the total energy of m^N possible configurations can be exactly mapped onto a generalized Ising model based on the energetic contributions of atomic clusters on parent lattice [7]. Using DFT calculations [8,9], the energies are abstained for each configuration independently and fail to take advantage of the underlying similarity among all different configurations. But CE is capable to obtain the energetic contributions of atomic clusters, or effective cluster interactions (ECIs) from a small set of structures to predict energies of all other configurations [10]. With the analytical linear Hamiltonian, CE can calculate energies rapidly, be applied to search ground states, and be combined with statistical methods, e.g., Monte Carlo, to calculate phase diagram. Applications of CE to wide variety of materials confirm that the chemical interaction is short-ranged in nature and can be accurately captured using simple clusters (e.g., pairs, triplets, and quadruplets) with small diameters (i.e., largest two-site distance in a cluster), and only a small number of energies for coherent structures with small unit cell (~ 10 atoms) are required in the training set of CE [11].

However, long-ranged interactions in materials, other than short-ranged chemical interactions, may play important roles in phase stability, morphology, and hence the shape of phase diagram [12,13,14]. The size-mismatch-caused coherency strain is one of the most common long-range interactions. Since CE Hamiltonian is based on the short-range cluster energies from DFT calculations, the limited size of DFT cell constrain the range of interaction to tens of angstrom and unable to capture the long-range strain interactions. Even if such simulation cells can be handled by DFT with large computational cost, the number of alloy configurations increases exponentially with the number of lattice sites, and thus DFT calculations for a great number of large structures are needed, which poses tremendous computational burden. For example, the number of binary alloy configurations for a cell with 24 atoms is $2^{24} = 16{,}777{,}216$, which reduces to $6{,}980{,}276$ if the symmetry of HCP crystal is considered. In addition, As the cut-off distance is increased, the number of fitting parameters increases quickly and can easily exceeds the number of training structures, making the fitting process meaningless due to the infinite number of solutions for such situations. All those reasons may lead to the non-convergence of the traditional CE.

To incorporate long-ranged strain interactions and improve the convergence of CE, Laks et al. proposed Mix-Space Cluster Expansion [17–19]. In this method, they consider long-range interaction through the Fourier transformation of the pair energies (ECI) in CE Hamiltonian into the reciprocal space (*k*-space) based on the static concentration wave (SCW) method [13]. In this way, the long-range interaction in real space turns into short-ranged interactions in reciprocal space. Theoretically, the method can capture pair-interactions with any length. The interaction parameters in *k*-space are obtained based on the strain energy required for alloy constituents to maintain coherency in the epitaxial configuration, which is termed constituent strain energy (CSE), **Eq. (2.13)**. Such formulation corresponds to the $\mathrm{A}_q\mathrm{B}_q$ type ordering in the long-periodicity limit ($q \rightarrow \infty$), which corresponds to $|\boldsymbol{k}| = 0$. To consider the media-range interactions , e.g., $|\boldsymbol{k}|$ is finite, the attenuation factor is used to capture the decreasing trend [16]. The method has been applied in many binary alloy and semi-conductor systems [20–32].

6.2 Extension to crystal with multiple sublattices and arbitrary symmetry

The MSCE approach has been overlooked in recent years, mainly due to its limitations to binary alloys with single sublattice and cubic crystal symmetry. This single sublattice limitation is rooted in the formulation of *k*-space energy, while the cubic symmetry of the underlying lattice is from the formalism of long-ranged CSE [13]. Although system with hexagonal symmetry was studies based on the calculations of CSE later by Issa et al.[33], the calculation was only limited to basal and $(10\bar{1}0)_{\mathrm{Mg}}$ planes of the HCP crystal. Hence, a method to calculate CSE for systems with arbitrary crystal symmetry, lattice mismatch and crystallographic plane is needed. In this Section, the MSCE method that can be applied to systems with multiple sublattice with any symmetry is developed.

The development process includes: (1) formulating k-space pair interactions for multiple sublattices; (2) modeling configuration-dependent long-ranged interactions in k-space; (3) calculating CSE for arbitrary lattice mismatch and crystal symmetry; (4) regularizing the ECIs by smoothness condition; (5) anisotropic attenuation of the long-ranged interactions.

6.2.1 Formulation of *k*-space pair interactions for multiple sublattices

In the original formulation of Laks et al., only phases on a single sublattice were considered [13]. In this case, only one atom is on each Bravais lattice site. However, as we know, in the theory of crystal, multiple atoms can form a basis, and each basis is on the ideal Bravais lattice site. These multiple atoms in the basis corresponds to multiple sublattice, which is the terminology widely used in context of materials thermodynamics. For a crystalline structure with multiple sublattices, the Fourier transform of the spin variable (i.e., the structural factor) follows [34,35],

$$S_{\boldsymbol{k},p}(\sigma) = \frac{1}{N}\sum_{l=1}^{N} S_{l,p}(\sigma) \cdot e^{i\boldsymbol{k}\cdot\boldsymbol{R}_l} \tag{6.1}$$

where N is the number of primitive cells, or basses, of the parent lattice in the structure (or the number of basis), v is the number of sublattices (the number of atoms in the primitive cell or in the basis of the parent lattice), $\boldsymbol{R}_l$ denotes the coordinate of the origin of the l-th primitive cell in the structure and p is the index for the p-th atom in the basis of the primitive cell. Following **Eq. (6.1)**, the inverse Fourier transform is,

$$S_{l,p}(\sigma) = \sum_{\boldsymbol{k}} S_{\boldsymbol{k},p}(\sigma) \cdot e^{-i\boldsymbol{k}\cdot\boldsymbol{R}_l} \tag{6.2}$$

The Fourier transformation and its inversed one are the starting point to express a configuration in the reciprocal space. It is reasonable that there are long-ranged multi-body interactions in principle. however, instead of directly expressing the multi-body interaction in reciprocal space, we use very large number of pair interactions to compensate them. This is because of the mathematical complexity of inversion of multiple atoms in real space[1,13,35]. Fortunately, it is proved that the long-ranged multi-body interactions are insignificant compared with pair interactions [1,13]. For the case with multiple sublattices, the interaction from a pair of atoms at $\boldsymbol{R}_i + \boldsymbol{h}_m$ and $\boldsymbol{R}_j + \boldsymbol{h}_n$ follow,

$$\begin{aligned} E_2(\sigma) &= \frac{1}{2}\sum_{i,j}\sum_{m,n} J\big(\boldsymbol{R}_i + \boldsymbol{h}_m, \boldsymbol{R}_j + \boldsymbol{h}_n\big) \cdot S_{i,m}(\sigma) \cdot S_{j,n}(\sigma) \\ &= \frac{1}{2}\sum_{i,j}\sum_{m,n} J_{m,n}\big(\boldsymbol{R}_i, \boldsymbol{R}_j\big) \cdot S_{i,m}(\sigma) \cdot S_{j,n}(\sigma) \\ &= \frac{1}{2}\sum_{i,j} \tilde{S}_i^T(\sigma) \cdot \tilde{J}\big(\boldsymbol{R}_j - \boldsymbol{R}_i\big) \cdot \tilde{S}_j(\sigma) \end{aligned} \tag{6.3}$$

where i and j run over the lattice sites and m and n run over the sublattices. $J_{m,n}\big(\boldsymbol{R}_i, \boldsymbol{R}_j\big) = J_{m,n}\big(\boldsymbol{R}_j - \boldsymbol{R}_i\big)$ is the pair interaction between atoms on m- and n-th sublattice. These two-dimensional variables can also be expressed in matrix, as shown in the last line in **Eq. (6.3)**, where $\tilde{S}_i(\sigma)$ is the column vector of the spin variables of atoms in the basis located at $\boldsymbol{R}_i$ and the superscript T denotes transposition. $\tilde{J}\big(\boldsymbol{R}_j - \boldsymbol{R}_i\big)$ is the $v \times v$ matrix of pair ECIs. Since the spin variable must be real numbers in *r*-space, $S_{\boldsymbol{k},p} = S^*_{-\boldsymbol{k},p}$ where the superscript * indicates the complex conjugate. Substitution of **Eq. (6.2)** with **Eq. (6.3)** leads to the pair interaction in *k*-space,

$$\begin{aligned}
E_2(\sigma) &= \frac{1}{2}\sum_{i,j}\sum_{m,n} J_{m,n}(\boldsymbol{R}_i,\boldsymbol{R}_j)\cdot S_{i,m}(\sigma)\cdot S_{j,n}(\sigma) \\
&= \frac{1}{2}\sum_{i,j}\sum_{m,n} J_{m,n}(\boldsymbol{R}_i,\boldsymbol{R}_j)\cdot\left(\sum_{\boldsymbol{k}} S_{\boldsymbol{k},m}(\sigma)\cdot e^{-i\boldsymbol{k}\cdot\boldsymbol{R}_i}\right)\cdot\left(\sum_{\boldsymbol{k}'} S^*_{-\boldsymbol{k}',n}(\sigma)\cdot e^{-i\boldsymbol{k}'\cdot\boldsymbol{R}_j}\right) \\
&= \frac{1}{2}\sum_{l}\sum_{m,n} J_{m,n}(\boldsymbol{R}_l)\cdot\left(\sum_{\boldsymbol{k}}\sum_{\boldsymbol{k}'} S_{\boldsymbol{k},m}(\sigma)S^*_{\boldsymbol{k}',n}(\sigma)\cdot e^{-i\boldsymbol{k}\cdot\boldsymbol{R}_l}\cdot\sum_{j} e^{-i(\boldsymbol{k}-\boldsymbol{k}')\cdot\boldsymbol{R}_j}\right) \\
&= N\sum_{\boldsymbol{k}}\sum_{m,n} S_{\boldsymbol{k},m}(\sigma)\cdot V_{m,n}(\boldsymbol{k})\cdot S^*_{\boldsymbol{k},n}(\sigma) \\
&= N\sum_{\boldsymbol{k}} \tilde{S}^T_{\boldsymbol{k}}\cdot\tilde{V}(\boldsymbol{k})\cdot\tilde{S}^*_{\boldsymbol{k}} \qquad (6.4)
\end{aligned}$$

where $\boldsymbol{R}_l = \boldsymbol{R}_j - \boldsymbol{R}_i$ and $V_{m,n}(\boldsymbol{k})$ is the Fourier transform of *r*-space pair interaction energy,

$$V_{m,n}(\boldsymbol{k}) = \frac{1}{2}\sum_{l} J_{m,n}(\boldsymbol{R}_l)\cdot e^{-i\boldsymbol{k}\cdot\boldsymbol{R}_l} \qquad (6.5)$$

And $\tilde{S}_{\boldsymbol{k}} = \frac{1}{N}\sum_l \tilde{S}_l\cdot e^{-i\boldsymbol{k}\cdot\boldsymbol{R}_l}$ is the Fourier transform of $\tilde{S}_l$, i.e., the column vector of the *r*-space spin variable corresponding to site $\boldsymbol{R}_l$. $\tilde{V}(\boldsymbol{k})$ is the $v\times v$ matrix of the $V_{m,n}(\boldsymbol{k})$. In the derivation of **Eqs. (6.4)** and **(6.5)**, the transnational invariance of $J_{m,n}(\boldsymbol{R}_l)$ and $\sum_j e^{-i(\boldsymbol{k}-\boldsymbol{k}')\cdot\boldsymbol{R}_j} = N\delta_{\boldsymbol{k},\boldsymbol{k}'}$ are used. For the case of single sublattice (i.e., $v = 1$), **Eqs. (6.1-5)** reduce to the formulation by Laks et al. [13]. So far, **Eqs. (6.4-5)** are equivalent to the pair interactions in *r*-space CE, since the Fourier transform simply gives *k*-space description of pair interactions. In this way, we extend the single lattice formulation to the one applicable to multi-sublattices.

6.2.2 Long-ranged strain interactions in *k*-space

In the last step, the configurations are expressed in reciprocal space through the Fourier transformation of spin variables in r-space, and the energy contribution from pair interactions are expressed based on the configurations in reciprocal space. Therefore, both real space pair-interaction formulations and its reciprocal version share the same issue of difficult convergence for systems long-ranged interactions. Besides the computational challenges due to large structures and longer cut-offs for clusters, the failure of capturing the contribution of the interaction from the long periodicity limit, i.e., A_qB_q $(q \rightarrow \infty)$, which corresponds to the origin, i.e., Γ point, in the *k*-space [13]. Non-vanishing interactions in the long periodicity limit means that the interaction is non-zero at the origin of *k*-space (i.e., Γ). Since long-ranged interactions are generally orientation-dependent, they approach Γ with different values along different orientations and lead to varying magnitudes of interactions in the neighborhood of Γ. Using spherical coordinates, an infinitesimal change along the azimuthal or polar angle of *k*-point will lead to a finite change of interaction magnitudes around Γ, which is the so-called singularity on the surface of interaction in *k*-space [13,36,37].

The definition of CSE caused by lattice mismatch, **Eq. (2.13)**, is consistent with the long-periodic limit, i.e., A_qB_q $(q \rightarrow \infty)$, which means that CSE represents the limit of long-range interaction of $\boldsymbol{k} \rightarrow \boldsymbol{0}$ along a specific direction defined by the normal of the shared crystallographic plane. In the current modeling, the CSE is described by the long-ranged pair interactions and explicitly separated from the relatively short-ranged pair interactions,

$$\begin{aligned} E_2(\sigma) &= E_2^{SR}(\sigma) + E_2^{LR}(\sigma) \\ &= N \sum_{\boldsymbol{k}} \sum_{m,n} S_{\boldsymbol{k},m}(\sigma) \cdot \left[V_{m,n}^{SR}(\boldsymbol{k}) + V_{m,n}^{LR}(\boldsymbol{k})\right] \cdot S_{\boldsymbol{k},n}^{*}(\sigma) \end{aligned} \quad (6.6)$$

where $V_{m,n}^{SR}(\boldsymbol{k})$ and $V_{m,n}^{LR}(\boldsymbol{k})$ are the short- and long-ranged parts of the pair interactions in *k*-space. The goal of such separation is to let $V_{m,n}^{LR}(\boldsymbol{k})$ contain the singularity of $V_{m,n}(\boldsymbol{k})$ at Γ, so that, after separation, $V_{m,n}^{SR}(\boldsymbol{k})$ is zero at Γ and can be handled by *r*-space methods with a cut-off distance. In practice, $V_{m,n}^{SR}(\boldsymbol{k})$ is interpreted as the chemical interactions of pair clusters and can be obtained by the Fourier transform of the *r*-space pair ECIs using **Eq. (6.5)**. Meanwhile $V_{m,n}^{LR}(\boldsymbol{k})$ is considered as the long-ranged interactions along $\boldsymbol{k}$, i.e., CSE on the plane with normal along $\boldsymbol{k}$**.** Therefore, the configuration dependent CSE follows,

$$E_2^{LR}(\sigma) = N\sum_{\boldsymbol{k}}\sum_{m,n} S_{\boldsymbol{k},m}(\sigma)\cdot V_{m,n}^{LR}(\boldsymbol{k})\cdot S_{\boldsymbol{k},n}^{*}(\sigma) \qquad (6.7)$$

Once the long-ranged strain interaction parameters in *k*-space $V_{m,n}^{LR}(\boldsymbol{k})$ are known, **Eq. (6.7)** along with the definitions of structural factors, **Eqs. (6.1-2)**, is sufficient to calculate the CSE for a given structure.

Next, the CSE is formulated using long-ranged pair interaction in *k*-space (**Eq. (6.7)**) by summing up the effective contribution from each *k*-point in the 1st BZ, rather than explicitly calculating the contribution from each pair of atoms on sublattices. This approach is based on the consideration:

(i) The reciprocal lattice, hence the *k*-points, is defined using the *r*-space lattice vectors and the information of the atoms within the basis is not incorporated.

(ii) The crystallographic orientations and planes are indexed with respect to the lattice vectors in *r*-space, not the atomic positions within the basis of the cell.

(iii) The total energy from DFT is defined for the cell and, when parameterizing the orientation dependence of CSE, the primitive cell is the smallest structural unit obeying periodic boundary condition. The energy of deformed primitive cell by DFT cannot be further decomposed.

This approach means that the long-ranged interaction energy is zero between two atoms within the same primitive cell; the long-ranged pair interactions between two atoms in different primitive cells are calculated using the vector connecting the origins of primitive cells. The former is obvious since long-ranged interaction is expected to have much larger length scales than the primitive cell. The latter means that the vector connecting the origins of primitive cells, rather than the vector using the spatial positions of atomic pairs, is used for orientation of the interaction, since the differences in between is vanishingly small for long-ranged pair interaction. Based on this approach, the configuration dependent CSE reduces to,

$$\Delta E_{CS}(\sigma) = N \sum_{\boldsymbol{k}} \hat{S}_{\boldsymbol{k}}(\sigma) \cdot V^{CS}(\boldsymbol{k}) \cdot \hat{S}^{*}_{\boldsymbol{k}}(\sigma) \qquad (6.8)$$

where $V^{CS}(\boldsymbol{k})$ and $\hat{S}_{\boldsymbol{k}}(\sigma)$ are the long-ranged CSE interaction parameter and the structural factor, corresponding to $\boldsymbol{k}$ incorporating the contributions from multiple sublattices. Following the theory of the X-ray diffraction for multiple sublattices [35], the structural factor for each $\boldsymbol{k}$ point in the 1st Brillouin zone equals the sum of the contributions from all sublattices,

$$\hat{S}_{\boldsymbol{k}}(\sigma) = \sum\nolimits_{p=1}^{v} S_{\boldsymbol{k},p}(\sigma) \qquad (6.9)$$

In this way, the long-ranged interaction parameter follows,

$$V^{CS}(\boldsymbol{k}) = \frac{1}{\hat{S}_{\boldsymbol{k}}(\sigma) \cdot \hat{S}^{*}_{\boldsymbol{k}}(\sigma)} \sum_{m,n} S_{\boldsymbol{k},m}(\sigma) \cdot V^{LR}_{m,n}(\boldsymbol{k}) \cdot S^{*}_{\boldsymbol{k},n}(\sigma) \qquad (6.10)$$

Although the above relation reveals the physical meaning of the effective long-ranged interaction parameter, it cannot be used to calculate the $V^{CS}(\boldsymbol{k})$, since $V^{LR}_{m,n}(\boldsymbol{k})$ is unknown. In the next step, a method to calculate $V^{CS}(\boldsymbol{k})$ for long-ranged CSE from DFT is presented.

In principle, multi-body interactions in the long range, other than pairs in the long range, may also contribute to the long-ranged interactions. However, in current MSCE, the long-ranged interactions are solely attributed to pairs due to two practical reasons. Firstly, treating multi-body interactions in k-space requires a Fourier transform of the multi-body interactions from r-space, which leads to cumbersome equations and complicates the problem. Secondly, including multi-body clusters with large diameters in the fitting would significantly increase the number of fitting parameters (i.e., r-space ECIs), which makes the fitting results less reliable even if the number of ECIs are smaller than the number of structures in the training set. Inevitably, such separation leads to inaccuracy in the descriptions of short- and long-ranged interactions. In previous MSCE calculations, this formalism leads to very accurate prediction of the formation energies (i.e., less than 2 meV/atom) in $Ga_{1-x}In_xP$ [24] and Ag-Pd system [28], which indirectly validate the assumption that long-ranged interactions can be attributed to pair clusters.

6.2.3 Calculation of the CSE for arbitrary mismatch and crystal symmetries

In the last step, the MSCE method is incomplete without the knowledge of the long-ranged interaction $V^{CS}(\boldsymbol{k})$. As discussed before, $V^{CS}(\boldsymbol{k})$ represent the long-ranged limit of the CSE for a compound A_qB_q as $q \rightarrow \infty$, in which case A_qB_q becomes an epitaxial configuration as visualized in **Fig. 6.1**. This configuration can be used to calculate the CSE along a certain orientation $\mathbf{G}$ (i.e., the normal of the epitaxial plane). Note that the difference between $\mathbf{G}$ and $\boldsymbol{k}$ is that $\mathbf{G}$ denotes the unit vector on the direction same as $\boldsymbol{k}$ but has no length. To eliminate the chemical interactions in this configuration and focus on the orientation dependent deformation energy, A and B can be distorted in separate cells instead of in direct contact and the coherency is remained as long as the lattice parameters on plane $\mathbf{G}$ are kept the same. Additionally, only small primitive cells are needed

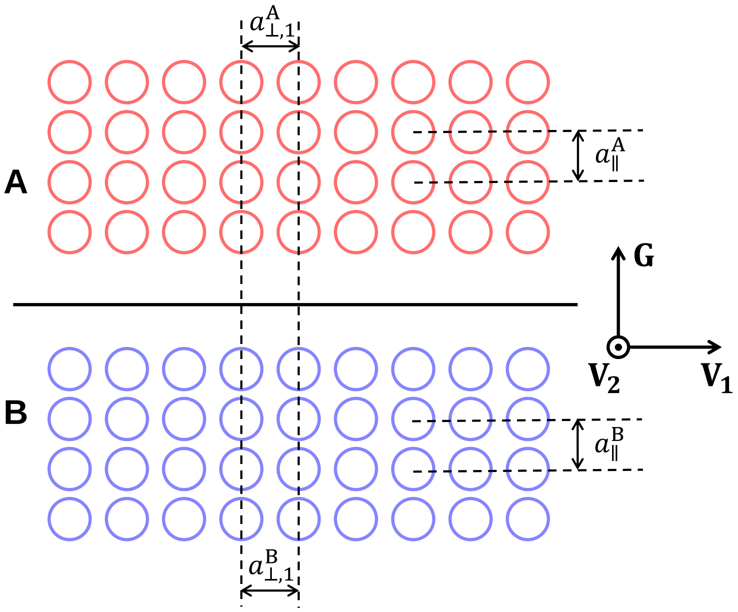

Fig. 6.1 Schematic illustration of the epitaxial configuration needed to calculate the orientation dependence of the CSE along $\mathbf{G}$. Generally, there are two independent lattice parameters on the epitaxial plane with normal $\mathbf{G}$, i.e., $a_{\perp,1}$ and $a_{\perp,2}$. The lattice parameters on the epitaxial plane ($a_{\perp,1}$ and $a_{\perp,2}$) are fixed to maintain coherency, while the lattice parameter along $\mathbf{G}$ ($a^{\mathrm{A}}_{\parallel}$ or $a^{\mathrm{B}}_{\parallel}$) is free to relax.

when separating A and B, while large supercell is needed to build a real epitaxial configuration if A and B are in contact. Previously, the CSE from DFT were incorporated in MSCE for binary cubic systems and the anharmonic lattice response due to large lattice mismatch were analyzed comprehensively [17,18,26,27,42]. The corresponding method is already implemented in Alloy Theoretic Automation Toolkit (ATAT) [43,44]. The CSEs for HCP Mg-Ca and Mg-Y systems were calculated previously, but the details of the calculation process were not reported [45]. Herein, a crystal-symmetry-agnostic algorithm for the calculation of CSE is developed.

For a given crystallographic orientation $\mathbf{G}$ (i.e., normal of the epitaxial plane), we can find two orientations perpendicular to $\mathbf{G}$, namely $\mathbf{V}_1$ and $\mathbf{V}_2$. Here $\mathbf{V}_1$ can be any vector perpendicular to $\mathbf{G}$ and $\mathbf{V}_2 = \mathbf{G} \times \mathbf{V}_1$. Along $\mathbf{V}_1$ and $\mathbf{V}_2$, the lattice parameters on the epitaxial plane are $a_{\perp,1}$ and $a_{\perp,2}$, which are stretched from the end member with smaller lattice parameter to the one with larger lattice parameters. For example, if $a_{\perp,1}^{A} < a_{\perp,1}^{B}$, then $a_{\perp,1}^{A} \leq a_{\perp,1} \leq a_{\perp,1}^{B}$. In practice, several values of $a_{\perp,1}$ serve as the grid points between $a_{\perp,1}^{A}$ and $a_{\perp,1}^{B}$. Once the values of $a_{\perp,1}$ and $a_{\perp,2}$ are picked, they are kept constant while the lattice parameter along $\mathbf{G}$ for both end members, i.e., $a_{\parallel}^{\mathrm{A}}$ or $a_{\parallel}^{\mathrm{B}}$, are relaxed to minimize the energy of the distorted cell. For an end member with lattice parameters of $a_{\perp,1}$, $a_{\perp,2}$ and $a_{\parallel}$ along $\mathbf{V}_1$, $\mathbf{V}_2$ and $\mathbf{G}$, the 3×3 matrix for the distorted lattice vector $\mathbf{L}'$ follows

$$\mathbf{L}' = \mathbf{L}^{\mathbf{0}} \cdot [\mathbf{Q} \cdot \mathbf{S} \cdot \mathbf{Q}^{T}] \tag{6.11}$$

where $\mathbf{L}^0$ is the 3×3 matrix for the lattice vectors of the end members at equilibrium (defined in the same coordinate system as $\mathbf{G}$, $\mathbf{V}_1$ and $\mathbf{V}_2$), $\mathbf{S}$ is the 3×3 matrix with dimensionless stretch of the lattice along $\mathbf{G}$, $\mathbf{V}_1$ and $\mathbf{V}_2$, and $\mathbf{Q}$ is the 3×3 matrix for the orientation of the epitaxial configuration using normalized vectors.

$$\mathbf{S} = \begin{bmatrix} a_{\parallel}/a_{\parallel}^{0} & 0 & 0 \\ 0 & a_{\perp,1}/a_{\perp,1}^{0} & 0 \\ 0 & 0 & a_{\perp,2}/a_{\perp,2}^{0} \end{bmatrix}, \quad \mathbf{Q} = \left[\frac{\mathbf{G}}{|\mathbf{G}|}, \frac{\mathbf{V}_1}{|\mathbf{V}_1|}, \frac{\mathbf{V}_2}{|\mathbf{V}_2|}\right] \tag{6.12}$$

Here $\mathbf{G}$, $\mathbf{V}_1$ and $\mathbf{V}_2$ are given by 1×3 row vectors. With the lattice vectors of the distorted cell, DFT calculation can be performed to obtain the distortion energy as a function of the $a_{\perp,1}$ and $a_{\perp,2}$ for both A and B, i.e., $\Delta E_{epi}^{\mathrm{A}}(a_{\perp,1}, a_{\perp,2})$ and $\Delta E_{epi}^{\mathrm{B}}\ (a_{\perp,1}, a_{\perp,2})$. The orientation and composition dependence of CSE follows,

$$\Delta E_{CS}(\mathbf{G}, x) = \min_{a_{\perp,1}, a_{\perp,2}} \left\{(1 - x)\Delta E_{epi}^{\mathrm{A}}(a_{\perp,1}, a_{\perp,2}) + x\Delta E_{epi}^{\mathrm{B}}(a_{\perp,1}, a_{\perp,2})\right\} \tag{6.13}$$

where x is the molar fraction of B in A-B system. In the calculations, $\Delta E_{epi}^{\mathrm{A}}$ and $\Delta E_{epi}^{\mathrm{B}}$ are calculated using the primitive cell for A and B on a pre-defined lattice.

The composition and orientation dependence of the CSE $\Delta E_{CS}(\mathbf{G}, x)$ needs to be transformed to obtain $V^{CS}(\boldsymbol{k})$. In the limit of $q \to \infty$, the CSE of structure $A_q B_q$ stacked along $\mathbf{G}$ is independent of q. This condition is only met if $V^{CS}(\boldsymbol{k})$ is independent of the magnitude of $\boldsymbol{k}$, i.e., $V^{CS}(\boldsymbol{k}) = V^{CS}(\widehat{\boldsymbol{k}})$ with $\widehat{\boldsymbol{k}} \equiv \boldsymbol{k}/|\boldsymbol{k}|$. Additionally, $\hat{S}(\boldsymbol{k}, \sigma) \neq 0$ holds only for the k-points with $\mathbf{G} \propto \boldsymbol{k}$. Therefore, the CSE for $A_q B_q$ stacked along $\mathbf{G}$ with $q \to \infty$ follows,

$$\Delta E_{CS}(\widehat{\boldsymbol{k}}) = V^{CS}(\widehat{\boldsymbol{k}}) \sum_{\boldsymbol{k}} \left|\hat{S}_{\boldsymbol{k}}(\sigma)\right|^2 \tag{6.14}$$

By definition, the $V^{CS}(\boldsymbol{k}) = 0$ for $\boldsymbol{k} = \mathbf{0}$. Therefore, $V^{CS}(\widehat{\boldsymbol{k}})$ can be obtained as,

$$V^{CS}(\widehat{\boldsymbol{k}}) = \Delta E_{CS}(\widehat{\boldsymbol{k}}) \Big/ \left[\sum_{\boldsymbol{k} \neq \mathbf{0}} \left|\hat{S}(\boldsymbol{k}, \sigma)\right|^2\right] \tag{6.15}$$

In the case of binary alloy where the spin variable of -1 and $+1$ are used, $\sum_{\boldsymbol{k} \neq \mathbf{0}} \left|\hat{S}(\boldsymbol{k}, \sigma)\right|^2$ reduces to $4x(1 - x)$, as formulated by Laks et al. [13]. Once the parent lattice and spin variables are defined for a system, the structural factor can be readily calculated and **Eq. (6.15)** can be adopted to relate $\Delta E_{CS}(\mathbf{G}, x)$ to $V^{CS}(\widehat{\boldsymbol{k}}, x)$ for a structure with composition x. In the general case of phases with multiple sublattices, the choice for the definition of spin variable is not unique as long as the orthogonality condition is obeyed [44]. In **Eq. (6.15)** the summation cannot be further simplified, since it depends on the specific choice for the definition of spin variables.

In an alloy configuration, the pairs can be aligned along any directions while the CSE data from **Eqs. (6.13-15)** can only be calculated for a few orientations by DFT. Therefore, parameterization is needed to yield the CSE surface that changes continuously with the orientation in *k*-space. This can be accomplished using the spherical harmonics adapted to the symmetry of the lattice [13,39,40]. In principle, any data on spherical coordinates can be fitted if infinite number of spherical harmonic functions are used. With prior knowledge of the symmetry of the lattice, spherical harmonics adapted to certain symmetry can be used to eliminate the redundant terms. For a structure with a given composition, the orientation dependence of $V^{CS}(\hat{\boldsymbol{k}})$ are parameterized by the symmetry-adapted spherical harmonics and the long-ranged CSE (without attenuation) for the structure can be calculated by **Eq. (6.8)**. For HCP Mg alloys, the hexagonal harmonic functions (HHFs) will be used [41].

Generally, there are two independent lattice parameters on the epitaxial plane (e.g., for hexagonal crystals). The number of independent lattice parameters can be reduced to one as long as the symmetry of lattice points on crystallographic plane $\hat{G}$ is retained. For a lattice with cubic symmetry, there is only one independent lattice parameter on high-symmetry planes (e.g., $\{001\}$ and $\{111\}$) and two for the low-symmetry planes (e.g., $\{110\}$). For the former, the above process can be simplified and reduces to the existing algorithm in ATAT [43,44]. In the current approach, the deformation energies, i.e., $\Delta E_{epi}^{\mathrm{A}}(a_{\perp,1}, a_{\perp,2})$ and $\Delta E_{epi}^{\mathrm{B}}(a_{\perp,1}, a_{\perp,2})$ are calculated based on DFT and is not limited to small size-mismatch between constituents, crystal symmetry or the number of sublattices.

6.2.4 Regularization of the ECIs

The reciprocal version of pair interactions enables the incorporation of interactions in very long range and along any direction. But this also means that the number of long-range interaction pairs is very large, which is difficult to be included in the CE Hamiltonian. Therefore, a method is needed to select the most import interactions which have large contributions and eliminate those with small contributions for the sake of computational feasibility. In the original work of Laks et al., the "smoothness condition" of interaction parameters in *k*-space is proposed and is added as a penalty to the loss function in the optimization process [13]. Although the smoothness condition is a different term with regularization, it provides the same function to reduce the number of fitting parameters. In the current method, the smoothening of $V_{m,n}(\boldsymbol{k})$ after separating the CSE at any *k*-point is equivalent to minimizing the magnitude of the secondary derivative with respect to the *k*-point,

$$\nabla_{\boldsymbol{k}}^2 V_{m,n}(\boldsymbol{k}) = -\frac{1}{2}\sum_{l} J_{m,n}(\boldsymbol{R}_l) \cdot R_l^2 \cdot e^{-i\boldsymbol{k}\cdot\boldsymbol{R}_l} \tag{6.16}$$

From **Eq. (6.16)**, smoothening of $\left|\nabla_{\boldsymbol{k}} V_{m,n}(\boldsymbol{k})\right|$ is equivalent to prioritizing the small clusters over larger ones, which is in accordance with the physical intuition that smaller clusters tend to have larger contribution to short-ranged chemical interactions. The loss function (ρ) of in the training of MSCE follows,

$$\rho = \sum_{\sigma\in s} w_\sigma |E^{DFT}(\sigma) - E^{MSCE}(\sigma)|^2 + \frac{t}{\alpha}\sum_{l} {\boldsymbol{R}_l}^4 \sum_{m,n} J_{m,n}^2(\boldsymbol{R}_l) \tag{6.17}$$

where w_σ is the weight of a configuration σ, $\alpha \equiv \sum_l R_l^4$ is a normalizing factor and t is a scaling factor for the smoothness condition. From **Eq. (6.17)**, the smoothness condition acts as a regularization (or shrinkage) technique for the chemical ECIs in *r*-space, i.e., the ECIs with smaller magnitudes will be favored over the larger ones if the residual errors are the same. The regularization of ECIs helps to reduce the prediction error for the testing dataset. With the regularization, the number of fitting parameters (i.e., ECIs) can be larger than the number of energies in the training set, thus significantly improves the fitting capability. Note that the smoothness condition is similar to the ridge technique used in machine learning to avoid overfitting [38]. The only difference is that, in smoothness condition in Eq. (12), the squares of ECIs are weight-averaged by the diameter of clusters.

6.2.5 Anisotropic attenuation of the long-ranged interactions

Combining the *r*-space CE and the formulation of long-ranged interactions, the expansion formula of MSCE can be written as,

$$E^{MSCE}(\sigma) = N \sum_{F,s\neq 2} D_F J_F \bar{\Pi}_F(\sigma) + N \sum_{\boldsymbol{k}} \sum_{m,n} S_{\boldsymbol{k},m}(\sigma) \cdot V_{m,n}^{SR}(\boldsymbol{k}) \cdot S_{\boldsymbol{k},n}^{*}(\sigma)$$

$$+ N \sum_{\boldsymbol{k}} \hat{S}_{\boldsymbol{k}}(\sigma) \cdot V^{CS}(\boldsymbol{k}) \cdot \hat{S}_{\boldsymbol{k}}^{*}(\sigma) \qquad (6.18)$$

On the right-hand-side (RHS) of **Eq. (6.18)**, the first term is the *r*-space CE and the summation runs over all the non-pair clusters, i.e., the number of sites $s \neq 2$. And the symmetrically equivalent clusters are grouped into a class of clusters (or figures, F), D_F is the number of equivalent clusters (or multiplicity) in F, J_F is the corresponding ECI for the equivalent clusters in F, $\bar{\Pi}_F$ is correlation function by averaging the product of spin variables. The second term on the RHS of **Eq. (6.18)** is the chemical interaction from pairs and the third term is the CSE, both modeled in *k*-space. Note that **Eq. (6.18)** is equivalent to the formulation of Laks et al. if a simple Bravais lattice ($v = 1$) is considered [13].

Furthermore, the second term on RHS of **Eq. (6.18)** is equivalent to the pair interaction in *r*-space CE if the derivation in **Eqs. (6.4)** and **(6.5)** is inversed. Since only relatively short-ranged clusters can be adopted in practical calculations of *r*-space CE, the sum of the first and second terms on RHS of **Eq. (6.18)** is the equivalent to *r*-space CE including all types of clusters. In this way, the expansion of configuration-dependent energy using MSCE follows,

$$E^{MSCE}(\sigma) = N\sum_{F} D_F J_F \bar{\Pi}_F(\sigma) + N\sum_{\boldsymbol{k}} V^{CS}(\boldsymbol{k}) \cdot \left|\hat{S}_{\boldsymbol{k}}(\sigma)\right|^2 \cdot \exp\left[-\frac{|\boldsymbol{k}|^2}{A(\boldsymbol{k})^2}\right] \tag{6.19}$$

From **Eqs. (6.6)**, **(6.18)** and **(6.19)**, a question arises concerning the modeling of the medium-ranged interactions that are not explicitly included in *r*-space CE or $V^{CS}(\boldsymbol{k})$, since *r*-space CE is short-ranged and $V^{CS}(\boldsymbol{k})$ is formulated in the long periodicity limit. Analysis by Ferreira et al. showed that $V^{CS}(\boldsymbol{k})$ decays exponentially with magnitude of the major wave vector with largest $|S_{\boldsymbol{k}}(\sigma)|$, when applied to medium-ranged structures [16]. In the formula by Ferreira et al. [16] and others that followed [17,29], it is assumed that the attenuation coefficient is orientation independent. However, the attenuation of $V^{CS}(\boldsymbol{k})$ as a function of $|\boldsymbol{k}|$ may vary along different orientations due to anisotropic response to long-ranged interactions. In **Eq. (6.19)**, an exponential factor $\exp\left[-\frac{|\boldsymbol{k}|^2}{A(\boldsymbol{k})^2}\right]$ for the decay of $V^{CS}(\boldsymbol{k})$ is added so that medium-ranged strain interactions can be modeled as well. The orientation-dependent decay coefficient $A(\boldsymbol{k})$ is parameterized using the symmetry-adapted spherical harmonics [39–41] in this work to minimize the fitting error of MSCE. Once the physical nature of the long-ranged interaction is embedded in the $V^{CS}(\boldsymbol{k})$, the configuration-dependent energy can be parameterized using **Eq. (6.19)**.

So far, we have extended the limited application of previous MSCE from binary cubic system with single sublattice to binary systems with any symmetry and multiple sublattices. Note that traditional CE is capable to describe multi-component systems with multiple sublattices and any symmetry. All limitation for MSCE comes from both the definition and calculation of CSE, which is the key of the medium- and long-range interactions.

6.3 Extension to multi-component systems

In the last section, the development of MSCE method in binary systems with multiple sublattices and arbitrary symmetry is shown. However, the number of elements in most systems in research or commercial applications are more than two. Therefore, we need the further extension of MSCE to multi-component systems with arbitrary symmetry on multi-sublattices. The development includes several steps. Since steps of (1) the formulation of k-space pair interactions for multiple sublattices, (2) calculating CSE for arbitrary lattice mismatch and crystal symmetry, (3) the regularization of the ECIs by smoothness condition, and (4) the anisotropic attenuation of the long-ranged interactions are all the same with those in binary systems developed in the last section, here we only focus on the key step: modeling configuration-dependent long-ranged interactions in k-space for multicomponent system.

The formulation of CSE in **Eqs. (6.11-15)** and the epitaxial configuration in **Fig. 6.1** only involve two constituents, and their applicability to multi-component alloys needs further examination. The success of MSCE for various systems validate the assumption that the long-ranged CSE in binary systems are primarily due to pair clusters. By definition, only two elements can reside on the sites of a pair cluster. If it is assumed that *the long-ranged CSE in multi-component alloys can also be primarily attributed to pair clusters*, the CSE for a structure in multi-component system can be calculated by summing up all the long-ranged CSE of pairs. Following this assumption, the CSE in ternary A-B-C ordering can be obtained by summing up the CSE of

A-B, A-C and B-C pairs calculated by **Eqs. (6.11-15)**, while the multi-body interactions are treated as chemical energy and calculated in *r*-space (**Eq. (6.11)**). Since the number of multi-body clusters (hence interaction parameters) explodes with increasing interaction distance, this assumption is also essential for a practical calculation. Note that this assumption was adopted decades ago by Khachaturyan et al. in the analytical modeling of long-ranged interactions in multi-component alloys [1,35].

In binary systems, we have discussed that, by definition, the $V^{CS}(\boldsymbol{k}) = 0$ for $\boldsymbol{k} = \boldsymbol{0}$. When $\boldsymbol{k} \neq \boldsymbol{0},$ $V^{CS}(\widehat{\boldsymbol{k}})$ can be obtained as, $V^{CS}(\widehat{\boldsymbol{k}}) = \Delta E_{CS}(\widehat{\boldsymbol{k}})/\left[\sum_{\boldsymbol{k}\neq\boldsymbol{0}}\left|\hat{S}(\boldsymbol{k},\sigma)\right|^{2}\right]$. Usually, the two spin variables are used with -1 and $+1$ to differentiate the two elements in binary systems. For any composition $x \neq 1/2$, we have [13]:

$$\sum_{\boldsymbol{k}=\boldsymbol{0}}|S(\boldsymbol{k},\sigma)|^2 + \sum_{\boldsymbol{k}\neq\boldsymbol{0}}|S(\boldsymbol{k},\sigma)|^2 = 1, \tag{6.20}$$

Also, the Fourier transformed spin variables at the origin of reciprocal space is,

$$S(\boldsymbol{0},\ \sigma) = \sum_{l}^{N} S_l(\sigma)e^{i\boldsymbol{0}\boldsymbol{R}_l} = \sum_l S_l(\sigma) = 2x - 1 \tag{6.21}$$

Therefore, in an indirect way, we obtain:

$$\sum_{\boldsymbol{k}\neq\boldsymbol{0}}|S(\boldsymbol{k},\sigma)|^2 = 1 - (2x-1)^2 = 4x(1-x), \tag{6.22}$$

Thus,

$$V^{CS}(\widehat{\boldsymbol{k}}) = \Delta E_{CS}(\widehat{\boldsymbol{k}})/[4x(1-x)] \tag{6.23}$$

Following the same logy in binary systems, a ternary system with three elements, i.e., A, B, and C, can be also derived. we assume the pair interactions in long periodic limit, $\mathit{\Delta} E_{CS}(x,\boldsymbol{k})$, of AB, BC, and AC are independent of each other for any configuration. Under this assumption, we have the CSE of a A-B-C ternary system defined in this form:

$$\Delta E_{CS}(x_A, x_B, x_C, \boldsymbol{k}) = (1-2x_C)\Delta E_{CS}^{AB}(\boldsymbol{k}) + (1-2x_B)\Delta E_{CS}^{AC}(\boldsymbol{k}) + (1-2x_A)\Delta E_{CS}^{BC}(\boldsymbol{k}) \tag{6.24}$$

where $x_A + x_B + x_C = 1$. The factors of $(1-2x)$ is an approximation for the sum of each three different kinds of pairs based on the composition of the system. Noted, the spin variables in ternary case are defined in a different way from the "± 1" in the binary case. As mentioned before, for multicomponent systems:

$$S(\boldsymbol{k}, \sigma) = \sum_l^N \gamma_{\alpha_i, M_i}(\sigma_i) e^{i\boldsymbol{k}\boldsymbol{R}_l}, \tag{6.25}$$

Therefore,

$$\sum_{\boldsymbol{k}=\boldsymbol{0}} |S(\boldsymbol{k}, \sigma)|^2 + \sum_{\boldsymbol{k}\neq\boldsymbol{0}} |S(\boldsymbol{k}, \sigma)|^2 = \sum_l^N \left(\gamma_{\alpha_i, M_i}(\sigma_i)\right)^2,$$

$$\sum_{\boldsymbol{k}\neq\boldsymbol{0}} |S(\boldsymbol{k}, \sigma)|^2 = \sum_l^N \left(\gamma_{\alpha_i, M_i}(\sigma_i)\right)^2 - \left(\sum_{\alpha_i} \gamma_{\alpha_{i, M_i}}(\sigma_i)\right)^2 \tag{6.26}$$

Therefore, we obtain the value of $V^{CS}(\widehat{\boldsymbol{k}})$ for multicomponent systems:

$$V^{CS}(\widehat{\boldsymbol{k}}) = \Delta E_{CS}(\widehat{\boldsymbol{k}}) / [\sum_l^N \left(\gamma_{\alpha_i, M_i}(\sigma_i)\right)^2 - \left(\sum_{\alpha_i} \gamma_{\alpha_{i, M_i}}(\sigma_i)\right)^2]. \tag{6.27}$$

6.4 The application in Mg-Zn-Ca ternary system

6.4.1 Calculations of CSE for the Mg-Zn-Ca sub-binary systems

As mentioned in last section, we assume that *the long-ranged CSE in multi-component alloys can also be primarily attributed to pair clusters*. Therefore, we start with the calculation of CSE for binary subsystem, i.e., Mg-Zn, Mg-Ca, and Ca-Zn. Since we focused on Mg-rich side of ternary system, the lattice of the system is defined on HCP, which the lattice of the matrix. The calculations follow the **Eqs. (6.11-15)** in the binary system with multiple sublattices and arbitrary symmetry in Section 6.1. To capture the whole feature of CSE with serval discrete directions as a function of $\boldsymbol{k}$ in reciprocal space, the CSE are calculated in 7 directions: $[10\bar{1}0]$, $[11\bar{2}0]$, $[0001]$, $[11\bar{2}1]$, $[11\bar{2}2]$, $[10\bar{1}2]$, $[30\bar{3}2]$ of the HCP lattice. The CSE value for Mg-Ca sub-binary system is shown in **Fig. 6.2**. As shown, at the Mg-rich side, CSE on $[0001]$ direction is the largest, which means Mg and Ca atoms don't like to be aligned with each other along $[0001]$ direction, and long-limit interaction of the Mg-Ca pair is the largest among the seven directions.

The CSE for the Mg-Zn sub-binary system is also calculated in these 7 directions, as shown in **Fig. 6.3**. At the Mg-rich side, CSE on all 7 directions are similar, which means CSE don't prefer any of the 7 directions, and the long-limit interaction of the Mg-Zn pair can be aligned on any of the 7 directions with almost the same strain energy penalty. The CSE for the Ca-Zn sub-binary system is also calculated in these 7 directions, as shown in **Fig. 6.4**. Due to the very large size mismatch between Ca and Zn, the CSE curves are not smooth on the directions of: $[10\bar{1}0]$, $[11\bar{2}0]$, $[0001]$, $[11\bar{2}1]$, and $[11\bar{2}2]$. To avoid the effect of the form of fitting functions, we plot the curves with very dense data points directly from DFT calculations, and the bizarre curves agrees with the current one. Therefore, we conclude that the shapes of the CSE curves are due to the nature of the

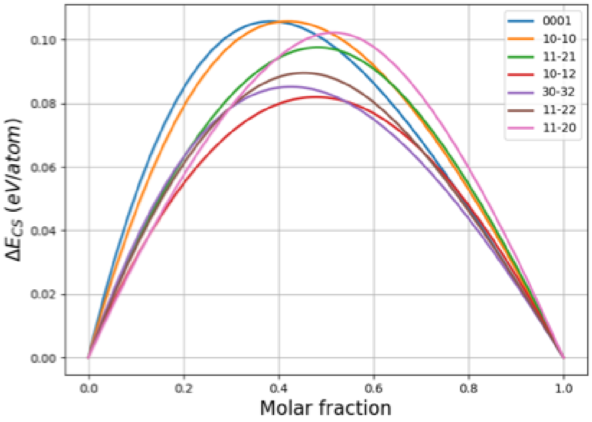

Fig. 6.2 The CSE calculated for the Mg-Ca sub-binary system on 7 different directions with the left of Mg rich side and right of Ca-rich side.

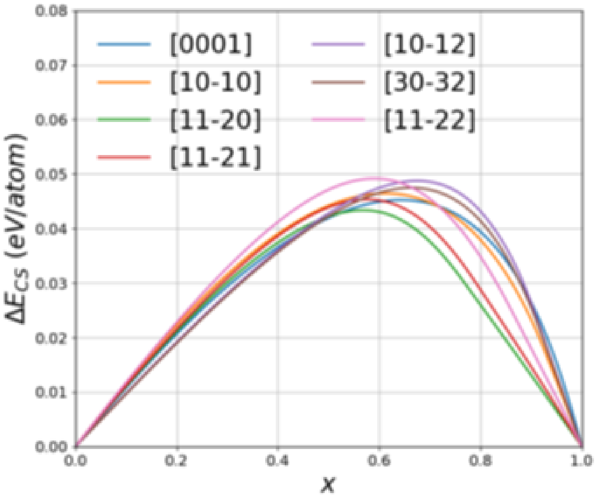

Fig. 6.3 The CSE calculated for the Mg-Zn sub-binary system on 7 different directions with the left of Mg rich side and right of Zn-rich side.

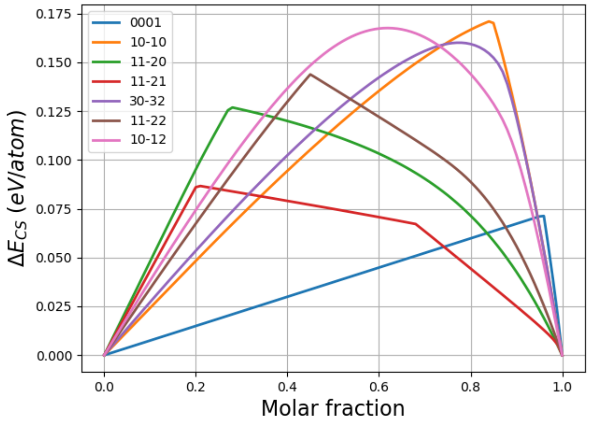

Fig. 6.4 The CSE calculated for the Ca-Zn sub-binary system on 7 different directions with the left of Ca-rich side and right of Zn-rich side.

electron interactions between the two elements. From those curves, it is seen that the CSE along the [0001] direction is much lower than those on the other 6 directions, which means the Ca-Zn pair prefers to be aligned along the [0001] direction. This calculation result is consistent with the proposed structures of the early-stage precipitates η' and η'' in Chapter 5, in which the Ca and Zn atoms are predicted to be aligned along the [0001] direction.

With the CSE values for the sub-binary systems of Mg-Zn-Ca, we can obtain the MSCE Hamiltonian for the ternary systems with multi-components, multi-sublattices, and arbitrary symmetry based on the **Eq. (6.19) and (6.24).** This Hamiltonian can be used to predict the low energy coherent phases in Mg matrix of this system. Further, it can be used in Monte Calo simulations to predict the shape of the precipitates. The most important part in the MSCE Hamiltonian is from the traditional CE that capture the short-range chemical interactions. Therefore, in the next section, we start with the traditional CE for Mg-Zn-Ca systems, which lay the basis for the building of MSCE Hamiltonian.

6.4.2 CE of the ternary Mg-Zn-Ca system

The CE of the Mg-Zn-Ca system uses the same DFT settings as we used for the prediction of monolayer GP zones in Chapter 4. This ternary system with very large size mismatch leads to the difficulty of the convergency of CE, which also calls for MSCE method to include the strain effect and help the convergence issue. Here we show the CE based on two kinds of training sets: fully relaxed structures and structures relaxed with volume and atomic positions. The reason for doing two kinds of CE is that the effect of large off-lattice relaxation can be easily compared and shown, and the effect of the CSE will be better shown in two different cases. Additionally, the fixed shape relaxation helps the atoms keep the original symmetry. In the full relaxed CE calculations, structures with atoms less than or equal to 8 are searched, which corresponds to 6075 symmetrically distinct structures, and all structures are included despite their degree of lattice distortion and formation enthalpies. The CV score of this CE calculation is 36.32 meV/atom. In the fixed-shape CE, structures with the number of atoms equal to or less than 10 atoms are considered, which corresponds to 36963 symmetrically distinct structures. In this case, structures

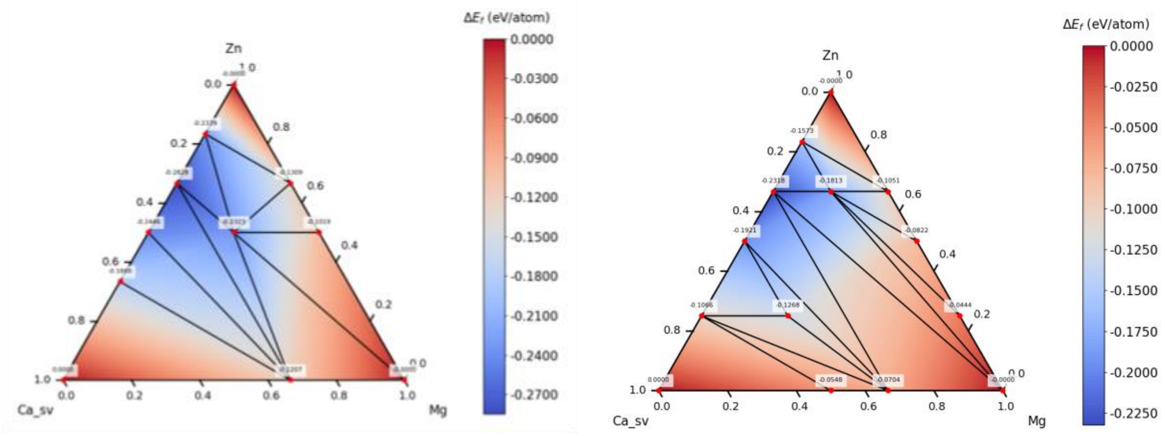

Fig. 6.5 The formation energy landscape of the Mg-Zn-Ca ternary system showing the mixing tendency of solutes under the relaxation of all degrees **(left)** and volume and atomic positions **(right)**.

with energies far away from the convex hull are excluded to accelerate the convergence and focus on the low energy structures. In this CE calculation, the CV score is 15.47 meV/atom.

The formation energy landscapes of the two CE calculations are shown in **Fig. 6.5**. The value of the formation energies reflects the tendency of the bonding of different elements, and the corner of pure elements is the reference state with the energies of zero. Comparing the mixing tendency of different elements, we can see that Ca and Zn have the largest combing trend, followed by Mg and Zn atoms, and then Mg and Ca atoms. This tendency is consistent with what we predicted for the atoms in the monolayer GP zones in Mg-Zn-Ca alloys. Further, the fully relaxation leads to a larger area of bule region, which corresponds to a bigger mixing tendency of Ca and Zn atoms. On the contrary, the bule region in the energy landscape of CE with fixed shape

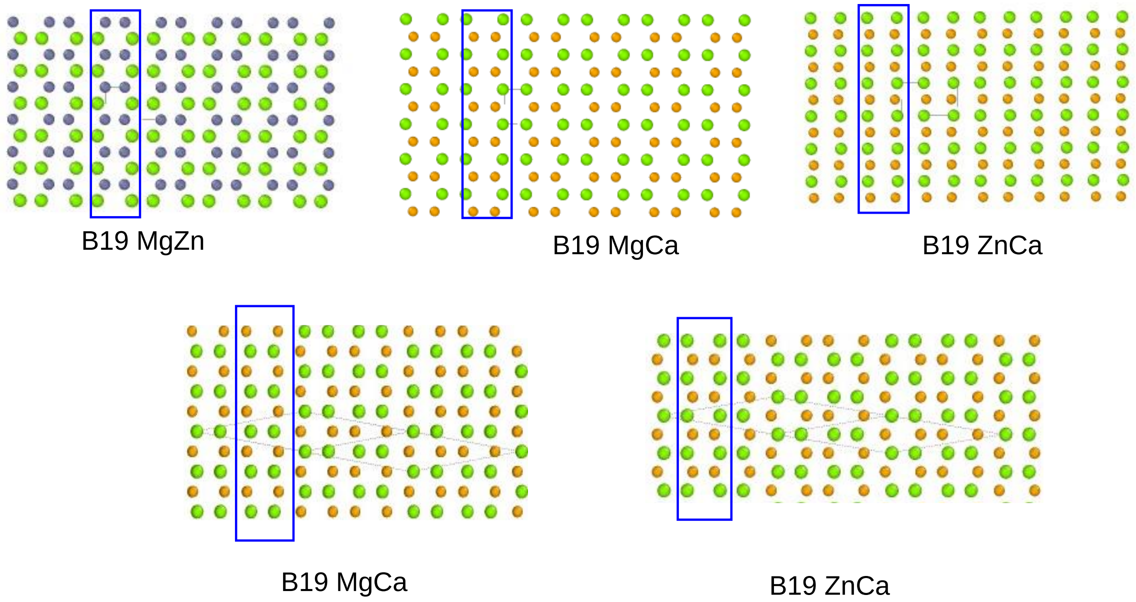
B19 MgZn
B19 MgCa
B19 ZnCa
B19 MgCa
B19 ZnCa

Fig. 6.6 The predict low energy structures showing the feature of B19, which is marked by the blue boxes. Noted these structures are all binary compounds and lay on the side the ternary phase diagrams of Mg-Zn-Ca system.

are much smaller, which means the relaxation method constrains atoms from breaking the original symmetry and constrains structures reach low energies.

The goal here is to study the coherent precipitates, like, GP zones. Since we focused on the structures distorted not far away from the HCP lattice, the CE of the fixed relaxations with lower CV scores are used to predict low energy structures. In the searched 36963 structures, some low energies structures show the feature of B19 MgZn, as shown in **Fig. 6.6**. In these structures, they contain two kinds of elements and lays on the sides of the ternary convex hull. Also, some structures resemble C15 Laves phases with unit layers stacking along [001] directions. In the unit layer, one sublayer resembles GP zones with big atoms surrounded by 6 small atoms on the hexagonal lattice, and another sublayer forming the Kagome net by big atoms. In these structures, both binary and ternary compounds appear, as some examples shown in **Fig. 6.7**. Additionally,

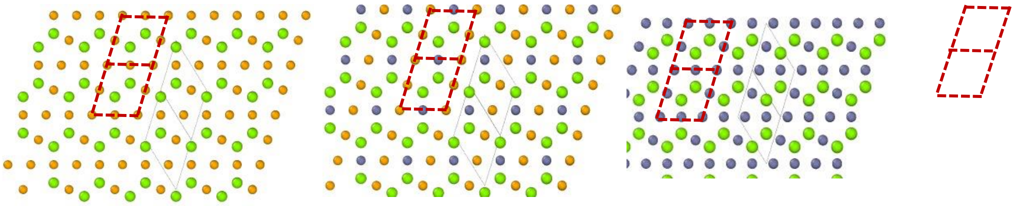

C15 Mg_2Ca C15 Mg_3Ca_2Zn C15 Zn_2Mg C15 Zn_3Ca_2Mg

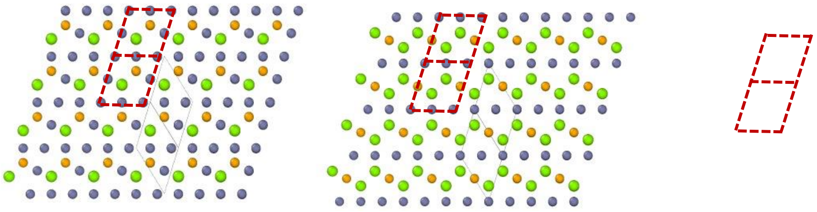

C15 Zn_4MgCa C15 Zn_3Ca_2Mg C15 Zn_2Ca

Fig. 6.7 The predict low energy structures showing the feature of C15 Laves phase, which is marked by the red dash lines. The unit layers is marked by the rhombohedrons, where two sublayers can be seen. Noted these structures includes both binary and ternary compounds.

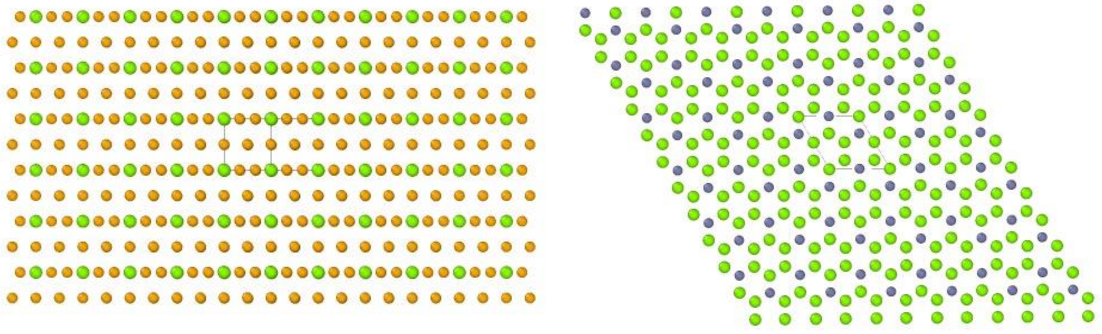

$CaCu_5$ type Laves phase $CaZn_5$ D_019 Mg_3Zn

Fig. 6.8 The predict low energy structures showing the feature of C15 Laves phase, which is marked by the red dash lines. The unit layers is marked by the rhombohedrons, where two sublayers can be seen. Noted these structures includes both binary and ternary compounds.

there are low energy structures resembles CaCu5 type Laves phases and D_019 phase, as examples shown in **Fig. 6.8**.

The CV score of the fully relaxed CE is around 30 meV/atom, which means we need a method to improve the predictability and convergence of CE, if we want to use this method to study the structures layer on the convex hull of the experiments. Therefore, the MSECE method is a good way to go.

Reference

[1] A.G. Khachaturyan, Theory of Structural Transformations in Solids, Dover Publications, Mineola, New York, 1983.

[2] F. Ducastelle, Order and Phase Stability in Alloys, 1993, Interatomic Potential and Structural Stability.

[3] A. Zunger, First-Principles Statistical Mechanics of Semiconductor Alloys and

Intermetallic Compounds, 1994, Statics and Dynamics of Alloy Phase Transformations.

[4] D. de Fontaine, Cluster approach to Order-Disorder Transformation in Alloys, *Solid State Phys.* 47 (1994) 33–176.

[5] A. Van de Walle, G. Ceder, The effect of lattice vibrations on substitutional alloy thermodynamics, *Rev. Mod. Phys.* 74 (2002) 11–45.

[6] A. V. Ruban, I.A. Abrikosov, Configurational thermodynamics of alloys from first principles: Effective cluster interactions, *Reports Prog. Phys.* 71 (2008) 046501.

[7] J.M. Sanchez, F. Ducastelle, D. Gratias, Generalized cluster description of multicomponent systems, *Phys. A Stat. Mech. Its Appl.* 128 (1984) 334–350.

[8] P. Hohenberg, W. Kohn, Inhomogeneous Electron Gas, *Phys. Rev.* 136 (1964) 864.

[9] W. Kohn, L.J. Sham, Self-Consistent Equations Including Exchange and Correlation Effects, *Phys. Rev.* 140 (1965) A1133.

[10] J.W.D. Connolly, A.R. Williams, Density-functional theory applied to phase transformations in transition-metal alloys, *Phys. Rev. B.* 27 (1983) 5169–5172.

[11] A. van de Walle, Methods for first-principles alloy thermodynamics, *JOM.* 65 (2013) 1523–1532.

[12] S. De Gironcoli, P. Giannozzi, S. Baroni, Structure and thermodynamics of SixGe1-x alloys from ab initio Monte Carlo simulations, *Phys. Rev. Lett.* 66 (1991) 2116–2119.

[13] D.B. Laks, L.G. Ferreira, S. Froyen, A. Zunger, Efficient cluster expansion for substitutional systems, *Phys. Rev. B.* 46 (1992) 12587–12605.

[14] L.G. Ferreira, A.A. Mbaye, A. Zunger, Chemical and elastic effects on isostructural phase diagrams: The -G approach, *Phys. Rev. B.* 37 (1988) 10547–10570.

[15] O.I. Gorbatov, Y.N. Gornostyrev, P.A. Korzhavyi, Many-body mechanism of Guinier-

Preston zones stabilization in Al–Cu alloys, *Scr. Mater.* 138 (2017) 130–133.

[16] L.G. Ferreira, V. Ozoliņš, A. Zunger, Fitting of accurate interatomic pair potentials for bulk metallic alloys using unrelaxed LDA energies, *Phys. Rev. B - Condens. Matter Mater. Phys.* 60 (1999) 1687–1696.

[17] C. Wolverton, V. Ozoliņš, A. Zunger, Short-range-order types in binary alloys: A reflection of coherent phase stability, *J. Phys. Condens. Matter*. 12 (2000) 2749–2768.

[18] C. Wolverton, L.W. Wang, A. Zunger, Coherent phase stability in al-zn and al-cu fcc alloys: the role of the instability of fcc zn, *Phys. Rev. B - Condens. Matter Mater. Phys.* 60 (1999) 16448–16462.

[19] V. Ozoliņš, C. Wolverton, A. Zunger, Cu-Au, Ag-Au, Cu-Ag, and Ni-Au intermetallics: First-principles study of temperature-composition phase diagrams and structures, *Phys. Rev. B*. 57 (1998) 6427–6443.

[20] J.Z. Liu, A. Zunger, Thermodynamic theory of epitaxial alloys: First-principles mixed-basis cluster expansion of (In, Ga)N alloy film, *J. Phys. Condens. Matter*. 21 (2009).

[21] V. Blum, A. Zunger, Mixed-basis cluster expansion for thermodynamics of bcc alloys, *Phys. Rev. B - Condens. Matter Mater. Phys.* 70 (2004) 1–17.

[22] A. Zunger, L.G. Wang, G.L.W. Hart, M. Sanati, Obtaining ising-like expansions for binary alloys from first principles, *Model. Simul. Mater. Sci. Eng.* 10 (2002) 685–706.

[23] Z. Lu, D. Laks, S. Wei, A. Zunger, First-principles simulated-annealing study of phase transitions and short-range order in transition-metal and semiconductor alloys, *Phys. Rev. B - Condens. Matter Mater. Phys.* 50 (1994) 6642–6661.

[24] C. Wolverton, A. Zunger, Ising-like Description ofStructurally Relaxed Ordered and Disordered Alloys, *Phys. Rev. Lett.* 73 (1995) 3162–3165.

[25] Z.W. Lu, B.M. Klein, A. Zunger, Thermodynamic instability of ag/au and cu/pd metal superlattices, *Superlattices Microstruct.* 18 (1995) 161–175.

[26] C. Wolverton, V. Ozolins, A. Zunger, First-principles theory of short-range order in size-mismatched metal alloys: Cu-Au, Cu-Ag, and Ni-Au, *Phys. Rev. B.* 57 (1998) 4332–4348.

[27] V. Ozoliņš, C. Wolverton, A. Zunger, Effects of anharmonic strain on the phase stability of epitaxial films and superlattices: Applications to noble metals, *Phys. Rev. B.* 57 (1998) 4816–4828.

[28] S. Müller, A. Zunger, First-principles predictions of yet-unobserved ordered structures in the Ag-Pd phase diagram, *Phys. Rev. Lett.* 87 (2001) 165502/1-165502/4.

[29] C. Wolverton, First-principles theory of 250,000-atom coherent alloy microstructure, *Model. Simul. Mater. Sci. Eng.* 8 (2000) 323–333.

[30] S. Müller, C. Wolverton, L.W. Wang, A. Zunger, Prediction of alloy precipitate shapes from first principles, *Europhys. Lett.* 55 (2001) 33–39.

[31] J.Z. Liu, G. Trimarchi, A. Zunger, Strain-minimizing tetrahedral networks of semiconductor alloys, *Phys. Rev. Lett.* 99 (2007) 1–4.

[32] C. Ravi, B.K. Panigrahi, M.C. Valsakumar, A. Van De Walle, First-principles calculation of phase equilibrium of V-Nb, V-Ta, and Nb-Ta alloys, *Phys. Rev. B - Condens. Matter Mater. Phys.* 85 (2012) 1–10.

[33] A. Issa, J.E. Saal, C. Wolverton, Physical factors controlling the observed high-strength precipitate morphology in Mg-rare earth alloys, *Acta Mater.* 65 (2014) 240–250.

[34] G. Wysin, Onsager reaction-field theory for magnetic models on diamond and hcp lattices, *Phys. Rev. B - Condens. Matter Mater. Phys.* 62 (2000) 3251–3258.

[35] A.G. Khachaturyan, Ordering in substitutional and interstitial solid solutions, *Prog. Mater.*

Sci. 22 (1978) 1–150.

[36] D. de Fontaine, Configurational Thermodynamics of Solid Solutions, *Solid State Phys.* 34 (1979) 73–274.

[37] L.B. Frechette, C. Dellago, P.L. Geissler, Consequences of Lattice Mismatch for Phase Equilibrium in Heterostructured Solids, *Phys. Rev. Lett.* 123 (2019) 135701.

[38] G. James, D. Witten, T. Hastie, R. Tibshirani, Introduction to Statistical Learning with Applications in R, 2nd ed., Springer, 2021.

[39] S.L. Altmann, A.P. Cracknell, Lattice Harmonics I. Cubic Groups, *Rev. Mod. Phys.* 37 (1965) 19–32.

[40] S.L. Altmann, A.P. Cracknell, Lattice Harmonics II. Hexagonal Close-Packed Lattice, *Rev. Mod. Phys.* 37 (1965) 33–45.

[41] A. Van De Walle, Q. Hong, L. Miljacic, A. Kowalski, P. Tiwary, Ab initio calculation of anisotropic interfacial excess free energies, *Phys. Rev. B - Condens. Matter Mater. Phys.* 184101 (2014) 1–11.

[42] V. Ozoliņš, C. Wolverton, A. Zunger, Strain-induced change in the elastically soft direction of epitaxially grown face-centered-cubic metals, *Appl. Phys. Lett.* 72 (1998) 427–429.

[43] A. Van de Walle, M. Asta, G. Ceder, The alloy theoretic automated toolkit: A user guide, *CALPHAD.* 26 (2002) 539–553.

[44] A. van de Walle, Multicomponent multisublattice alloys, nonconfigurational entropy and other additions to the Alloy Theoretic Automated Toolkit, *CALPHAD.* 33 (2009) 266–278.

[45] C.N. Varney, G.L.W. Hart, C. Wolverton, A Coherency Strain Model for Hexagonal-Close-Packed Alloys, *TMS Lett.* 1 (2005) 35–36.

[46] A. van de Walle, M. Asta, Self-driven lattice-model Monte Carlo simulations of alloy

thermodynamic properties and phase diagrams, *Model. Simul. Mater. Sci. Eng.* 10 (2002) 521–538.

[47] K. Wang, D. Cheng, C. Fu, B. Zhou, First-principles investigation of the phase stability and early stages of precipitation in Mg-Sn alloys, *Phys. Rev. Mater.* 013606 (2020) 1–13.

[48] G. Strang, Linear Algebra and Its Applications, 4th ed., Cengage Learning, 2006.

[49] C. Zhu, R.H. Byrd, P. Lu, J. Nocedal, Algorithm 778: L-BFGS-B: Fortran Subroutines for Large-Scale Bound-Constrained Optimization, *ACM Trans. Math. Softw.* 23 (1997) 550–560.

[50] P. Virtanen, R. Gommers, T.E. Oliphant, M. Haberland, T. Reddy, D. Cournapeau, et al., SciPy 1.0: fundamental algorithms for scientific computing in Python, *Nat. Methods*. 17 (2020) 261–272.

[51] D. Joubert, From ultrasoft pseudopotentials to the projector augmented-wave method, *Phys. Rev. B.* 59 (1999) 1758–1775.

[52] J.P. Perdew, K. Burke, M. Ernzerhof, Generalized gradient approximation made simple, *Phys. Rev. Lett.* 77 (1996) 3865–3868.

[53] G. Kresse, J. Furthmüller, Efficiency of ab-initio total energy calculations for metals and semiconductors using a plane-wave basis set, *Comput. Mater. Sci.* 6 (1996) 15–50.

[54] G. Kresse, Efficient iterative schemes for ab initio total-energy calculations using a plane-wave basis set, *Phys. Rev. B.* 54 (1996) 11169–11186.

[55] D. Cheng, K. Wang, B.-C. Zhou, A Comprehensive First-Principles Investigation of the Phase Structures and Stabilities in Mg-Zn Alloys, sumitted to Acta Materialia, 2022.

[56] A.R. Natarajan, E.L.S. Solomon, B. Puchala, E.A. Marquis, A. Van Der Ven, On the early stages of precipitation in dilute Mg-Nd alloys, *Acta Mater.* 108 (2016) 367–379.

[57] M. Stricker, B. Yin, E. Mak, W.A. Curtin, Machine learning for metallurgy II. A neural-network potential for magnesium, *Phys. Rev. Mater.* 4 (2020) 1–20.

[58] D. Marchand, A. Jain, A. Glensk, W.A. Curtin, Machine learning for metallurgy I. A neural-network potential for Al-Cu, *Phys. Rev. Mater.* 4 (2020) 1–21.

[59] C.W. Rosenbrock, K. Gubaev, A. V. Shapeev, L.B. Pártay, N. Bernstein, G. Csányi, G.L.W. Hart, Machine-learned interatomic potentials for alloys and alloy phase diagrams, *Npj Comput. Mater.* 7 (2021) 1–9.

[60] C. Verdi, F. Karsai, P. Liu, R. Jinnouchi, G. Kresse, Thermal transport and phase transitions of zirconia by on-the-fly machine-learned interatomic potentials, *Npj Comput. Mater.* 7 (2021).

[61] A. Singraber, J. Behler, C. Dellago, Library-Based LAMMPS Implementation of High-Dimensional Neural Network Potentials, *J. Chem. Theory Comput.* 15 (2019) 1827–1840.

[62] A. Bendo, T. Maeda, K. Matsuda, A. Lervik, R. Holmestad, C.D. Marioara, K. Nishimura, N. Nunomura, H. Toda, M. Yamaguchi, K. ichi Ikeda, T. Homma, Characterisation of structural similarities of precipitates in Mg–Zn and Al–Zn–Mg alloys systems, *Philos. Mag.* 99 (2019) 2619–2635.

[63] J. Buha, Reduced temperature (22-100 °C) ageing of an Mg-Zn alloy, *Mater. Sci. Eng. A.* 492 (2008) 11–19.

[64] J.F. Nie, Precipitation and hardening in magnesium alloys, *Metall. Mater. Trans. A.* 43A (2012) 3891–3939.

Chapter 7 Summary and Future Work

7.1 Summary of results

Mg alloys with high number densities of GP zones in the specific RE-free Mg alloys show significantly enhanced strength while retaining a high elongation. At the same time, they can be extruded at rates comparable to commercial Al alloys with much lower density. These attractive properties are the motivation of the GP zone-strengthened Re-free Mg alloys. However, the knowledge to control the formation of the preferred coherent precipitates to realize these desired prosperities is still lacked. The basis of the knowledge to control the prosperities through precipitates is the knowledge of the basis properties of the precipitates, which mainly includes coherent precipitates in current context. The information of precipitates can be used in predict the hardening effect through either empirical model or atomic scale model. However, even with the state-of-art experimental equipment, the direct identification from experiments of the atomic scale structures of GP zones and other early-stage precipitates formed during aging is still difficult, and the explanation of the observed shapes and orientations of precipitates remains unclear.

In this work, we use cluster expansion to predict the atomic structures, orientation relationships, metastable phase diagrams of GP zones in binary Mg-Zn and further ternary Mg-Zn-Ca systems. The prediction from ab initial calculations agrees well with the experimental reports, e.g., the zig-zag GP zones plates on the $(10\bar{1}0)_\alpha$ prismatic planes in Mg-Zn binary alloys and the monolayer GP zones on the basal plane in Mg-Zn-Ca and Mg-Zn-Nd alloys. These results prove the validity of CE Hamiltonian in predicting ground state structures of the coherent phases in the defined matrix. In addition to the prediction of atomic structures, our CE Hamiltonian is also capable to predict the metastable phase diagrams of GP zones in Mg-Zn binary systems combined with Mote Carlo simulation. To explore the structures of precipitates in ternary Mg-Zn-Ca, we proposed the structures for all the observed ternary phases based on the atomic contrast in HAADF-STEM images and diffraction patterns from experiments in the Mg-0.6Zn-0.3Ca alloy aged at 200 C. The proposed structures are validated by comparing the simulated diffraction patterns and atomic contrast in STEM images with the experimental results.

CE is a lattice model and relies on defined the lattice sites of the structures. The ternary CE of the Mg-Zn-Ca systems shows large CV scores and difficulty of convergence, which is caused by the large lattice mismatch and severe off lattice distortion of structures after relaxation from ideal HCP lattice. To solve the convergence issue and improve the predictability of the CE, we developed mix-space cluster expansion (MSCE) for system with multiple sublattices, multiple elements and arbitrary symmetry besides cubic systems. Specifically, the process involves the extension of original Fourier transform of spin variables that represent the species on the lattice defined sites from single sublattice to multiple sublattice. Further, the calculation of CSE is extend from cubic systems to systems with arbitrary symmetry. Lastly, the binary CSE is extended to ternary systems that mainly based on the averaged composition. With the current MSCE method, the new Hamiltonian is expected to predict the coherent phases in the cared Mg-Zn-Ca systems.

7.2 Conclusion

The atomic structures of precipitates in binary Mg-Zn and ternary Mg-Zn-Ca systems are explored using combined computational and experimental methods. The provided atomic structures give access to the important information of precipitates, e.g., stability, lattice parameters, and antiphase boundary energy, which are required to predict the macroscale properties like strength and ductility in analytical models. Therefore, the current work lay the foundation for the design of precipitation strengthened RE-free Mg alloys. The Mg-Zn system is the basis for many commercial alloys due to its strong age hardening response. Our provided structures of GP zones and β_1' precipitates address people's concerns or inquires regarding the nanoscale early-stage precipitates and β_1' with a complex hierarchy of phases in this system. The Mg-Zn-Ca system shows good combinations of extrudability and strength in extrusions and formability and strength in sheets that have never been achieved in commercial Mg alloys. Our exploration of precipitate structures explains the driving force of the observed precipitation sequence. Additionally, the predicted GP zones update people's understanding of their structures and the bonding trend of atoms in this system. Based on the current predicted structures of precipitate, it is suggested that the contribution of basal plane GP zones on the strength from both its surrounding strain field and antiphase boundary energy does not reach the expected values. Other methods are needed to greatly improve the desired properties, e.g., promoting the formation of GP zones on prismatic planes, strengthening the Mg alloy by texture and twins.

7.3 Future Work

In current work, the mathematical expression of the MSCE in systems with multicomponent, multi-sublattice, and arbitrary symmetries are developed. Therefore, the future work involves:

1) Apply the correction from MSCE to the traditional CE that has been done in current work on Mg-Zn-Ca systems and improve the convergence of the CE and its predictability.
2) Use the MSCE Hamiltonian to search the ground states in Mg-Zn-Ca systems and predict low energy structures, including the coherent precipitates, e.g., GP zones, formed in the early-stage aging, and compare with the experimental observations.
3) Combine MSCE with Monte Calo simulations to predict the shape, size, phase diagrams of GP zones in Mg Re-free alloys, which can be useful information for the thermomechanical processing for the industrial application.
4) Predict the chemical system in which prismatic plate-like precipitates will form, e.g., the Mg-In-Ca system.
5) The ideal of including the long-range interaction in materials into MSCE can be used to study other long-range interactions in other functional materials, like columbic interactions in electrode material.

Biography

Du Cheng is originally from the city of Xi’an in China. She received her Bachelor of Science, with Distinction in Materials Physics at the Northwestern Polytechnical University in Xi’an, China in 2015. Immediately following, she commenced her study on the simulation of interactions of dislocations with precipitates in Al alloys under the supervision of Prof. Feng Liu and then received her Master of Engineering in Materials Science and Engineering at the Northwestern Polytechnical University in 2018. Same year, she started the work on the GP-zone strengthened Mg alloys at University of Virginia under the supervision of Prof. Bi-Cheng Zhou and was expected to complete her Ph.D. in 2023. A list of publications during her Ph.D. study is given below.

[1] **D. Cheng**, K. Wang, B.C. Zhou. “Crystal structure and stability of phase in MgZn: a comprehensive first-principles study.” Acta Mater. (2022): 118443.

[2] **D. Cheng**, E. R. Hoglund, K. Wang, J. M. Howe, S. R. Agnew, Bi-Cheng Zhou. “Atomic structures of ordered monolayer GP zones in Mg-Zn-X (X= Ca, Nd) systems.” Scripta Mater. 216 (2022): 114744.

[3] **D. Cheng**, K. Wang, B.C. Zhou. “First-Principles Investigation of the Early-Stage Precipitations in Mg-Sn and Mg-Zn Alloys.” Mag. Tech. Springer, Cham, 2022. 281-290. (TMS LMD Magnesium Technology Best Paper Award)

[4] K. Wang, **D. Cheng**, B.C. Zhou. “First-principles investigation of the phase stability and early stages of precipitation in Mg-Sn alloys.” Phy. Rev. Mater. 4.1 (2020): 013606.

[5] K. Wang, **D. Cheng**, B.C. Zhou. “Mixed-space cluster expansion in multicomponent system with arbitrary lattice”. npj Comp. Mater., under review.

[6] Z.H. Li*, **D. Cheng***, K. Wang, E. R. Hoglund, J. M. Howe, B.C. Zhou, T.T. Sasaki, T. Ohkubo, K. Hono. “Revisit of precipitation process in dilute Mg-0.3Ca-0.6Zn alloy” Acta Mater., submitted. (***equally contributions**)